Implementation and Characterization of 16-port Devices in Circuit Quantum Electrodynamics

Yulin LIU

Master student in the Department of Physics

Master Thesis 2012

Laboratory for Solid State Physics
ETH Zurich

Supervisors: Lars Steffen & Dr. Arkady Fedorov

Professor: Prof. Dr. Andreas Wallraff

Quantum Device Lab

Abstract

Quantum computation and quantum information have been proposed and investigated intensively in recent years [1]. The peculiar properties in the quantum world are believed to bring revolutionary computation abilities in future (e.g. the entanglement and the superposition could result in parallel processing). The Cavity Quantum Electrodynamics which studies the coherent interaction between atoms and quantized electromagnetic fields trapped inside of a cavity is one of the most promising and rich paradigms for the realization of quantum computation.

In our lab, the atom in the cavity is a superconducting two-level system called transmon [20] and the cavity is replaced by a transmission line resonator to achieve strong coupling strength between the transmon and the quantized photon. The transmission line resonators and the transmons are deposited and etched on a sapphire based microchip. Each resonator is capacitively coupled to its input and output ports. RF frequency signals are sent through these resonators and are detected via these ports. The transmons are placed at the ends and the crosses of the resonators and are controlled by the flux lines and the charge lines which are connected to the ports on an interface called Printed circuit board (PCB). Photons of microwave range and pulsed dc currents are sent to the transmons via these gate lines. With more ports on the microchip and on the PCB, more resonators and transmons can be controlled individually and simultaneously.

The mission of this thesis is trying to build up some new 16-port devices. The theoretical descriptions of the Cavity Quantum Electrodynamics are first briefly reviewed. The signal synthesis and acquisition processes, together with the dilution refrigerator, are explained. Different versions of microchips (7 mm x 6.6 mm) of various quality factors are designed using the software Mathematica 8. Other 16-port devices are designed and modeled using the softwares autodesk Inventor and autoCAD Mechanical (e.g. PCBs, PCB covers). The specifications of these devices are shown successively. The characterizations of different microchips with and without PCB covers at different temperatures are displayed in chapter 4. The measurements of the microchip with three crossed resonators (one with open ends) and big transmon size (200 μm x 60 μm) are conducted and shown in the last chapter.

Contents

Chapter 1

Introduction

On 27th April 1900, in the British Association for the Advancement of Science the British physicist Lord Kelvin claimed that

> There is nothing new to be discovered in physics now. All that remains is more and more precise measurement.

However two dark "clouds", the experiment of Michelson and the ultraviolet catastrophe, were still hanging over the classical physics. These two uninterpretable experiments at that time led to the naissances of the theory of relativity and quantum theory. The quantum theory has ever since developed and progressed dramatically. It successfully explained many phenomena found at that time and later which are hard to be explained with classical physics, counterintuitively though.

Since the middle of the twentieth century, the development of the computer has generally kept in accordance with the so-called Moore's law which states that the number of transistors that can be arranged on an integrated circuit with the same price doubles every 18 months [2]. However, this law can not be sustained shortly in the future when the size of the transistors reaches the atomic level due to the rise of the quantum effects. One of the solutions to this impasse is not trying to get rid of these inevitable quantum effects at the single atom level but trying to take advantage of them.

The idea of quantum computation and quantum information has then generated naturally. Earlier on in 1982, Richard Feynman came up with the idea of simulating the quantum system using a quantum computer [3] since our nature consists of essentially myriad of quantum systems which can only be simulated efficiently by quantum systems. The success of quantum computation in future, in turn, will help to better understand the counterintuitive quantum physics. In 1985, the universal quantum computer is formally discussed by D. Deutsch [4]. In 1990s, Peter Shor proposed an algorithm which can efficiently factorize large numbers on a quantum computer than any algorithms can on classical computers [5]. Lov Grover also suggested an efficient database searching algorithm [6] using a quantum computer.

However, it was only since last couple of decades, the precise control over single quantum system at will, the physical implementations of quantum computation and quantum information have been set up in reality.

The physical realization of a quantum bit (dubbed qubit) should be individually controllable meanwhile strongly decoupled from its environment (including its controlling and measurement channels) to avoid noise and losing information which is a dilemma. Currently several types of qubit realizations are intensely investigated. They are photons, Rydberg atoms, superconducting Josephson junction qubits, spins of Nitrogen Vacancy centers in diamond, quantum dots and trapped ions. In our experiment, the physical realization of qubits are the superconducting Josephson junctions.
Before this thesis, the design, implementation and characterization of the 8-port devices in Circuit Quantum Electrodynamics (Circuit QED) have been done. Three qubits can be implemented and controlled individually on these devices. Some fruitful measurements have been conducted [7, 8]. During this thesis, we have been trying to build up several 16-port devices in Circuit QED. With these 16-port devices, the number of qubits that can be controlled individually is more flexible.
In the first chapter, a brief introduction of the fundamental conceptions, terminologies and theories will be given. In the following chapter, a brief review of the measurement setup and some design and fabrication specifications will be shown. In the chapter three, the characterizations of the PCB cover, gatelines and resonators are exhibited. The measurements of the relaxation time and dephasing time of the qubits are accomplished successively in the following chapter. In the last chapter, in-depth discussions, conclusions and outlook are presented.

Chapter 2

Theory

Quantum electrodynamics (QED) studies the light matter interaction. If the photons are confined inside of a cavity, the atoms in the cavity can strongly couple to certain modes of photons. The research on the interaction between atoms and photons trapped in a cavity is called Cavity QED [9]. In this chapter, the theoretical aspect of superconducting Josephson junction qubits and Cavity QED will be briefly reviewed. In the following sections the physical realization of the qubit is first presented. The mathematical representation of the qubit is then introduced. Based on the introduction of the illustrative Bloch sphere, the evolution and preparation of the qubit state are presented. In the last part, the Hamiltonian of the Cavity QED is showed and the quantum-non-demolition (QND) readout principle is interpreted.

2.1 Josephson junction

Two superconducting materials separated by a thin insulator (or a non superconducting thin metal, or even a constraint of superconducting thin film) display some peculiar physics phenomenon as shown below. This was first found in 1962 by Brian David Josephson [10] who won a Nobel prize in physics shortly after that discovery.

In the superconducting regime, the macroscopic wave functions of the Cooper pairs (a pair of electrons with opposite spins and angular momenta gathering together due to the interaction with phonons) [12] in the left and right superconductors (see Fig 2.1 a) are $\psi_i = \sqrt{\rho_i}e^{i\theta_i}$ (i=1,2). ρ_i are the Cooper pair densities, and θ_i are the phases in each side. ψ_1 and ψ_2 can overlap (i.e. Cooper pairs can tunnel through the barrier coherently and result in a current) if the insulating layer is thin enough. Suppose that the two superconductors are connected by a voltage source V, then the current flowing through the Josephson junction is given by [13]

$$J = \frac{2K}{\hbar}\sqrt{\rho_1\rho_2}\sin\delta, \tag{2.1}$$

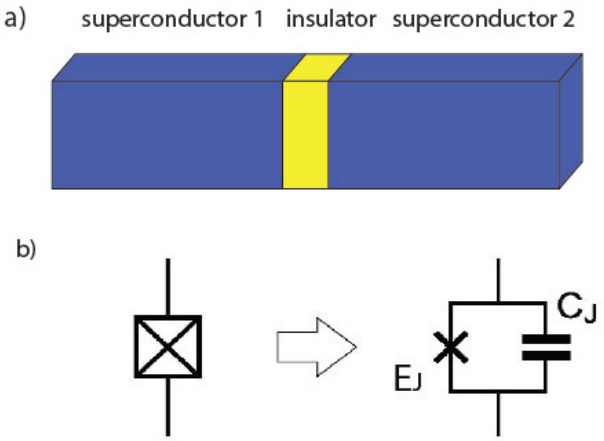

Figure 2.1: a) The schematic illustration of the Josephson junction. b) the Josephson junction (represented by a cross in a box) can be modeled by a capacitor and a Josephson element in parallel [11].

where K is the coupling strength of the wave functions in both sides and δ is the phase difference

$$\delta(t) = \theta_2(t) - \theta_1(t) = \delta_0 + \frac{2e}{\hbar}\int V(t)dt = \delta_0 + \frac{2e}{\hbar}\int \boldsymbol{A}d\boldsymbol{l}, \tag{2.2}$$

where $\delta_0 = \delta(t = 0)$ and $\boldsymbol{A}$ is the magnetic vector potential which is integrated from one electrode to the other one. The DC Josephson effect is in the case that the voltage V(t)=0, a constant current flows through the junction due to the tunneling of the Cooper pairs. The current can be written as [14, 15]

$$J = J_c \sin\delta. \tag{2.3}$$

$J_c = \pi\Delta(T)/2eR_n \tanh(\Delta(T)/2k_BT)$ [16] is the critical current. $\Delta(T)$ is the temperature dependent band gap between the ground Cooper pair state and the excited quasiparticle state. R_n is the resistance of the junction in non-superconducting regime. It inversely scales with the cross sectional area A of the junction and exponentially scales with the thickness d of the insulating film (i.e. $R_n \propto e^{dM}/A$). M is the material dependent constant.
If a DC voltage $V_0 < V_g = 2\Delta/e$ (the so called gap voltage) is set, a sinusoidal current with frequency $2eV_0/\hbar$ is formed [17]. This is called AC Josephson effect. Later, we will see, the nonlinearity of the Josephson junction is of paramount importance for the anharmonicity of the energy levels of the superconducting qubits. If the applied voltage is over the gap voltage, the Cooper pairs are separated into quasiparticles.
The energy stored in the Josephson junction when a voltage is applied is

$$\begin{aligned} E_1 = \int JV dt &= \int J_c \sin\delta \frac{\hbar}{2e}\frac{d\delta}{dt}dt = \frac{\hbar}{2e}J_c\int \sin\delta d\delta \\ &= \frac{\Phi_0 J_c}{2\pi}(1-\cos\delta) = E_J(1-\cos\delta), \end{aligned} \tag{2.4}$$

where Φ_0 is the magnetic flux quantum and $E_J = \Phi_0 J_c/2\pi$ is the Josephson energy. The Josephson energy is engineered during the fabrication process which allows to control the thickness and the area of the insulating layer.
The total charging energy stored in the Josephson junction is

$$E_2 = \frac{CV^2}{2} = \frac{C}{2}\left(\frac{n2e}{C}\right)^2 = 4n^2\frac{e^2}{2C} = 4n^2E_C, \tag{2.5}$$

where C is the total capacitance, n is the number of excessive Cooper pair on one side of the superconductor with respect to the neutral state and $E_C = e^2/2C$ is the charging energy (the electrostatic energy needed to transfer one electron from one side to the other side).

2.2 Cooper pair box and Transmon

The Cooper pair box (CPB) [18] is a Josephson junction capacitively coupled to a voltage source (see Fig 2.2 a). Cooper pairs of electrons can tunnel coherently back and forth through the insulating layer. The number of excess Cooper pairs on the island (red part in Fig 2.2 a) can be controlled by the gate voltage V_g.
Since E_C and E_J are determined during the fabrication process, in our experiments, the CPB with only single Josephson junction is replaced by the split Cooper pair box (see Fig 2.2 b). The island is connected to the reservoir by two parallel Josephson junctions which is usually called SQUID (Superconducting QUantum Interference Device). In addition to the control parameter of the gate voltage V_g, the Josephson energy is now also tunable by the magnetic flux through its SQUID loop created by an external coil.

$$E_J = (E_{J1} + E_{J2})\cos\left(\pi\frac{\Phi}{\Phi_0}\right) = E_J^{max}\cos\left(\pi\frac{\Phi}{\Phi_0}\right). \tag{2.6}$$

Thus the transition frequency of the qubit (the split CPB with its two lowest energy levels) is controllable by the external magnetic field created by coils. The Hamiltonian of the split CPB is

$$\mathscr{H}_{CPB} = \sum_n [E_C(\hat{n} - n_g)^2|n\rangle\langle n| - \frac{E_J}{2}(|n\rangle\langle n+1| + |n+1\rangle\langle n|)]. \tag{2.7}$$

$\hat{n}$ is the operator of the excess CPB number on the island with respect to the neutral state. $n_g = -C_gV_g/2e$ is the number of charges on the capacitor C_g (in units of 2e). Thus $2(n - n_g)$ is the effective excess charge number with respect to the neutral state. We can write the Hamiltonian in the matrix form

$$\mathscr{H}_{CPB} = \begin{pmatrix} \ddots & & & & & \\ & E_C(-1-n_g)^2 & -\frac{E_J}{2} & 0 & & \\ & -\frac{E_J}{2} & E_C(0-n_g)^2 & -\frac{E_J}{2} & 0 & \\ & 0 & -\frac{E_J}{2} & E_C(1-n_g)^2 & -\frac{E_J}{2} & 0 \\ & & & & & \ddots \end{pmatrix}.$$

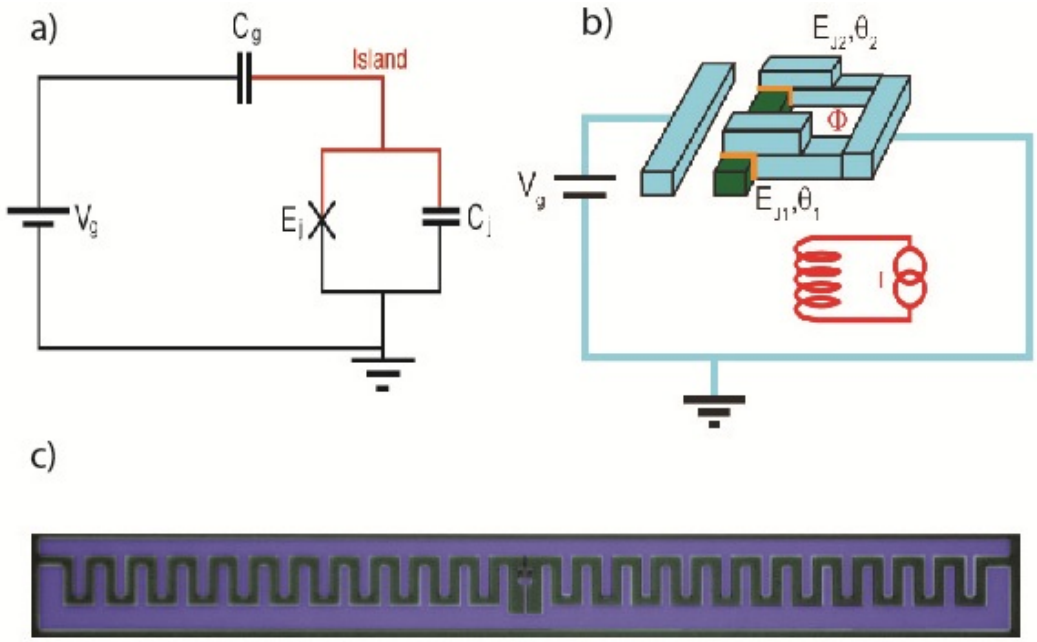

Figure 2.2: a) The circuit diagram of the CPB capacitively coupled to a voltage source. b) The schematic illustration of the split CPB. The Josephson energy is controlled by an external magnetic field created by a coil. c) The optical microscope image of transmon (300 μm x 30 μm) with false color [28]. The split CPB is shunted by a large finger capacitor which results in a relatively small charging energy.

The off-diagonal elements are all zero except for the elements directly neighboring to the diagonal elements.
If we restrict to the first two levels n=0, 1, the matrix can be reformed into

$$\mathscr{H}_{CPB2} = \begin{pmatrix} E_C n_g^2 & -\frac{E_J}{2} \\ -\frac{E_J}{2} & E_C(1-n_g)^2 \end{pmatrix}.$$

The energy dispersion of the split CPB in the charge regime is quite large as can be seen from the Fig 2.3 a. The transition frequency is thus sensitive to the charge noise. The split CPB is mainly operated at the sweet spot ($n_g = 0.5$) to be first order immune to charge noise (because the first derivative of energy dispersion at this point is zero) and to get higher coherence time. Focusing around the degenerate point $n_g = 1/2$ and using the Taylor expansion, we get the approximation

$$\mathscr{H}_{n_g \approx \frac{1}{2}} = \begin{pmatrix} \frac{1}{2}E_C(2n_g - 1) & -\frac{E_J}{2} \\ -\frac{E_J}{2} & -\frac{1}{2}E_C(2n_g - 1) \end{pmatrix}.$$

Correspondingly, its eigenvalues are

$$E_{0,1} = \pm\frac{1}{2}\sqrt{E_C^2(2n_g - 1)^2 + E_J^2}. \tag{2.8}$$

The transition energy from ground state to the first excited state at the sweet spot is approximately E_J.
Even though operated at the sweet spot, the coherence time of the split CPB is still limited by higher-order effects [19]. This can be easily solved using the split CPB in the transmon regime ($E_J \gg E_C$) instead of in the charge regime ($E_C \gg E_J$). This could be achieved by shunting the split CPB with a large finger capacitor (see Fig 2.2 c). Correspondingly the charging energy is significantly reduced.
The realization of the qubit should satisfy the requirement of having enough

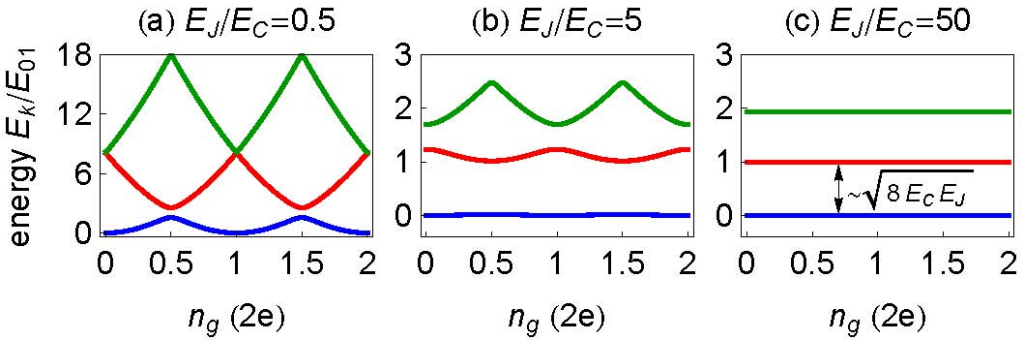

Figure 2.3: The energy spectrum of the split CPB with different E_J/E_C ratio [28]. The energy levels E_k (k=1,2,3) are plotted in unit of the transition energy E_{01} at $n_g = 0.5$.

anharmonicity (the transition frequency between ground state and first excited state ω_{01} is significantly different from the one from the first excited state to the second excited state ω_{12}). The anharmonicity of the split CPB is only algebraically reduced while the energy dispersion is exponentially flattened when increasing the ratio of E_J/E_C [20].
The transition frequency from ground state to the first excited state is approximately given by

$$\hbar\omega_{01} \approx \sqrt{8E_C E_J^{max} |\cos(\pi \frac{\Phi}{\Phi_0})|} - E_C. \tag{2.9}$$

The anharmonicity of the transmon is given by

$$\hbar\omega_{12} - \hbar\omega_{01} \approx -E_C. \tag{2.10}$$

In our experiment, the charging energy of the transmon is around 200 MHz which is large enough for the requirement of anharmonicity.

2.3 Bloch sphere

Bloch sphere is an illustrative and easily accessible tool towards better understanding of the evolutions of a single qubit [1].
In the Fig 2.4, the south and north poles of this sphere represent state $|0\rangle$

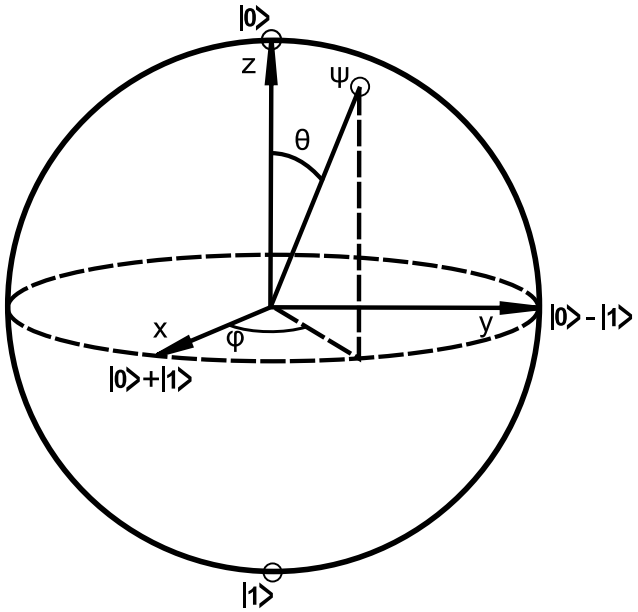

Figure 2.4: The schematic illustration of the Bloch sphere [1]. The south and north poles indicate the ground and excited states respectively. The dashed line represent the equator where the probabilities of finding the ground state or the excited state are equally 1/2.

and $|1\rangle$ respectively. Any state $|\psi\rangle$ of the qubit can be represented as a vector on the Bloch sphere.

$$|\psi\rangle = e^{i\gamma}(\cos\frac{\theta}{2}|0\rangle + e^{i\phi}\sin\frac{\theta}{2}|1\rangle), \tag{2.11}$$

where γ is global phase, θ is polar angle and ϕ is azimuthal angle.

2.4 The density matrix

The density operator is defined as

$$\hat{\rho} = \sum_i P_i|\varphi_i\rangle\langle\varphi_i|, \tag{2.12}$$

where P_i is the probability of the qubit being in the state $|\varphi_i\rangle$.
A pure quantum system can be equivalently described by both the wavefunctions and the density operators (matrices). For a quantum system with mixed state, the density operator description is more advantageous.
The expectation values of any operator $\hat{O}$ can be obtained by summing over the trace of $\hat{\rho}\hat{O}$, i.e. $\langle\hat{O}\rangle = Tr(\hat{\rho}\hat{O})$. The density matrix is Hermitian and $Tr\,(\hat{\rho}) = 1$ for both mixed state and pure state. For a pure state, the density operator can be written as $\hat{\rho} = |\varphi\rangle\langle\varphi|$, therefore $\hat{\rho}^2 = |\varphi\rangle\langle\varphi|\varphi\rangle\langle\varphi| = |\varphi\rangle\langle\varphi| = \hat{\rho}$ and $Tr\,(\hat{\rho}^2) = Tr\,(\hat{\rho}) = 1$. While for a mixed state, $0 < Tr\,(\hat{\rho}^2) < 1$.
If the dynamics of a quantum system is described by a time-dependent unitary

operator $U(t)$, then the elvolution of its density operator is $\rho(t) = U(t)\rho(t=0)U^{\dagger}(t)$. The single qubit density matrix can also be written as

$$\hat{\rho} = \frac{\mathbf{1} + \boldsymbol{r} \cdot \boldsymbol{\sigma}}{2}, \tag{2.13}$$

where $\boldsymbol{r} = (r_x, r_y, r_z)$ is a vector on or inside of the Bloch sphere, $\mathbf{1}$ is the identity operator and $\boldsymbol{\sigma} = (\sigma_x, \sigma_y, \sigma_z)$ are the Pauli matrices.

$$\begin{pmatrix} \rho_{00} & \rho_{01} \\ \rho_{10} & \rho_{11} \end{pmatrix} = \frac{1}{2} \begin{pmatrix} 1 + r_z & r_x - ir_y \\ r_x + ir_y & 1 - r_z \end{pmatrix}.$$

Thus

$$r_x = \rho_{01} + \rho_{10}, r_y = i\left(\rho_{01} - \rho_{10}\right), r_z = \rho_{00} - \rho_{11}. \tag{2.14}$$

since $\hat{\rho}$ is Hermitian, $\rho_{00} + \rho_{11} = 1$ and $\rho_{10} = \rho_{01}^{*}$.
The Eq. (2.13) can be used to calculate the expectation values:

$$\langle \sigma_x \rangle = Tr\left(\hat{\rho}\sigma_x\right) = Tr\left[\frac{1}{2}\left(\sigma_x + r_x\sigma_x^2 + r_y\sigma_y\sigma_x + r_z\sigma_z\sigma_x\right)\right] = Tr(\frac{1}{2}r_x\mathbf{1}) = r_x. \tag{2.15}$$

Therefore, r_x is the expectation value of the observable along $\overrightarrow{x}$ direction σ_x. Idem for $\langle \sigma_y \rangle = r_y$ and $\langle \sigma_z \rangle = r_z$.

$$Tr\left(\hat{\rho}^2\right) = Tr\left[\left(\frac{\mathbf{1} + \boldsymbol{r} \cdot \boldsymbol{\sigma}}{2}\right)^2\right] = \frac{1 + |\mathbf{r}|^2}{2}. \tag{2.16}$$

Therefore, the pure state corresponds to the vector on the Bloch sphere, i.e. $|\boldsymbol{r}| = 1$. The probability of a qubit in a given state (ground state $|0\rangle$, for example) is obtained by the projection expectation value of the projection operator $\hat{P}_0 = |0\rangle\langle 0|$.

$$P_{|0\rangle} = Tr(\hat{P}_0\hat{\rho}) = Tr[\begin{pmatrix} 1 & 0 \\ 0 & 0 \end{pmatrix}\begin{pmatrix} \rho_{00} & \rho_{01} \\ \rho_{10} & \rho_{11} \end{pmatrix}] = \rho_{00} = \frac{1 + r_z}{2}.$$

Idem

$$P_{|1\rangle} = Tr(\hat{P}_1\hat{\rho}) = Tr(|1\rangle\langle 1|\hat{\rho}) = Tr(\frac{\mathbf{1} - \hat{\sigma_z}}{2}\hat{\rho}) = \rho_{11} = \frac{1 - r_z}{2}.$$

Therefore the diagonal elements are the probabilities to find the qubit in a certain state (which indicates that the diagonal elements are non-negative real values). The off-diagonal elements represent the phase coherence between states. The pure states are prone to evolve into mixed states due to the dephasing effects.

2.5 State preparation

Any single qubit state can be prepared by applying a sequence of pulses (mathematically, a sequence of unitary operations) onto the initial ground state. This

process corresponds to a sequence of rotations on the Bloch sphere.
For a system in its ground state $|\psi_i\rangle = |0\rangle$, the final state
$|\psi_f\rangle = e^{i\gamma}\left(\cos\frac{\theta}{2}|0\rangle + \sin\frac{\theta}{2}e^{i\phi}|1\rangle\right)$ can be obtained by applying a sequence of unitary operations onto its initial state:

$$U(\Theta)|\psi_i\rangle = |\psi_f\rangle$$

with $U(\Theta) = \exp\left(i\hat{\sigma}\cdot\hat{n}\frac{\Theta}{2}\right)$, where $\hat{n} = (n_x, n_y, n_z)$ is the rotation axis and Θ is the angle of rotation.
As can be seen here, $U(\Theta)$ is a unitary operator $UU^\dagger = \hat{I}$.
e.g.
1)

$$|\psi_f\rangle = |1\rangle, U(\pi) = \exp\left(i\sigma_x\frac{\pi}{2}\right) = \cos\frac{\pi}{2}\hat{I} + i\sin\frac{\pi}{2}\sigma_x = i\begin{pmatrix}0 & 1\\ 1 & 0\end{pmatrix}.$$

The above calculations are based on the following approximation: for $\hat{O}^2 = \hat{I}$ and $\Theta \in \mathbf{R}$, $e^{i\Theta\hat{O}} = \cos\Theta\hat{I} + i\sin\Theta\hat{O}$.
The identity operator $\hat{I}$ and Pauli matrices $\sigma_x, \sigma_y, \sigma_z$ satisfy the $\hat{O}^2 = \hat{I}$.
2)

$$|\psi_f\rangle = 3e^{i\frac{\pi}{4}}\sin\frac{3\pi}{8}|1\rangle - 3\cos\frac{3\pi}{8}|0\rangle$$

the final state can be simplified:

$$|\psi_f\rangle = e^{i\pi}[\cos\frac{3\pi}{8}|0\rangle + \sin\frac{3\pi}{8}e^{i\frac{5\pi}{4}}|1\rangle]$$

The corresponding global phase $\gamma = \pi$, polar angle $\theta = 3\pi/4$ and azimuthal angle $\varphi = 5\pi/4$. Therefore $U = \exp\left(-i\frac{\pi}{8}\sigma_z\right)\cdot\exp\left(i\frac{3\pi}{8}\sigma_y\right)$.

2.6 Bloch equation

Considering an isolated nuclear spin with an intrinsic angular momentum $\vec{I}$ in a static magnetic field $\vec{B} = (0, 0, B_0)$ which can be deemed as a 2-level system, its Hamiltonian can be written as

$$\mathscr{H} = -\vec{M}\cdot\vec{B} = -\gamma\vec{I}\cdot\vec{B} = -\gamma m\hbar B_0, \tag{2.17}$$

where $\vec{M}$ is its magnetic momentum, m is the spin quantum number $\pm 1/2$, γ is the gyromagnetic ratio. The dynamics of the spin in this static magnetic field is described by the Lamor precession with precession frequency γB_0,

$$\frac{d\vec{M}(t)}{dt} = \vec{M}(t)\times\gamma\vec{B}. \tag{2.18}$$

Now, if the environmental effects are taken into account (for example, interaction with surrounding lattice, random fluctuations of the local magnetic field

etc.), the longitudinal (spin lattice) relaxation time and transversal (spin-spin) relaxation time come into play. Then the equation (2.18) is rewritten as

$$\begin{aligned}
\frac{dM_x(t)}{dt} &= \gamma(\vec{M}(t) \times \vec{B}(t))_x - \frac{M_x(t)}{T_2} \\
\frac{dM_y(t)}{dt} &= \gamma(\vec{M}(t) \times \vec{B}(t))_y - \frac{M_y(t)}{T_2} \\
\frac{dM_z(t)}{dt} &= \gamma(\vec{M}(t) \times \vec{B}(t))_z - \frac{M_z(t) - M_0}{T_1},
\end{aligned} \tag{2.19}$$

where $M_0 = \lim_{t\to\infty} M_z(t)$.
The solution of equation (2.19) is

$$\begin{aligned}
M_x(t) &= M_0 \cos(\Omega t) e^{-t/T_2} \\
M_y(t) &= M_0 \sin(\Omega t) e^{-t/T_2} \\
M_z(t) &= M_0 \left(1 - e^{-t/T_1}\right)
\end{aligned}$$

with $\Omega = -\gamma B_0$.
From the solution of equation (2.19), it can be easily seen that $\gamma_1 = 1/T_1$ describes the relaxation rate and $\gamma_2 = 1/T_2$ represents the rate of decoherence of the transverse nuclear spin magnetization (loss of initial coherence, no net xy plane magnetization) due to the random fluctuations of the magnetic field. If the random variation origins are slow on the time scales of experiments, the spin echo experiment [1] can compensate the loss of coherence. If T_1 and T_2 are infinitely large, equation (2.19) is the same as equation (2.18).
Now let's consider a 2-level system with transition frequency w_{01} driven by an external EM field with frequency w, phase ϕ and amplitude Ω_R. The corresponding Hamiltonian can be written as

$$\mathscr{H} = \frac{1}{2}\hbar w_{01}\sigma_z + \hbar\Omega_R \cos(wt + \phi)\sigma_x. \tag{2.20}$$

In the Heisenberg representation, the Hamiltonian is rewritten as

$$\mathscr{H} = U\mathscr{H}U^\dagger - i\hbar U\frac{\partial U^\dagger}{\partial t} \tag{2.21}$$

with $U(t) = e^{i\frac{wt}{2}\sigma_z}$.
Thus

$$\begin{aligned}
\mathscr{H} = e^{i\frac{wt}{2}\sigma_z}\frac{1}{2}\hbar w_{01}\sigma_z e^{-i\frac{wt}{2}\sigma_z} + \hbar\Omega_R\cos(wt+\phi)e^{i\frac{wt}{2}\sigma_z}\sigma_x e^{-i\frac{wt}{2}\sigma_z} \\
- i\hbar e^{i\frac{wt}{2}\sigma_z}(-i\frac{w}{2}\sigma_z)e^{-i\frac{wt}{2}\sigma_z}.
\end{aligned}$$

Due to $[U, \sigma_z] = 0$ and $[U, \sigma_x] \neq 0$,

$$\begin{aligned}
\mathscr{H} &= \frac{\hbar w_{01}}{2}\sigma_z + \hbar\Omega_R\cos(wt+\phi)\left[\cos(wt)\sigma_x - \sin(wt)\sigma_y\right] - \frac{\hbar w}{2}\sigma_z \\
&= \frac{\hbar\Delta}{2}\sigma_z + \frac{\hbar\Omega_R}{4}\left[e^{i(wt+\phi)} + e^{-i(wt+\phi)}\right]\left[(e^{iwt} + e^{-iwt})\sigma_x - (\frac{e^{iwt} - e^{-iwt}}{i})\sigma_y\right],
\end{aligned}$$

where $\Delta = w_{01} - w$ is the detuning term.

$$\mathscr{H} = \frac{\hbar\Delta}{2}\sigma_z + \frac{\hbar\Omega_R}{4}[(e^{i(2wt+\phi)} + e^{-i(2wt+\phi)} + e^{-i\phi} + e^{i\phi})\sigma_x + i(e^{i(2wt+\phi)} + e^{-i(2wt+\phi)} + e^{-i\phi} - e^{-i\phi})\sigma_y].$$

According to the Rotating Wave Approximation (RWA) which is valid if the detuning Δ and the driving amplitude Ω_R are small, the fast rotating terms can be neglected.
The final effective Hamiltonian with RWA is written as

$$\mathscr{H} = \frac{\hbar\Delta}{2}\sigma_z + \frac{\hbar\Omega_R}{2}(\cos\phi\sigma_x + \sin\phi\sigma_y). \tag{2.22}$$

The evolution of this quantum 2-level system can be visualized on the Bloch sphere. The Hamiltonian can also be written as

$$\mathscr{H} = -\frac{1}{2}\hbar\gamma\vec{\sigma}\cdot\vec{B} \tag{2.23}$$

with $\gamma\vec{B} = (\Omega_R\cos\phi, \Omega_R\sin\phi, \omega_{01} - \omega)$.
Therefore the two-level system with a driving field is analogous to the spin $\frac{1}{2}$ in a time-dependent magnetic field. The dynamics of this driven two-level system can also be described by the Bloch equations as proven below.
In the Heisenberg picture, $\dot{A} = \frac{i}{\hbar}[\mathscr{H}, A]$. Therefore,

$$\begin{aligned}
\dot{\sigma}_x &= \frac{i}{\hbar}[\mathscr{H}, \sigma_x] \\
&= -\frac{i\gamma}{2}[\vec{\sigma}\cdot\vec{B}, \sigma_x] \\
&= -\frac{i\gamma}{2}[\sigma_x B_x + \sigma_y B_y + \sigma_z B_z, \sigma_x] \\
&= -\frac{i\gamma}{2}(-i\sigma_z B_y + i\sigma_y B_z) \\
&= -\gamma[\vec{\sigma}\times\vec{B}]_x \\
&\qquad (\sigma_i\sigma_j = i\varepsilon_{ijk}\sigma_x)
\end{aligned}$$

Due to

$$\langle\sigma_x\rangle = Tr[\sigma_x\rho],$$

we get

$$\begin{aligned}
\langle\dot{\sigma}_x\rangle &= Tr[\dot{\sigma}_x\rho] = -\gamma Tr[(\vec{\sigma}\times\vec{B})_x\rho] \\
&= -\gamma[Tr(\vec{\sigma}\rho)\times\vec{B}]_x = -\gamma[\langle\vec{\sigma}\rangle\times\vec{B}]_x
\end{aligned}$$

Idem $\langle\dot{\sigma}_y\rangle = -\gamma[\langle\vec{\sigma}\rangle\times\vec{B}]_y$ and $\langle\dot{\sigma}_z\rangle = -\gamma[\langle\vec{\sigma}\rangle\times\vec{B}]_z$.

2.7 Circuit QED

If the EM field is trapped in a cavity containing single atom, the interaction of the EM field with the single atom is enhanced. The spontaneous decay rate of the atom is strongly suppressed because only certain modes are allowed in the cavity.

When the atom transition frequency is on resonance with the cavity, the atom

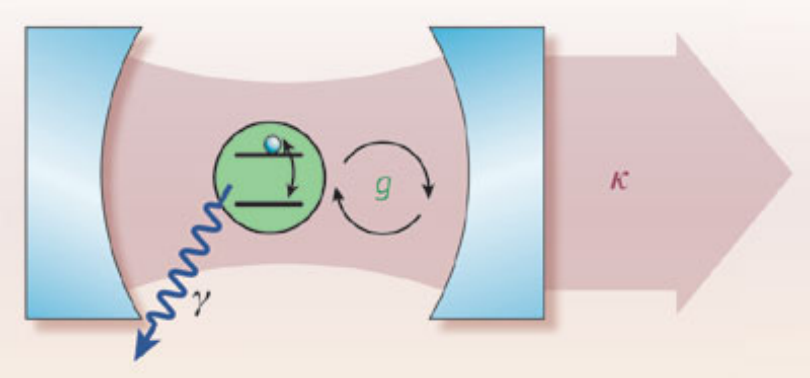

Figure 2.5: The schematic illustration of the Cavity QED [11]. A 2-level atom is trapped inside with decay rate γ and coupled to the quantized photon with decay rate κ. The coupling strength is g.

and the cavity are hybridized and the eigenenergies are degenerated into two energy levels separated by $2g\hbar\sqrt{n+1}$ [21] where n is the number of photons inside of the cavity. The new eigenstates are the superpositions of the atom and the cavity $\frac{1}{\sqrt{2}}(|g\rangle|n+1\rangle \pm |e\rangle|n\rangle)$ (symmetric and antisymmetric states). The photon is exchanged by the atom and the cavity at a frequency $2g\sqrt{n+1}/2\pi$. When $n = 0$, it is called vacuum Rabi oscillations [22]. If the coupling term g is bigger than the atom decay rate (the coupling of the atom to the modes other than the cavity modes) and the photon decay rate κ ($g \gg \kappa, \gamma$), the atom is in the strong coupling regime. In this regime, the vacuum Rabi oscillations can be observed.

If the transition frequency of the atom is nearly on resonance with the cavity modes, it is then significantly shifted by the cavity due to the vacuum fluctuations which is called Lamb shift [23]. And the spontaneous decay of the atom is enhanced by the so called Purcell effect [24].

In our experiments, the cavity consists of a transmission line resonator and two capacitors on each side [25]. The microwave photons are sent through the input ports and trapped by the two capacitors and standing waves are formed. The interaction of the atom with the EM field is maximal if the atom is placed at the antinodes of the EM field. The Hamiltonian of a system with a transmon coupled to the Coplanar wave guide (CPW) resonator is given by

$$\mathscr{H} = \sum_{i=0} \hbar\omega_i |i\rangle\langle i| + \hbar\omega_r(\hat{a}^\dagger\hat{a} + \frac{1}{2}) + \sum_{i=0} \hbar g_{i,i+1}(|i\rangle\langle i+1| + |i+1\rangle\langle i|)(\hat{a}^\dagger + \hat{a}). \tag{2.24}$$

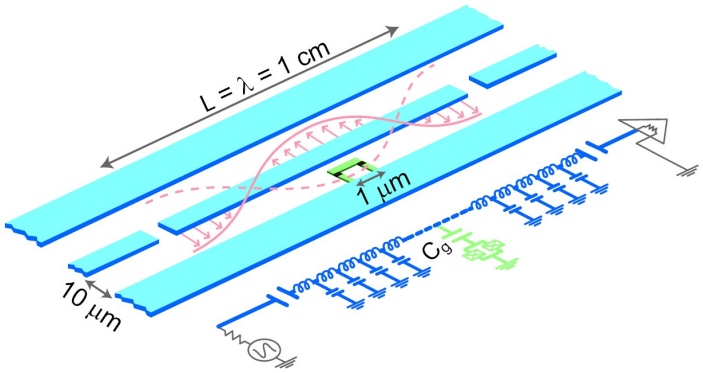

Figure 2.6: The schematic illustration of the Circuit QED [11]. The quantized field is trapped between two capacitors at each end of the resonator acting as reflecting mirrors for photons. A transmon is placed at the antinode of the EM field. The circuit representation of the system is also shown in below.

The first term describes the energy levels of the transmon. The second term is the Hamiltonian of the quantized EM field with creation and annihilation operators $\hat{a}^\dagger, \hat{a}$ of the photon in the cavity. The third term describes the interaction of the transmon with the photon with coupling strength g. The non-neighboring excitation (relaxation) terms are fairly small and can be dropped. In the regime that $g \ll \omega_{i,i+1}, \omega_r$ and detuning $|\Delta| = |\omega_{i,i+1} - \omega_r| \ll \omega_{i,i+1} + \omega_r$, the RWA is valid and the terms $|i\rangle\langle i+1|\hat{a}$ (emission of a photon with de-exicitation of the atom), $|i+1\rangle\langle i|\hat{a}^\dagger$ (absorption of a photon with excitation of the atom) can be neglected. The Hamiltonian can be written as

$$\mathscr{H} = \sum_{i=0} \hbar\omega_i |i\rangle\langle i| + \hbar\omega_r(\hat{a}^\dagger\hat{a} + \frac{1}{2}) + \sum_{i=0} \hbar g_{i,i+1}(|i\rangle\langle i+1|\hat{a}^\dagger + h.c.). \quad (2.25)$$

If we consider only the first two levels, we come to the Jaynes-Cummings model [26]

$$\mathscr{H} = \frac{1}{2}\hbar\omega_{01}\hat{\sigma}_z + \hbar\tilde{\omega}_r(\hat{a}^\dagger\hat{a} + \frac{1}{2}) + \hbar g_{01}(|0\rangle\langle 1|\hat{a}^\dagger + h.c.), \quad (2.26)$$

where $\tilde{\omega}_r$ is the renormalized resonator frequency due to the interaction with higher transmon levels.

2.8 Dispersive limit and Quantum non-demolition measurement

The dispersive limit is the case when the transmon is far detuned from the resonance frequency of the resonator. In the dispersive limit, the Hamiltonian can be written as

$$\mathscr{H} = \frac{1}{2}\hbar\omega_{01}\hat{\sigma_z} + \hbar(\tilde{\omega}_r + \frac{g_{01}^2}{\Delta}\hat{\sigma}_z)(\hat{a}^\dagger\hat{a} + \frac{1}{2}) \quad (2.27)$$

The direct coupling between the qubit and the resonator is strongly suppressed and shows up as a qubit-state dependent frequency shift g_{01}^2/Δ.

The resonance frequency of the resonator is shifted depending on the state of

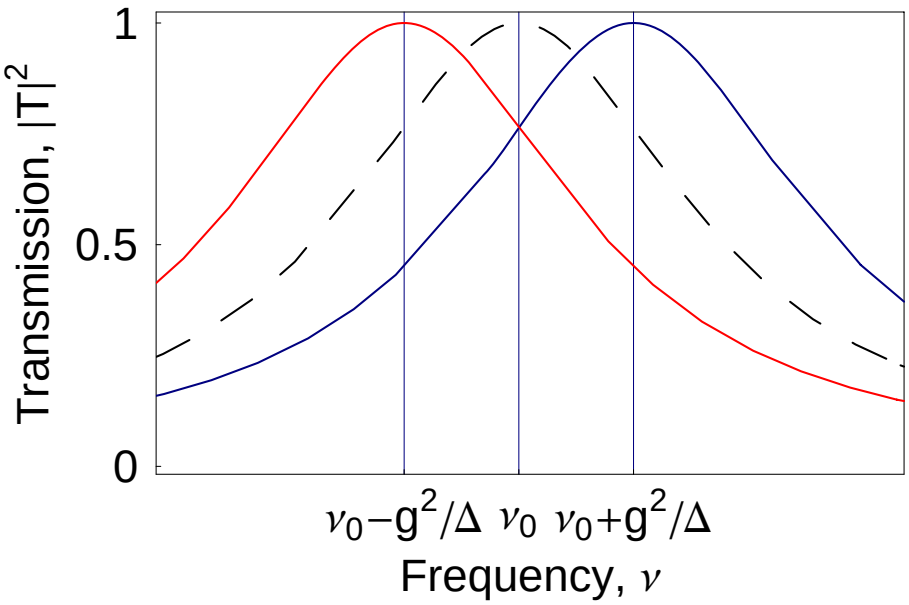

Figure 2.7: The transmission amplitude of the resonator is qubit-state dependent [25]. The dased black line is the transmission spectrum of the resonator without the qubit presence. The red and blue curves are the transmission amplitude spectra of the case when qubit is in ground and excited state respectively.

the qubit (see Fig 2.7) which can be used to determine the state of the qubit. The phase of the transmitted signal $\Phi = \pm\tan^{-1}(2g^2/\kappa\Delta)$ is also qubit-state dependent (see Fig 2.8). In the dispersive limit, the state of the qubit can be read out without destroying its state which is called quantum non-demolition (QND) measurement.

We can rewrite the Hamiltonian (2.27) as

$$\mathscr{H} = \frac{1}{2}\hbar(\omega_{01} + \frac{g_{01}^2}{\Delta} + 2\frac{g_{01}^2}{\Delta}\hat{a}^\dagger\hat{a})\hat{\sigma}_z + \hbar\tilde{\omega}_r(\hat{a}^\dagger\hat{a} + \frac{1}{2}) \tag{2.28}$$

As can be seen in the first term, the qubit transition frequency is renormalized by the Lamb shift term g_{01}^2/Δ due to the field vacuum fluctuations in the resonator. Considering the renormalized qubit frequency $\tilde{\omega}_{01} = \omega_{01} + g_{01}^2/\Delta$ and the photon number $\langle n\rangle = \hat{a}^\dagger\hat{a}$, it is easily to see that the qubit transition frequency is photon number dependent. This is called ac-Stark shift [27] and can be used to determine the photon number inside of the cavity.

If the driving EM field from Eq. (2.20) and (2.22) are also included, the Hamiltonian of the circuit QED with driving field can be written as

$$\mathscr{H} = \hbar\left(\frac{\omega_{01}}{2} + \chi\left(\hat{a}^\dagger\hat{a} + \frac{1}{2}\right) - \frac{\omega}{2}\right)\hat{\sigma}_z + \hbar\tilde{\omega}_r(\hat{a}^\dagger\hat{a} + \frac{1}{2}) + \frac{\hbar\Omega_R}{2}(\cos\phi\sigma_x + \sin\phi\sigma_y), \tag{2.29}$$

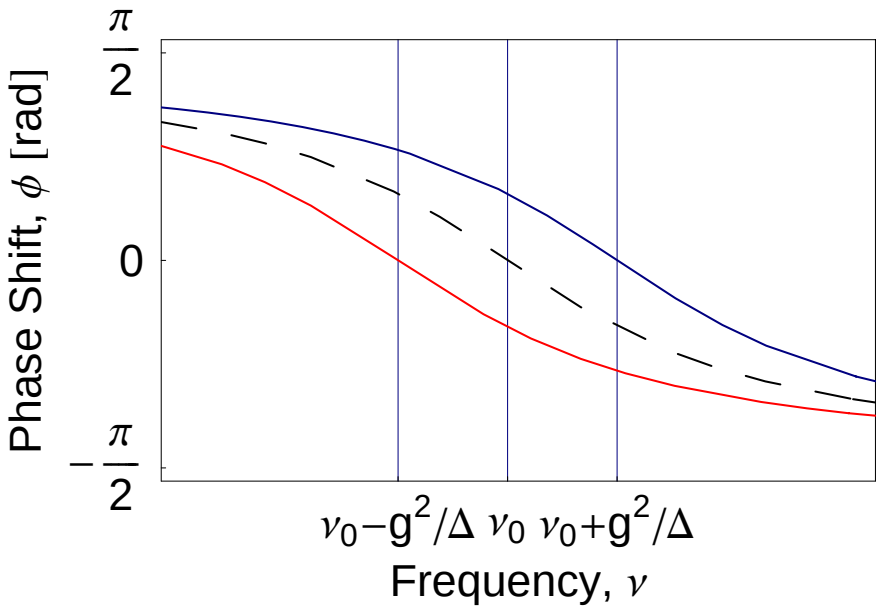

Figure 2.8: The transmission phase of the resonator is qubit-state dependent [25].The dased black line is the transmission phase spectrum of the resonator without the qubit presence. The red and blue curves are the transmission phase spectra of the case when qubit is in ground and excited state respectively.

where $\chi = g_{01}^2/\Delta$ and $\chi\left(\hat{a}^\dagger\hat{a} + \frac{1}{2}\right)$ are the ac-Stark and Lamb terms. If the driving frequency ω equals to the renormalized qubit frequency, the first term vanishes (i.e. the detuning is zero). The second term is the frequency shifted resonator term. The last term describes the σ_x and σ_y rotations controlled by the amplitudes $\Omega_R \cos\phi$ and $\Omega_R \sin\phi$ of the driving pulse.

Chapter 3

Design, fabrication and implementation of the measurement setup

In this chapter, we mainly discuss the measurement setup. In the first section, the signal generation, process and data acquisition are introduced. During measurement the sample is kept at ultralow temperatures (around 20 mK) to prepare the transmon in its superconducting ground state and to suppress thermal and quasiparticle excitations by phonons and the black body radiation ($k_BT \ll \hbar w$). In order to achieve such low temperatures, we use a dilution refrigerator. The principle of a dilution cryostat is briefly presented in the following section. Since in this thesis several new microchips with 16 ports and bigger size (6.6 mm x 7 mm) are designed and fabricated, the corresponding PCB, PCB cover, mount, lid, coils, cryoperm magnetic shields, cables and so on are all redesigned, fabricated and implemented. The specifications of these designs are given in the third section. Later, when the PCB covers and the resonators on the microchip are characterized, a special tool called dip stick and a Network Analyzer are needed. Therefore, in the last section, a brief introduction of these two tools are given.

3.1 Signal synthesis and acquisition

Since the transition frequency of the transmon is in the GHz range, we can take advantage of the mature RF technology. The signal synthesis and acquisition are processed with microwave components (e.g. microwave generators, mixers, attenuators, filters, analog-to-digital converters etc). Signals generated at room temperatures must be attenuated to achieve the single photon level energy (to the order of attowatt 10^{-18} W) and be filtered to minimize the effect of noise from the room temperature electronics. The transmitted signals can then be detected and analyzed.

In the following subsections, The signal synchronization, synthesis, modulation, process, demodulation and acquisition are interpreted consecutively. The

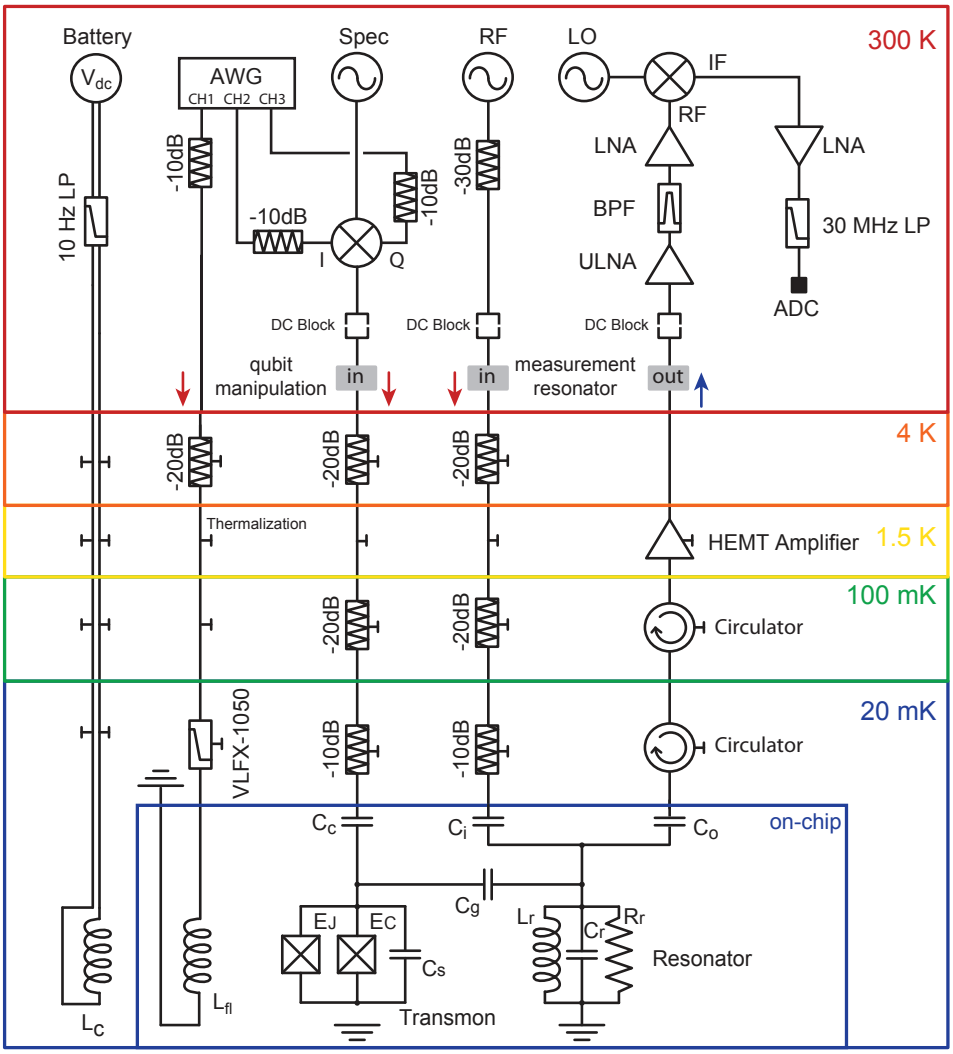

Figure 3.1: The schematic illustration of wiring and cabling configurations at different temperature stages in the cryostat [28]. Here only one transmon and one resonator are displayed.

principle of the important microwave component IQ mixer is also presented.

3.1.1 Signal synthesis and modulation

In general, three kinds of signals are required for the experiments: the continuous microwave signals (RF) for the qubit read-out and qubit spectroscopy, the pulsed coherent microwave signals (Spec) for qubit state operation through charge lines and the pulsed low frequency signals for the fast tuning of the qubit frequency through flux lines.
The first kind of RF signals are generated by the microwave signal generator Agilent (E8257C). The amplitudes of the pulsed coherent Spec signals are modulated with nanosecond resolution by the Tektronix Arbitrary wave generator

(AWG) which provides a sampling rate of $1Gs$ per second on 4 independent analog channels. Thus short envelope of Spec pulses of a few nanoseconds length are generated (for detail, see the section 3.1.2). The third type of signals are provided by AWG as shown in the Fig 3.1.
The synchronization of signal synthesis and signal acquisition is achieved by employing the 4 digital markers provided by the AWG. A Rubidium atomic clock is used to avoid phase accumulation during the signal synthesis and acquisition processes. The phase drifts and phase instabilities can be eliminated by phase locking the whole process with the 10 MHz Rubidium frequency standard.

3.1.2 IQ-mixer

The operations of the qubit state is achieved by sending a sequence of pulses through the charge lines. The accurate preparation and control of the qubit state need the precise control of the shape (amplitude, phase and frequency) of the short pulsed signal. This can not be achieved in the frequency range of GHz without the help of an AWG and an IQ mixer.
The IQ-mixer (up converter) consists of one LO input port, two I and Q input

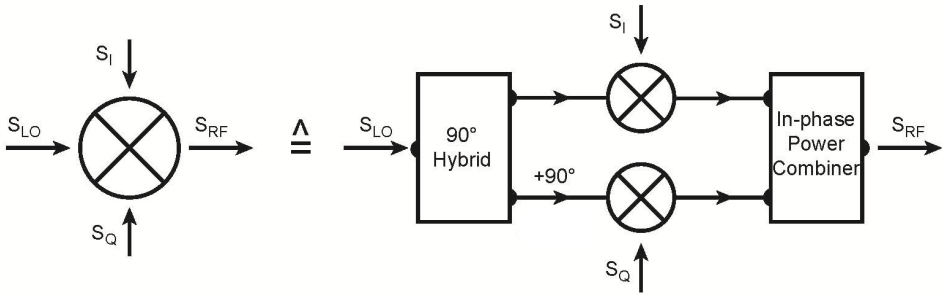

Figure 3.2: The schematic illustration of the IQ mixer.

ports, one RF output port, a power divider and a 90 degree phase shifter.
The signal IF provided by the AWG that is upconverted is split into in-phase signal S_I and quadrature signal S_Q with phase shift φ. The two signals are sent through I and Q ports of the mixer and multiplied to two split phase shifted local oscillator (LO) high frequency signals respectively (one of them is 90 degree shifted). The two signals are then hybridized inside of the mixer into the output signal S_{RF}. The LO signal has a fixed amplitude A_{LO} and frequency ω_{LO}. We define its phase zero. The signals S_I and S_Q have the same time dependent amplitude $A_{IF}(t)$ and phase $\phi_{IF}(t)$. The final output signal S_{RF} is deduced by some trigonometric calculations as shown in below:

$$S_{LO} = A_{LO}\cos(w_{LO})t$$

$$S_I = A_{IF}(t)\cos(w_{IF}t + \phi_{IF}(t))$$
$$S_Q = A_{IF}(t)\cos(w_{IF}t + \phi_{IF}(t) + \varphi)$$

. The output signal is given by simple calculations:

$$\begin{aligned} S_{RF} &= \frac{A_{LO}}{\sqrt{2}}[\cos(w_{LO}t)S_I + \cos(w_{LO}t + \frac{\pi}{2})S_Q] \\ &= \frac{A_{LO}A_{IF}(t)}{\sqrt{2}}[\cos(w_{LO}t)\cos(w_{IF}t + \phi_{IF}(t)) \\ &+ \cos(w_{LO}t + \frac{\pi}{2})\cos(w_{IF}t + \phi_{IF}(t) + \varphi)] \\ &= \frac{A_{LO}A_{IF}(t)}{\sqrt{2}}[\cos(w_{LO}t)\cos(w_{IF}t + \phi_{IF}(t)) \\ &- \sin(w_{LO}t)\cos(w_{IF}t + \phi_{IF}(t) + \varphi)]. \end{aligned}$$

Two special cases with $\varphi = \pm\pi/2$:

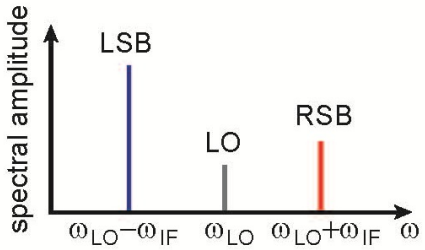

Figure 3.3: The left sideband LSB and the right sideband RSB around the L.O. frequency.

a)

$$\varphi = \frac{\pi}{2}; S_{RF} = \frac{A_{LO}A_{IF}(t)}{\sqrt{2}}\cos[(w_{LO} - w_{IF})t - \phi_{IF}(t)).$$

b)

$$\varphi = -\frac{\pi}{2}; S_{RF} = \frac{A_{LO}A_{IF}(t)}{\sqrt{2}}\cos[(w_{LO} + w_{IF})t + \phi_{IF}(t)).$$

In these cases S_{RF} located totally in lower band $(w_{LO} - w_{IF})$ and in upper band $(w_{LO} + w_{IF})$, respectively.
Therefore, simply by tuning the phase shift φ, the amplitude of the signals on the two sidebands $w_{LO} \pm w_{IF}$ can be adjusted. Any frequency around w_{LO} within the bandwidth of the mixer can be generated. The frequency of IF signal can be chosen to be zero or finite. Besides, the amplitude of the output signal S_{RF} can be controlled by $A_{IF}(t)$ and the phase can be controlled by $\phi_{IF}(t)$.

3.1.3 Signal in cryostat

As can be seen from the Fig 3.1, the RF and Spec signals are first attenuated -30 dB at room temperature and then a DC blocker is employed to banish

the ground loops before signals entering the cryostat. The signals are further filtered and attenuated (-20 dB attenuated at 4K stage and 100 mK stage and -10 dB attenuated at 20 mK stage) in the cryostat to some attowatt order before entering the resonator.
The cables inside of the cryostat are bent to suppress the contraction and movement of the inner materials due to the thermal variations. Considering the fact that the heat conductivity of the copper is larger than the one of the stainless steel, we use stainless steel coaxial cables connecting different cooling stages to minimize the heat transfer from the room temperature to the cooling stages and between different cooling stages. At the same temperature stage (e.g. of the mixing chamber), the cables are mainly Cu-Cu type to minimize the signal loss. Due to its low electrical conductivity, the steel coaxial cable in the readout line is replaced by a superconducting Niobium Titanium coaxial cable (low heat conductivity and low loss) to minimize signal losses.
Applying two many attenuators along the flux lines would cause overheating problem, because a significant current flows through the flux lines. Therefore only one attenuator (-10dB) at room temperatures and one attenuator (-20dB) at the 4K stage are employed. A low pass filter VLFX from company Mini-circuits is placed at the 20 mK stage to suppress high frequency flux noise. Because the output signal is feeble, the attenuators are not practical for the output cabling. By employing two circulators, the incoming thermal radiations are guided to a different branch 50Ω termination and absorbed without influencing the transmitting signals.
At the 1.5 K stage, a low noise amplifier LNA from the company LNF (bandwidth 4-8 GHz) and a LNA from Caltech (bandwidth 1-14 GHz) are employed. The power gain of the amplifiers is around 30 dB.

3.1.4 Signal demodulation and acquisition

The information of the qubit state is encoded in the amplitude and phase of the transmitted signals through the output capacitor. The transmitted signals are in the frequency range of 10 GHz. According to Nyquist sampling theorem (which states that in order to perfectly reconstruct a band limited analog signal, the sampling rate should be larger than twice the highest frequency of the analog signal), the sampling rate is required to be higher than 20GHz. This is technically uneasy and could be avoided by down-converting the transmitted signals to an appropriate frequency range. The down-conversion of the transmitted signals (inverted process of upconversion in previous sections) is achieved via an IQ demodulator where the transmitted RF signals are split and mixed with the LO signals which usually have an offset of ν_{IF} =10 MHz or 25 MHz from the transmitted measurement signals. The input ports I and Q in the upconverting case now act as output ports. In the case that the split LO signals are $\pi/2$ phase shifted, the output signals S_I and S_Q can be written as

$$S_I(t) = \frac{A_{LO}(t)A_{IF}(t)}{\sqrt{2}}[\cos(2\pi\omega_{IF}t) - \cos(2\pi(2\omega_{RF} + \omega_{IF})t)]. \tag{3.1}$$

$$S_Q(t) = \frac{A_{LO}(t)A_{IF}(t)}{\sqrt{2}}[\sin(2\pi\omega_{IF}t) - \sin(2\pi(2\omega_{RF} + \omega_{IF})t)]. \quad (3.2)$$

The output I an Q quadratures can then be amplified, low-pass filtered (the fast oscillating term can be filtered out), digitized and averaged (by the Acquiris with 1GS/s sampling rate on each of its two channels) conveniently. The amplitude of the input signal is recovered by $\sqrt{I^2 + Q^2}$ and the phase is obtained by $\arg(I + iQ)$.

3.2 Dilution refrigerator

Our sample is placed at 20 mK in the superconducting regime of the transmon. The low temperature is achieved by employing a conventional dilution refrigerator. The schematic illustration of the dilution refrigerator is shown in the Fig 3.4.

The liquid ^{4}He (boiling point 4.23 K at 1 atm) is continuously pumped from the 1K pot. After the temperature of the 1 K pot has attained around 1.5 K, a mixture of ^{3}He (boiling point 3.19 K at 1 atm) and ^{4}He gas is first precooled and liquefied at the heat exchanger attached to the 1 K pot condenser and then is pumped using a rotary pump. The whole dilution refrigerator is getting colder and colder. The level of the liquefied mixture of ^{3}He and ^{4}He in the mixing chamber increases until it arrives the still. When the pressure in the still is fairly low, a roots pump is turned on. The temperature in the still drops to about 700 mK.

The incoming gas flowing through the heat exchangers attached to the 1K pot and to the still gets cooled to below 800 mK. The two isotopes separate into two phases spontaneously in the mixing chamber: the concentrated phase rich in ^{3}He (thus lighter and floats on the top) and the dilute phase rich in ^{4}He (thus heavier and sinks in the bottom).

Since the boiling point of the ^{3}He is lower than the one of ^{4}He, the gas pumped out in the still is mainly ^{3}He atoms. Consequently the ^{3}He atoms are moving from the concentrated phase to the dilute phase and from the mixing chamber to the still due to the osmotic pressure gradient. As the ^{3}He atoms are "evaporated" from the upper concentrated phase to the lower dilute phase which is energy-consuming, the temperature in the mixing chamber is further lowered. However, as the temperature decreases, the solubility of the ^{3}He in the ^{4}He medium reduces as well. It is important that even at extremely low temperature (below 20 mK) the solubility remains as large as 6.4%. Otherwise, the cooling process could be stopped due to the lack of "evaporation" of ^{3}He. The temperature in the mixing chamber can achieve to around 20 mK after around ten hours circulation.

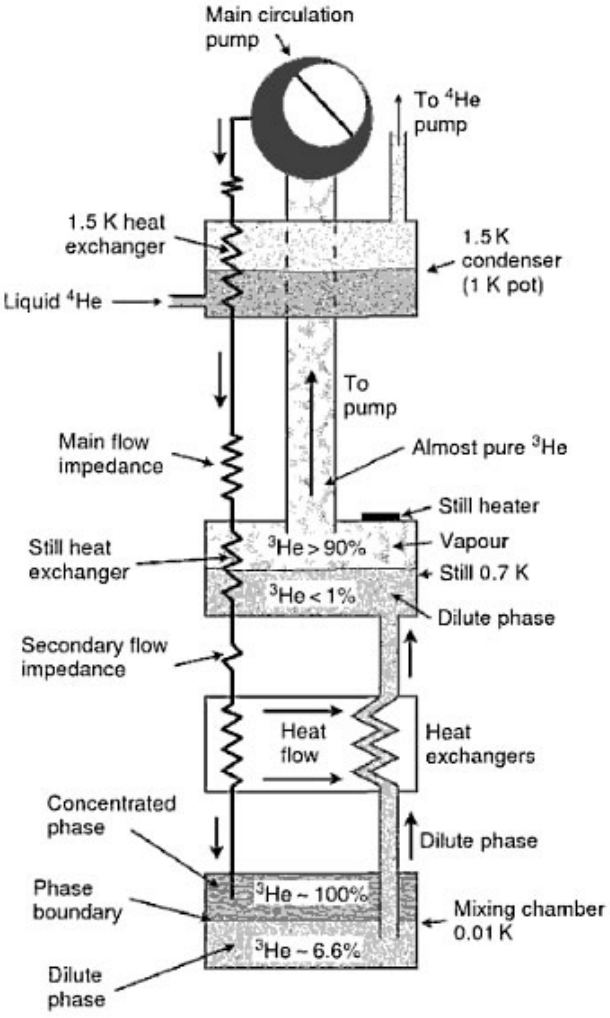

Figure 3.4: The schematic illustration of a classic dilution refrigerator[29].

3.3 Sample

Our samples consist of a microchip that is glued on a printed circuit board (PCB). The ports on the microchip are bonded to the coplanar wave guide (CPW) on the PCB. The PCB is fixed on the mount which has a groove on its backside (see Fig 3.5). The small coils are loaded inside of the groove and the big coil is fixed on the backside of the mount. A PCB cover is added in between the PCB and the lid to shift the resonance frequencies of the spurious cavity modes to higher frequency (over 20 GHz). The whole sample is then enclosed by two cryoperm (high permeability alloy) magnetic shields which is not shown in the Fig 3.5 (in our first measurements only one cryoperm magnetic shield is employed).
The mount, the PCB cover, the lid, the cryoperm magnetic shields and the coil holders are all modeled in 3D using the software Autodesk Inventor Pro-

fessional 2011. The PCBs are designed using AutoCAD Mechanical 2011 and the microchips are designed using the software Wolfram Mathematica 8.

In the following sections, the specifications of the designs will be shown.

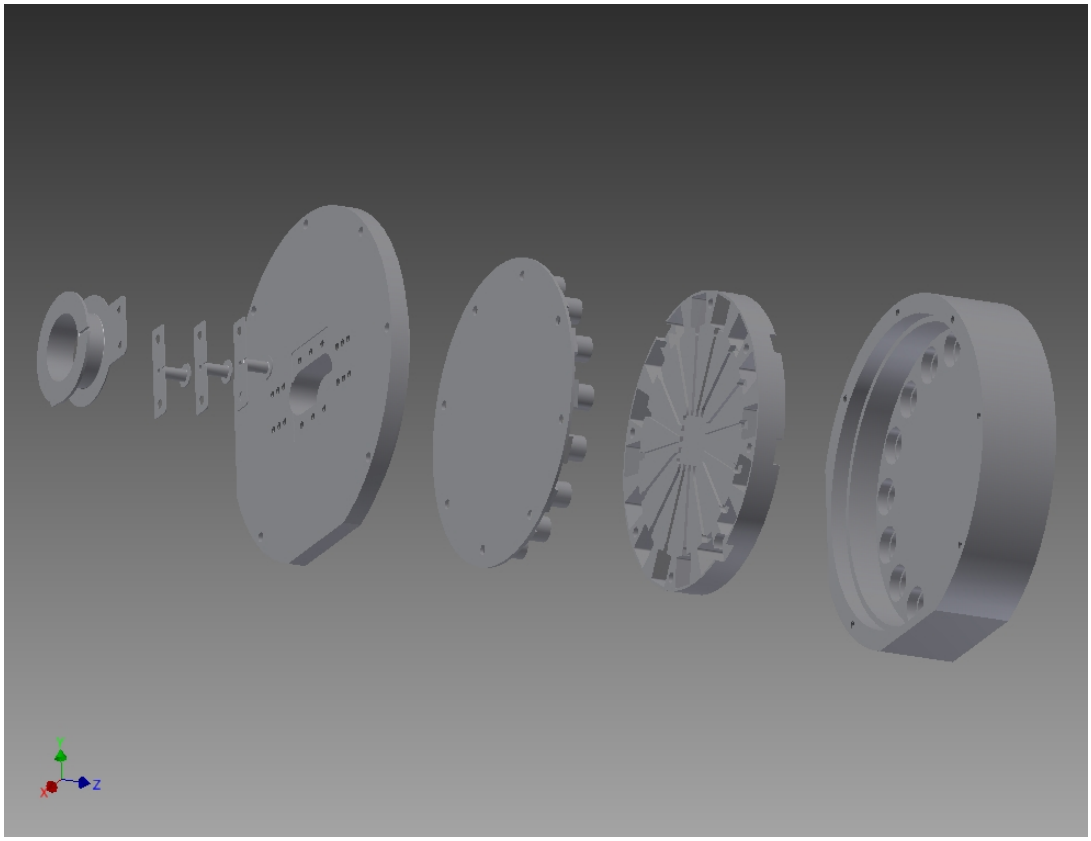

Figure 3.5: The illustrative CAD design of the sample. It is an assembly of a big coil, three parallel arranged small coils (in our first experiments only two small coils are implemented), mount, PCB, microchip (not shown in the figure), PCB cover and lid (from left to right).

3.3.1 Microchips and PCB

Different kinds of microchips of the size 7 mm x 6.6 mm (the resonance frequency of the cavity is around 20 GHz) have been designed and are shown in below.

The microchip M20B1 is shown in Fig 3.6. It has two crossed resonators with quality factor Q= 4000. Three transmon gaps are placed at the ends and cross of the resonators. Each transmon gap is equiped with a charge line and a flux line. Some other microchips of the same design but of different quality factors have also been designed.

The microchip M20D1 is shown in Fig 3.7. It has three crossed resonators with quality factor Q= 2000. Four transmon gaps are placed at the ends and crosses of the resonators. Each transmon gap is equiped with a charge line and a flux line.

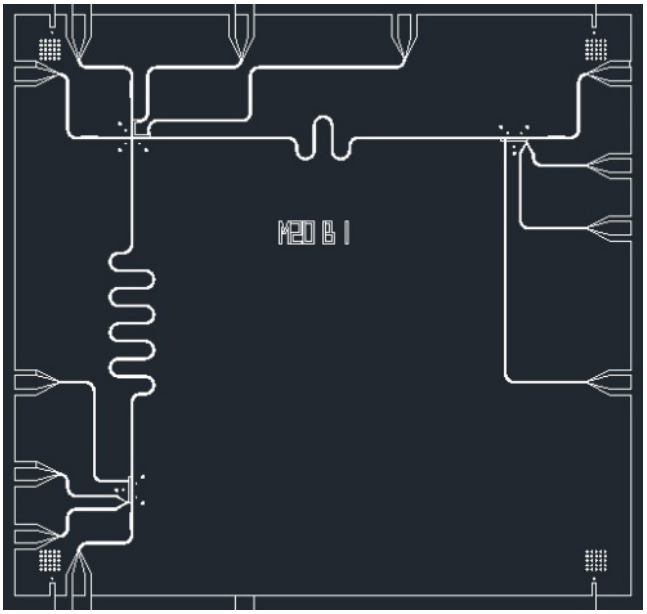

Figure 3.6: The mask design of the microchip M20B1. The resonance frequencies of the left and upper resonators are 7.5 GHz and 9.5 GHz respectively.

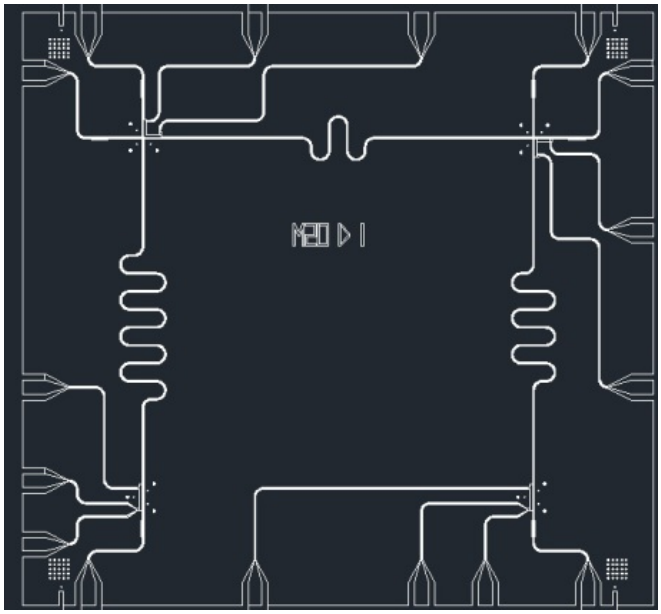

Figure 3.7: The mask design of the microchip M20D1. The resonance frequencies of the left, upper and right resonators are 7.5 GHz, 9.5 GHz and 8.5 GHz respectively.

Since currently in our cryostat only two cold amplifiers are implemented (only two read-outs are possible), the type of three crossed resonators (upper one with open ends) M20H1 is also designed (see Fig 3.8).
The type of three crossed resonators (upper one with open ends) with big transmon gaps is shown in Fig 3.11.

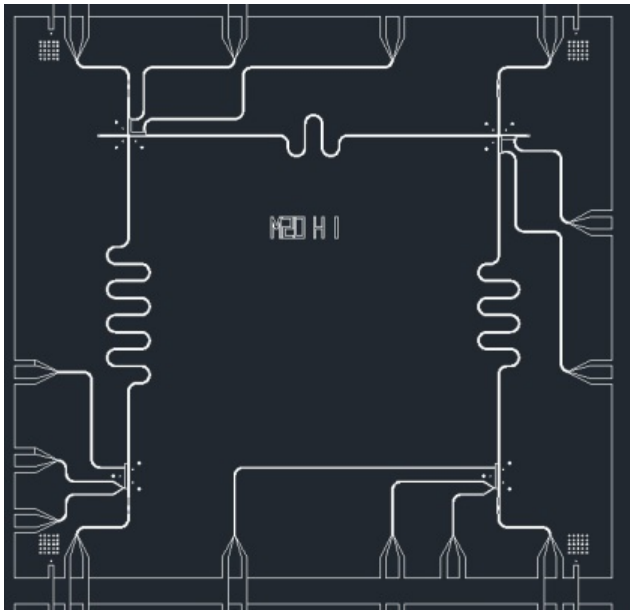

Figure 3.8: The mask design of the microchip M20H1. The resonance frequencies of the left, upper and right resonators are 7.5 GHz, 9.5 GHz and 8.5 GHz respectively. The upper resonator is open ended.

The types of four crossed resonators M20M1, M20N1 and M20O1 (see Fig

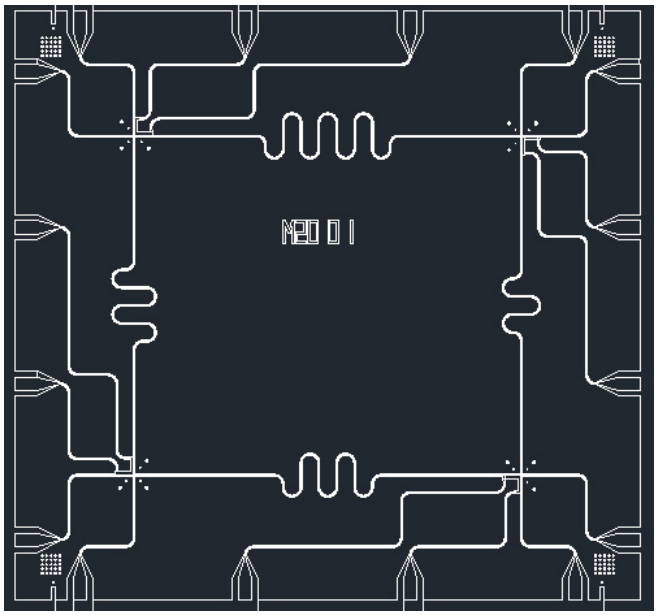

Figure 3.9: The mask design of the microchip M20O1. The resonance frequencies of the left, upper, right and lower resonators are 7.5 GHz, 9.5 GHz, 8.5 GHz and 10.5 GHz respectively.

3.9) have the same resonator and transmon gap designs but different quality factors (8000, 2000 and 4000 respectively).

The type of one resonator with seven qubits M20Q1 is shown in Fig 3.10. The

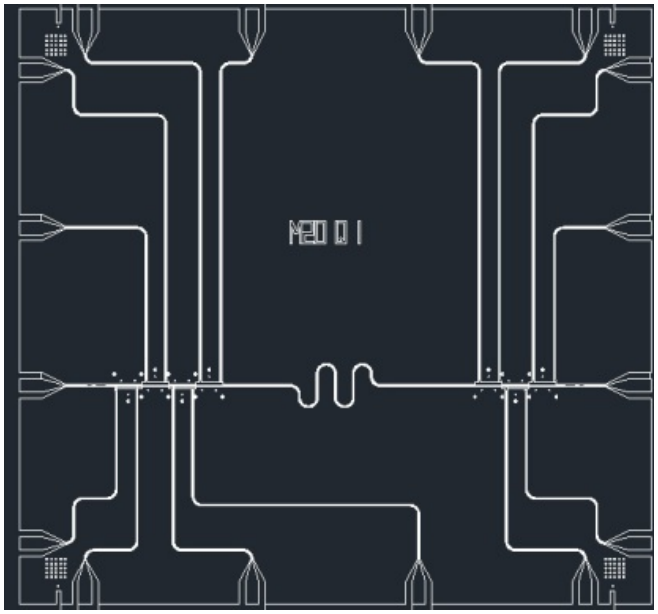

Figure 3.10: The mask design of the microchip M20Q1. The resonance frequenciy of the resonator is 9 GHz.

gate lines on these microchips have the comparable length of the resonator. Since the launchers of the gate lines are connected to the PCB using Al bonds which results in some mismatch, these gate lines act somehow as a resonator. This could induce unwanted resonances near the resonance frequencies of the resonator.
Some other different kinds of microchips are also designed and fabricated which are to be shown in chapter four.

Here we describe in detail the microchip M20K2 that we used in our first experiments. As can be seen from the Fig 3.11, the three crossed resonators are capacitively connected to their input and output ports (since currently only two amplifiers are implemented in our experiments, only two readouts are possible. Thus the input and output ports of the upper resonator are taken out). The resonance frequencies of the left, upper and right resonators are designed to be 7.5 GHz, 9.5 GHz and 8.5GHz respectively. The resonance frequencies of the crossed resonators are designed to be different to avoid unwanted resonance caused by cross talking of neighboring resonators. The length of the resonators depends on the frequency desired and the effective dielectric constant ϵ_{eff}.

$$f_0 = \frac{c}{\sqrt{\epsilon_{\text{eff}}}} \frac{1}{2l}, \tag{3.3}$$

where l is the length of the resonator and f_0 is the desired resonance frequency. The meandering shape of the resonators is due to the small size of the microchip (6.6 mm x 7 mm).
The niobium film is deposited on the monocrystalline sapphire substrate and

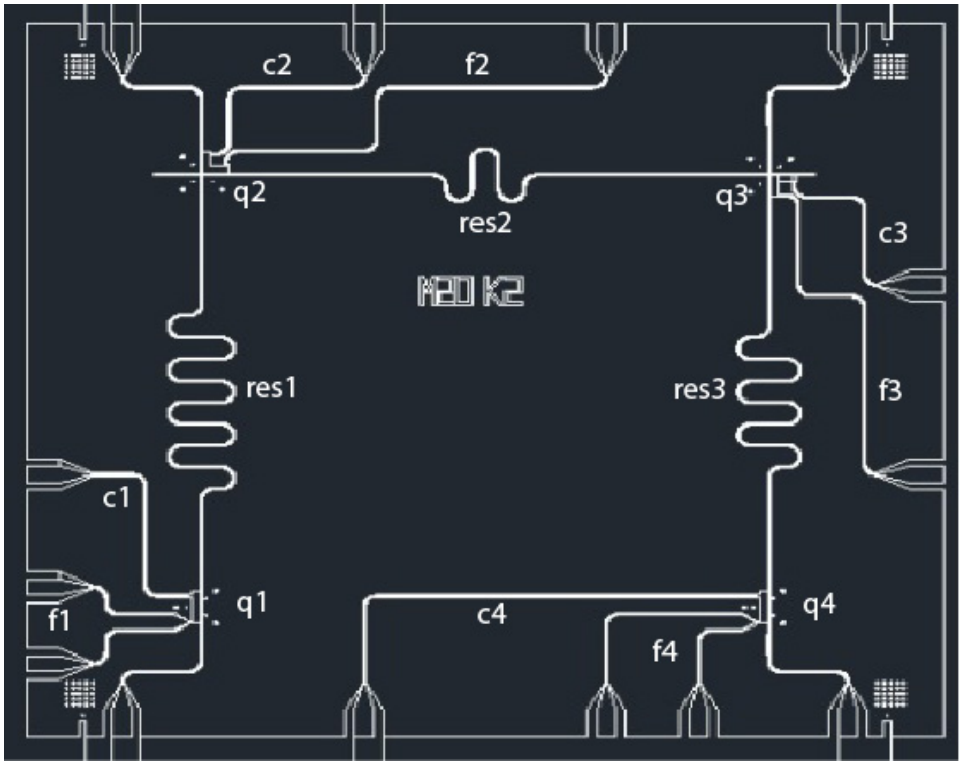

Figure 3.11: The mask of the microchip M20K2 with three crossed resonators res1, res2, res3 and four qubits q1, q2, q3, q4. The charge lines c1, c2, c3, c4 and the flux lines f1, f2, f3, f4 for the control of each qubit are also indicated in the figure.

the transmission line resonators are then etched by using a standard optical lithography technique. In our sample, the resonators are made of Niobium (T_c=9.2 K) instead of Aluminum (T_c=1.2 K) for the reason that the test of the resonators and of the PCB cover (see next chapter) can be realized at relatively high temperature (liquid helium temperature 4.2 K). Additionally, the quality factor is found to be less sensitive to the variation of the applied magnetic field using Niobium film than using Al film [30]. The resonator can couple to its input and output ports via either gap or finger capacitors (finger capacitors in our case).

The photons are essentially transmitted in and out of the resonator cavity through the input and output capacitors. However the photons can be temporally trapped inside of the cavity and the input and output gap capacitors act as mirrors. The photon decay rate $\kappa = \omega_r/Q$ is determined by both the resonator frequency and the quality factor Q. The quality factor Q is given by

$$\frac{1}{Q} = \frac{1}{Q_{\text{int}}} + \frac{1}{Q_L}. \tag{3.4}$$

The CPW resonators with resonance frequency 5-15GHz ($\hbar\omega \gg k_B T$ at $T \approx$ 20 mK) can achieve high internal quality factor Q_{int}=10^6 determined by the intrinsic dielectric losses. High internal quality factor indicates low atom decay

rate γ.
The loaded quality factor Q_L can be engineered by adjusting the capacitances at both ends of the resonator. Large gap capacitor leads to small capacitance, large quality factor and long photon lifetime. Finger capacitor leads to large capacitance, small quality factor and short photon lifetime which is beneficial for fast measurements ($\kappa = \omega/Q_L$ =1 MHz). For a symmetrically coupled resonator, the loaded quality factor Q_L scales with the reverse of the capacitance square in the overcoupled case and saturates at the internal quality factor in the undercoupled case[31, 30]. To enhance the rate of the signal transmitted through the output capacitor, the output capacitance is usually designed to be larger than the input capacitance. But in our experiment we fabricated each resonator with the same finger capacitors at its two ends.

The signal transmitted power is determined by how much the impedance

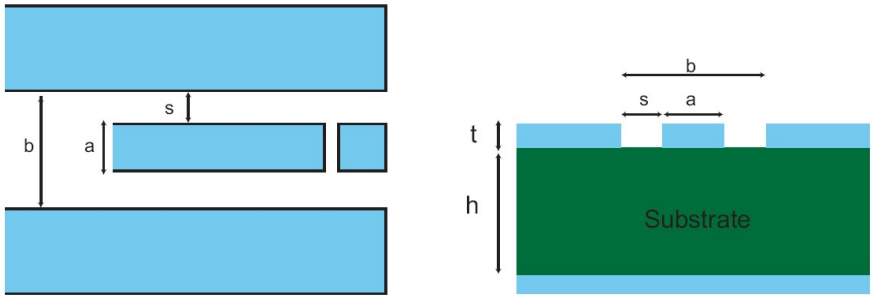

Figure 3.12: The top and side views of the CPW [28]. The width of the center conductor is $a = 10$ μm and separated from the lateral ground planes by the $s = 4.5$ μm wide gaps.

match between the resonator and the transmission line. The characteristic impedance of the CPW resonator can be calculated as $Z = \sqrt{L_l/C_l}$ where L_l and C_l are the capacitance and inductance per unit length of the resonator. L_l and C_l depend on the geometry of the CPW resonator (the ratio of the center conductor width a to the gap width b between the ground planes) and the dielectric constant of the substrate [31]. The ratio of b/a together with the sapphire substrate results in the Z=50 Ω impedance which matches the impedance of the conventional microwave components.
The transmons are fabricated in the transmon gaps (see Fig 3.14 and 3.16) by electron beam lithography technique after the fabrication of resonators.

The ground planes separated by the gate lines and resonators are bonded using Al bonding wires. At high frequency, the impedance of the Al bonds is high $Z = i\omega L$. Several bonds in parallel are used to reduce the impedance. As can be seen from Fig 3.13 and 3.14, the resonator res1 is separated by res2 and connected using Al airbridges.

The advantage of using the transmon is its large electric dipole moment d and using the 1D transmission line resonator as the cavity benefits from the large vacuum electric field E_0 (10^6 larger than the one in 3D microwave cavity). Both of them contribute to the large coupling strength between the qubit and

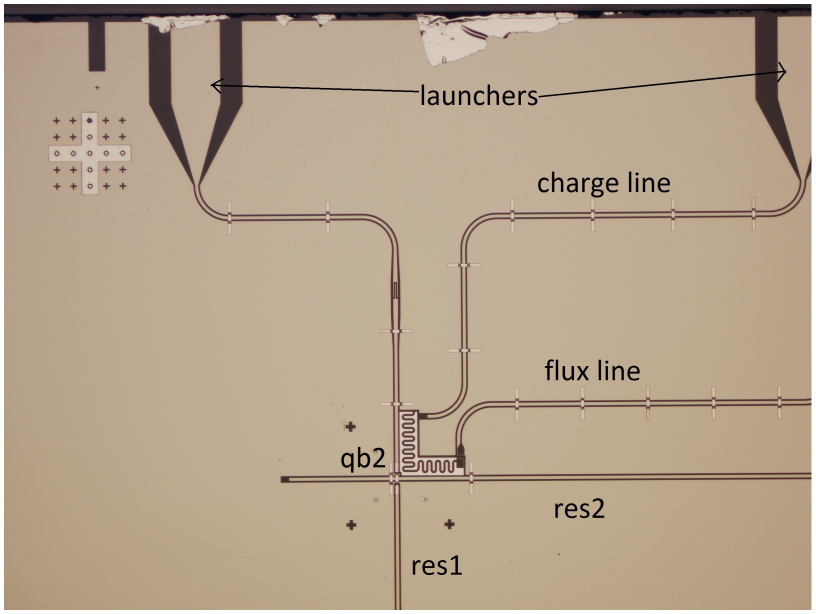

Figure 3.13: The transmon q2 is fabricated inside of the transmon gap on the microchip M20K1. The launchers, the flux line and the charge line are indicated.

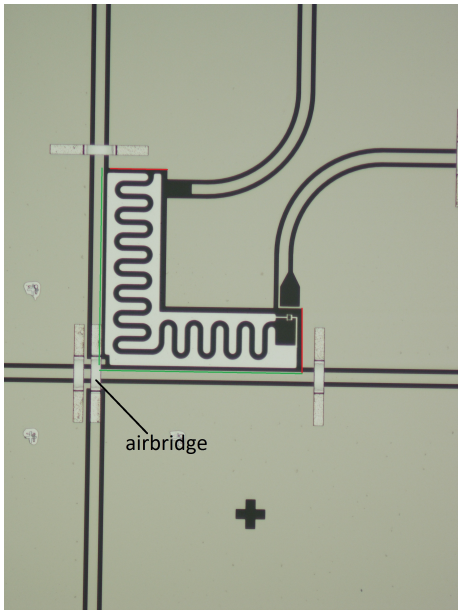

Figure 3.14: The zoom in of the transmon in the previous picture. The dimension of the big transmon gap is shown. The length of the red lines are 60 μm (for the normal gap it is 30 μm). The length of the green lines are 200 μm (the same for the normal ones).

the resonator as can be seen from [11]

$$g = \frac{dE_0}{\hbar}. \tag{3.5}$$

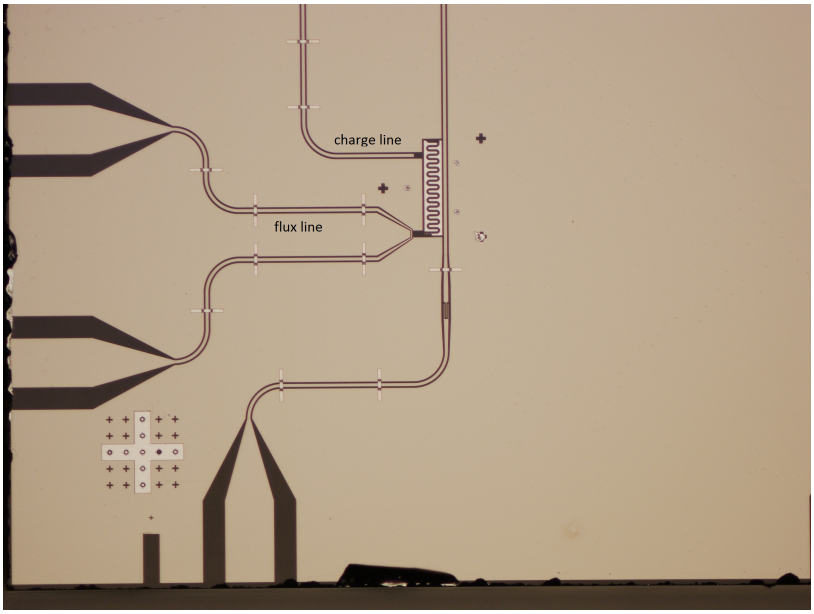

Figure 3.15: The transmon q1 fabricated inside of the transmon gap.

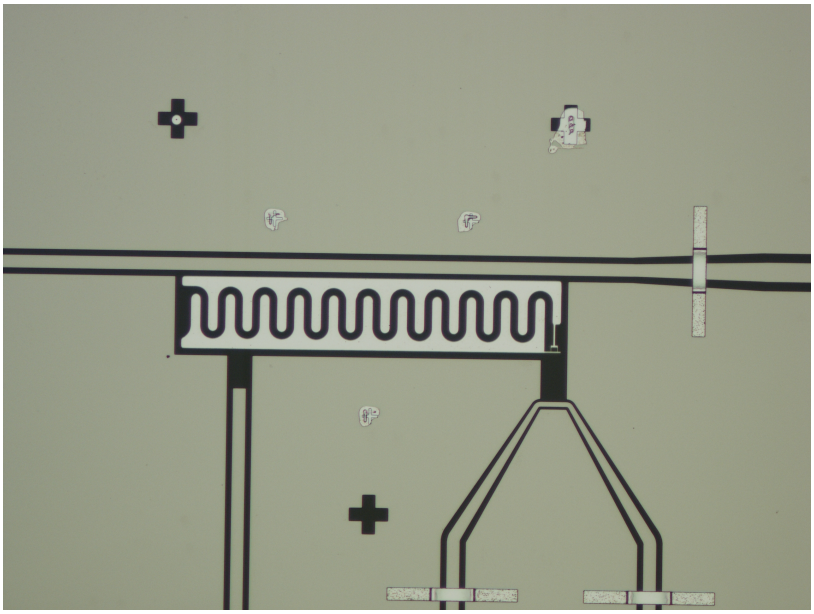

Figure 3.16: The zoom in of transmon qb1. The flux line is designed to be far from the capacitor of the transmon to suppress capacitively coupling with transmon. The size of the transmon gap is of 300 μm x 60 μm (for the normal ones 300 μm x 30 μm.).

The coupling strength of the qubit to the resonator can easily attain to $g/\pi \approx$ 300 MHz while keeping the photon decay rate κ and atom decay rate γ below 1 MHz. The strong coupling regime $g \gg \kappa, \gamma$ is easily achieved in this case. Since the magnetic flux created by the coils can only be slowly changed, the fast tuning of the qubit transition frequency is not realizable by coils.

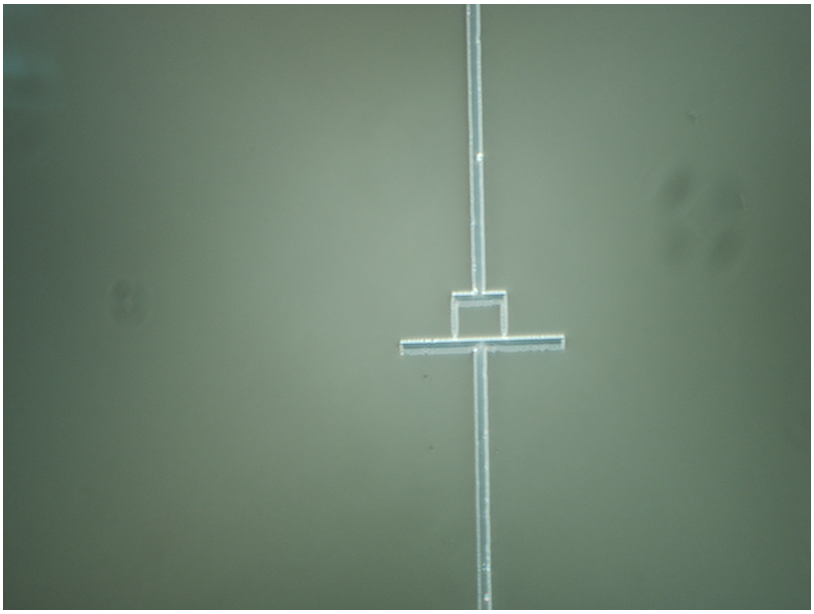

Figure 3.17: The zoom in of the SQUID loop of the transmon.

Nowadays for the purpose of individually control the qubit's state and fast tuning the qubit transition frequency, the charge lines and flux lines are implemented near each transmon. The charge lines c1, c2, c3, c4 and flux lines f1, f2, f3, f4 of each transmon are indicated in the Fig 3.11.

The microchip is then glued in the 7.4 mm x 7 mm cutout of the PCB (see

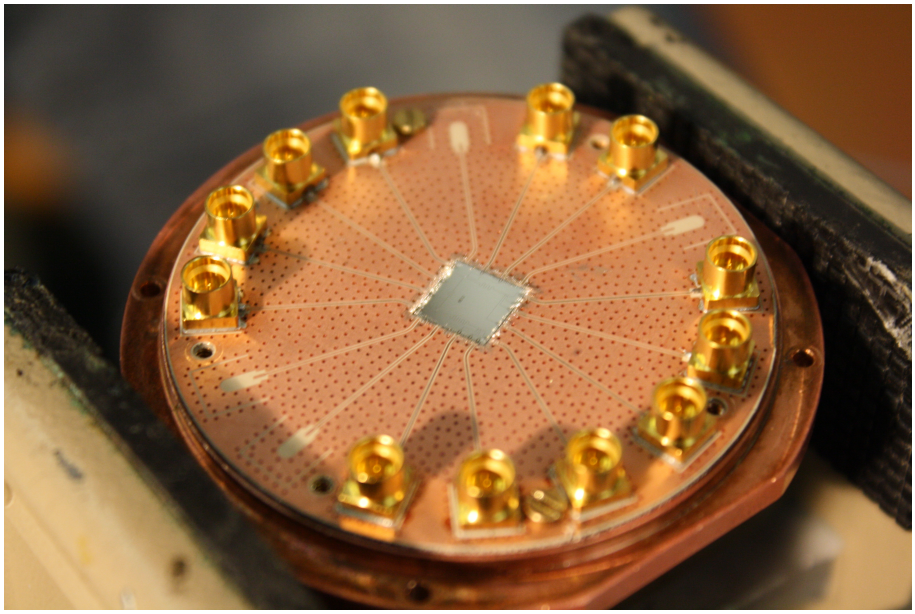

Figure 3.18: The microchip is glued on a PCB and some SMP connectors are soldered on the PCB.

Fig 3.18) after the soldering of SMP connectors on the PCB. The launchers are bonded to the coplanar waveguide (CPW) on the PCB and the ground planes of the microchip are bonded to the ground planes on the PCB by using Al wire bonds. The SMP connectors are soldered on the PCB board to join the CPW with the incoming cables (the cables are ended with SMP connectors and connected to the SMP connectors on the PCB by bullets).

3.3.2 Mount, PCB cover, lid and cryoperm magnetic shields

Figure 3.19: The pictures in the upper row are the recto and verso sides of the lid. The pictures in the lower row are the recto and verso sides of the mount.

The PCB with microchip glued on is fixed on a copper mount and covered by a copper lid (see Fig 3.14). The groove on the back side of the mount is for the coils. The holes on the lid allow the cables enter and connect to the SMP connectors on the PCB. Two magnetic shields made of high permeability metal alloy cryoperm are placed outside of the copper cavity. Previously two cryoperm magnetic shields are mounted directly outside of the sample holder. Currently due to the large size of the sample holder, only one of them (see Fig 3.20) is mounted directly outside of the sample holder. Another big one is placed inside of the dewar of the cryostat since there is no more space in the 20 mK stage (not implemented in our first experiments).

3.3.3 Coils

The qubit state is controlled by varying length, amplitude and phase of microwave pulses sent through the charge lines to the qubit (see first section of

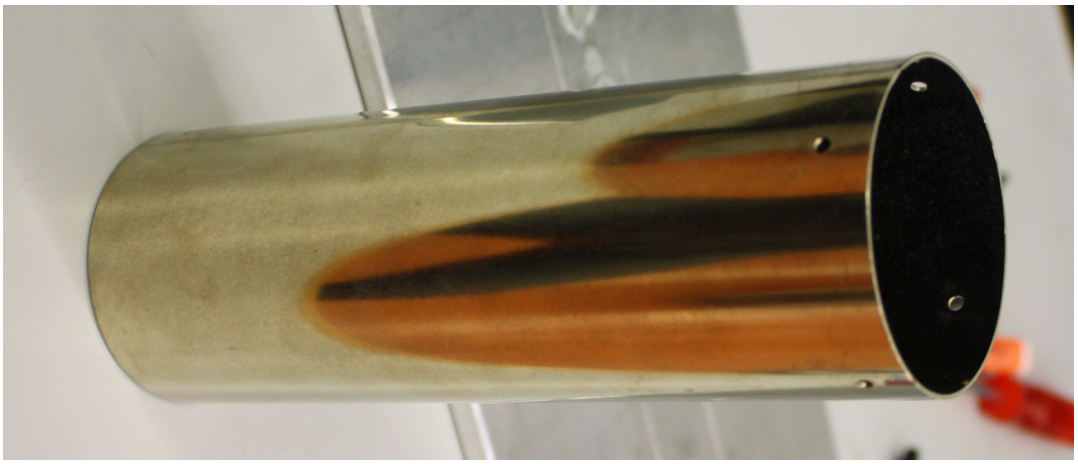

Figure 3.20: The cryoperm magnetic shield.

this chapter). The fast tuning of the magnetic field is achieved using the flux lines. Since the cables carrying the currents to the flux lines are not made of superconducting materials, only short pulsed and relatively low current from AWG can be sent through the flux lines on the chip to avoid heating the system. Thus the magnetic fields through the qubits are mainly created by the external magnetic coils which can only be slowly changed.
In the version of the 8-port microchip, as many as three qubits can be implemented on the microchip and can be controlled individually and simultaneously by three coils right below the microchip on the mount. In order to control the transition frequencies of all four qubits on our new microchip individually and simultaneously, four coils are required. Consequently, another coil is needed to be mounted on the PCB mount.
In order to control the qubit frequency, the coils should be placed right below the microchip. Due to the limited size of the microchip, the coils are placed in double layers. The two small coil holders (radius = 2 mm, length = 4.4 mm) are placed in parallel and the big coil holder (radius = 6 mm, length = 4 mm) is placed on the second layer. In the 16-port microchip, the two small coil holders are replaced by three small coil holders arranged in parallel (radius = 1 mm, length = 4.4 mm) while the big coil holder is kept as the same size and at the same position.
The four coil holders for 16-port microchip are arranged in the way shown in the Fig 3.22.
The coil holder is made of epoxy to avoid potential leakage of coil current to the coil housing. In addition, the epoxy housing could thermalize the coil wires in the cryostat. The winding superconducting wire (to avoid heating) is fine diameter copper stabilized SC-T48B-M-0.025mm wire produced by Supercon Inc. The center superconducting NbTi (Tc=9.2K) filament is surrounded by high conductivity cryogenic grade copper to provide stabilization. The diameter of the inner bare filament, the copper filament and the insulated filament are 0.015mm, 0.025mm and 0.036mm respectively.

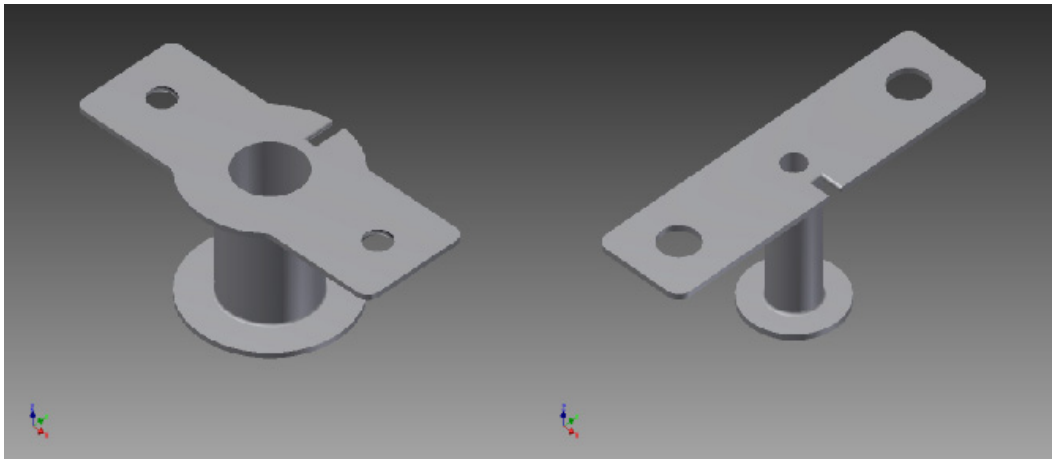

Figure 3.21: The illustrative CAD designs of the small coil holder for 8-port microchip (on the left) and for 16-port microchip (on the right). The coil holder consists of a cylindrical housing and a pair of wings used to fix it on the mount.

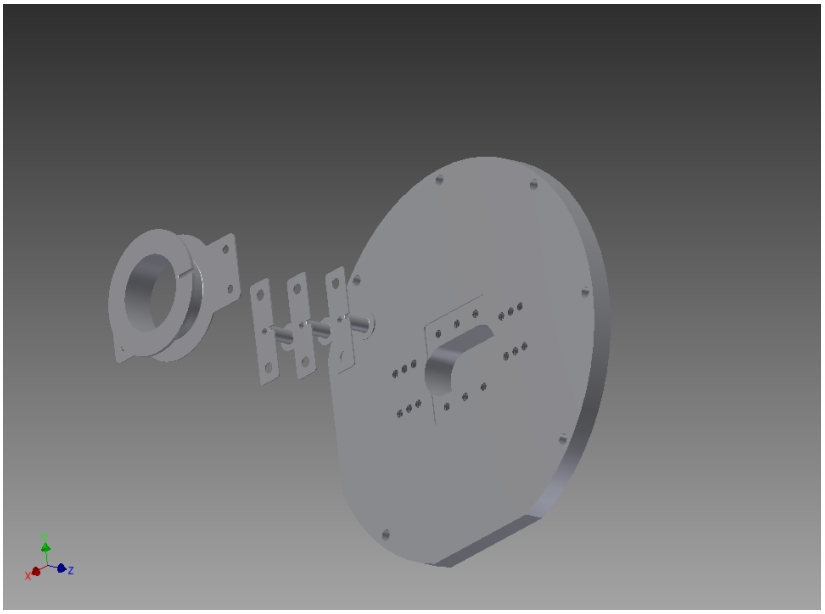

Figure 3.22: The illustrative CAD design of the mount with three small coil holders and a big coil holder.

The new small coil holders are fabricated. Together with the SC-T48B-M-0.025mm superconducting wire, they are sent to the company to get them winded with specific number of layers and number of turns.
The big coil holder was winded by 70 layers and 100 turns per layer (for a total N=7000 turns, around 330 m wire) for the 8-port microchip. It is winded by 20 layers and 100 turns per layer (for a total N=2000 turns, around 95m wire) for the 16-port microchip for economic reason. The magnetic field created by the big coil is reduced and can be compensated by increasing the current through

the coil. The small coil holders of 8-port microchip were winded by 30 layers and 120 turns per layer (for a total N=3600 turns, around 60m wire). As can be seen in the Fig 3.22 in order to mount three small coils in the backside groove of the mount, the size of the new smaller coil holders is reduced and a maximal winding of 20 layers (120 turns per layer) results in N=2400.
Since the size of the coil holders has been changed, the inductance and the magnetic field of the smaller coils are to be calculated to get a rough estimate of the magnetic field.
The ideal inductance of the solenoids is calculated by

$$L = \frac{\mu_0 \mu_r \pi r^2 N^2}{l}, \tag{3.6}$$

where the permeability of the vacuum $\mu_0 = 4\pi 10^{-7}$, the relative permeability μ_r=1 (in our case the coil is in the vacuum chamber), r is the effective radius of the solenoid, N is the total number of turns and l is the length of the solenoid. The effective radius r includes half the thickness of the winding coils.
In reality, the equation (3.5) requires modification if accurate inductance of the coils is needed. The field non-uniformity correction term is added to the previous equation.
The corrected inductance of the solenoids is now given by the Wheelers formula:

$$L = \frac{\mu_0 \mu_r \pi r^2 N^2}{l} K_L, \tag{3.7}$$

where $K_L = 1/\left(1 + 0.45D/l\right)$ is called Nagaokas coefficient and can be significantly different from 1 when the diameter D of the coil is comparable to the length of the coil l.
Through calculation, the inductances of the big coil of 8-port microchip and 16-port microchip are 1.012 H and 0.067 H respectively. The inductances of the small coil of 8-port microchip and 16-port microchip are 0.056 H and 0.009 H respectively. The inductance of the big coil and the one of small coils are reduced around 15 times and 6 times respectively.
The qubit transition frequency is controlled by the magnetic flux enclosed by the SQUID loop

$$\omega \propto E_J^{max} |\cos(\pi \frac{\phi}{\phi_0})|. \tag{3.8}$$

Assume that the area S enclosed by the SQUID loop is 2 microns square, and in order to induce a single quantum flux h/(2e), the magnetic field needed is around 0.75mT according to the formula below.

$$\Phi = B \cdot S = \Phi_0 = \frac{h}{2e}. \tag{3.9}$$

Now let's see with 1 mA current flowing in the coils, what are the B fields created by the coils at the locations of the qubits on the 16-port microchip.
The calculation is based on the ref [32] which is applicable for solenoids with single layer only, but we will anyway use this formula to get an intuitive view.
The flux focusing factor due to the superconducting ground planes is taken as

20 and the magnetic field losses during passing through the mount (copper), the PCB and the microchip (sapphire) are neglected.
The coordinations of the four qubits q1, q2, q3 and q4 in the Fig 3.11 are (-2.2,-2.1), (-2.2,1.9), (2.2,1.9) and (2.2,-2.1) respectively (in units of mm). The coordinations of the center of the three coils in the 8-port version b1, b3 and b4 (big coil) are (-3.7,1.53), (3.7,-1.53) and (0,0) respectively (in units of mm). The coordinations of the center of the four coils in the 16-port version c1, c2, c3 and c4 (big coil) are (-3.7,1.53), (0,0), (3.7,-1.53) and (0,0) respectively (in units of mm).

Table of magnetic fields (in units of mT) in the spots of q1, q2, q3 and q4 created by different coils with 1 mA current

	q1	q2	q3	q4
b1	8.2	0.2	2.6	3.6
c1	3.2	0.6	0.7	0.3
c2	7.9	9.3	9.3	7.9
b3	2.6	3.4	10.8	0.4
c3	0.7	0.4	3.8	0.3
b4	8.2	7.3	7.3	8.2
c4	3.9	3.5	3.5	3.9

As can be seen from the table above, the magnetic fields created by the coils c1, c2, c3 and c4 of 16-port microchip are reduced compared to the ones created by the coils b1, b3 and b4 of 8-port microchip. This decrease can be compensated by increasing the current through the coils. However, in our first several measurements, we still use the coils b1, b2 and b3 since simultaneously control all the four qubits are not required. The picture shown the mount with two small coils and a big coil is given in Fig 3.23.

On the microchip, a single qubit transition frequency is controlled by the

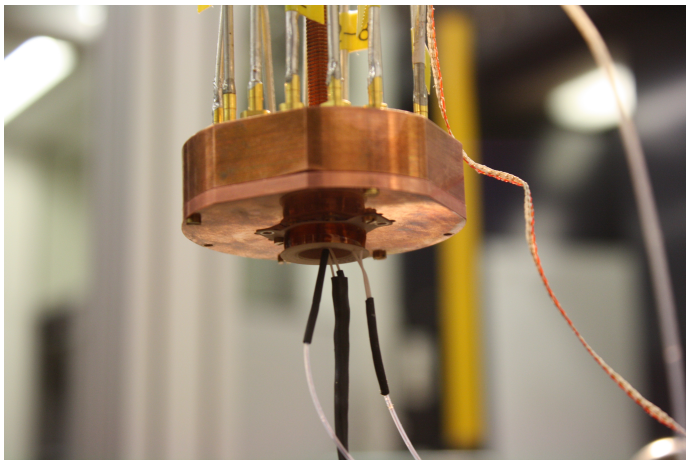

Figure 3.23: The two small coils and the big coil are fixed on the back side of the mount.

magnetic field created by all the coils in the way that the big coil provides the

overall magnetic field while the small coils only strongly tune the qubit near to their center lines [33].
The unwanted 1/f noise and low frequency current noise due to DC current which could affect the phase coherence of the qubits can be efficiently filtered out by a RC filter at room temperature [33].
The ultra-low noise isolated voltage source used here is provided by a Standard Research System SIM928 with short-circuit protected output. The ultra-clean (the noise is 10 μVrms with 1 kHz bandwidth) DC voltage can be set between $\pm$20V with millivolt resolution ($\pm$40 V floating voltage). The source can be set between $\pm$10mA and a maximum current of 15mA.

3.4 Dip stick and VNA

For the characterizations and measurements conducted in room temperatures, liquid nitrogen temperature (77 K) and liquid helium temperature (4.2 K), the dip stick and the Vector Network Analyzor (VNA) can be used to conduct the fast experiments. For the microchip with only 8 ports, a dip stick with only 8 connectors was designed and fabricated. For our new 16 port sample, an adapter with 16 connections (see Fig 3.24) is designed and fabricated.

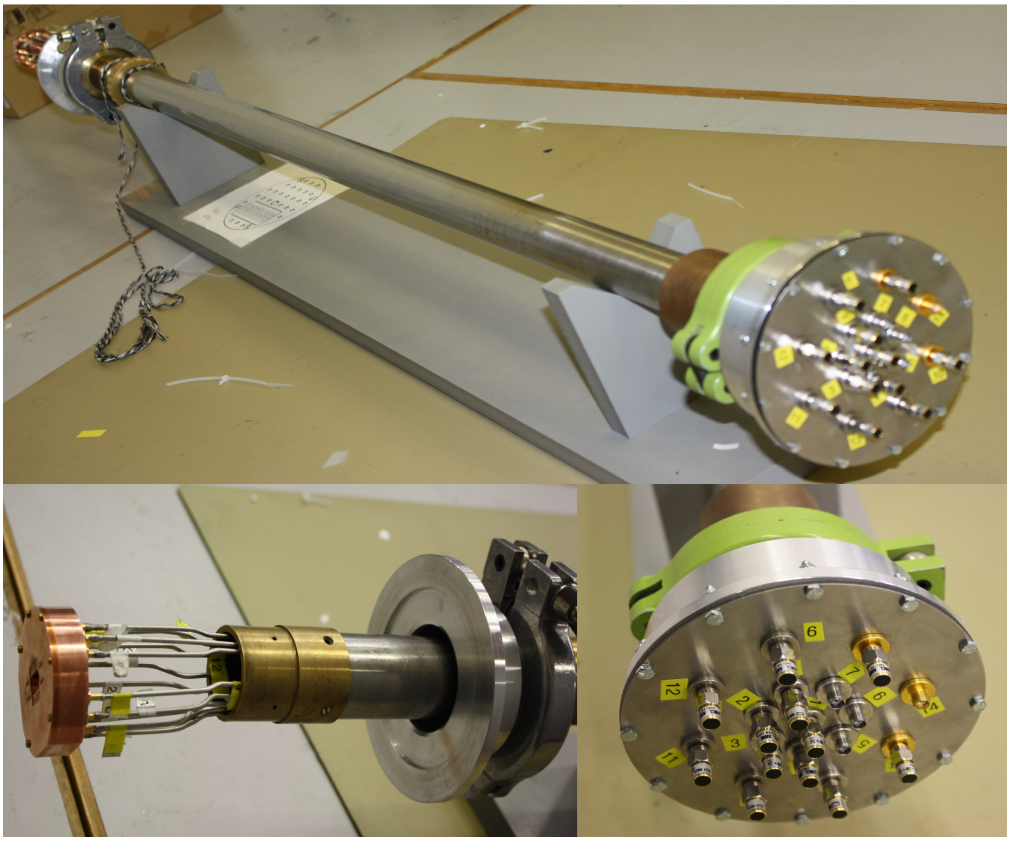

Figure 3.24: The upper picture shows the full view of the dip stick. The lower pictures give a near view of its two ends. The left one is the sample mounted to the dip stick. The right one shows the 16 ports for connections. Some ports on the dip stick are terminated by 50 Ω terminations to suppress reflection signals if they are not connected to the Network Analyzer.

Chapter 4

Characterization

With the measurement setup described in the previous chapter, it is important to first characterize the newly made cables, the PCB cover and the microchips with only microwave resonators.

4.1 Cables characterization

Since the new microchips have 16 ports, new cables need to be fabricated. The SMA and SMP connectors are soldered on the ends of the cables. When the dip stick is dipped inside the dewar of helium, the heat transfered from outside speeds up the evaporation of the liquid helium which should be tried to avoid. Thus the cables inside of the dip stick are of the type SS-Cu (stainless steel outer conductor and copper inner conductor). The outside conductor of the cables is made of stainless steel since steel has poor heat conductivity compared to the copper and the heat is mainly transferred by the outside conductor of the cable. The inner conductor of the cables is made of copper to decrease the signal loss.

The cable is then connected to the VNA to measure the transmission and reflection through the cable. The diagram 4.1 shows the data of the SS-Cu cable at room temperature. Curves with different color indicate the reflection and transmission spectra: the blue and green curves represent the reflection signal power from each end of the cable when an input signal frequency swept from 300kHz to 20 GHz is sent to the cable; the red and yellow curves represent the transmission signal power measured in each end (the yellow transmission curve is shifted down 10 dB for better visibility).
As long as the reflection spectra are below -10dB, the cable is of good quality and can be used in our experiments.

4.2 PCB cover characterization

For a high conductive material, the penetration depth of electric field is fairly small, which means that the electromagnetic (EM) field is mostly reflected. Since the microwave photons can be reflected by the metal like the visible

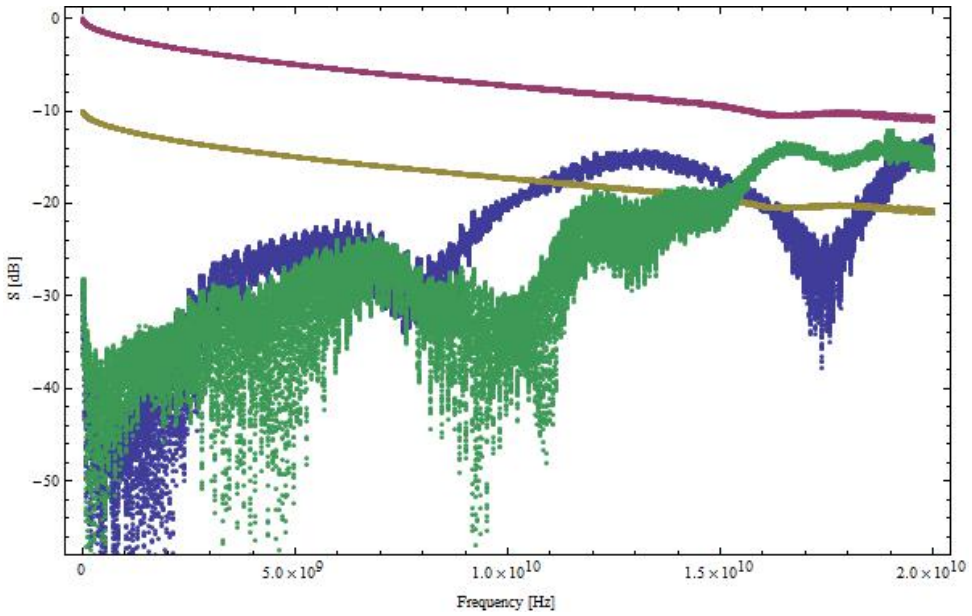

Figure 4.1: The transmission (yellow and red) and reflection (blue and green) spectra of the SS-Cu cable at room temperature. The yellow transmission curve is -10 dB shifted.

range photons reflected by the mirror, a standing electromagnetic oscillation of specific frequency could be formed in a cavity made of metal. As can be seen from Fig 3.19, the 3D cylindrical cavity formed between the PCB and the lid can also couple to the qubits in our experiments. To avoid this unwanted coupling, a PCB cover made of conducting material is placed inside of the 3D cavity to shift the cavity resonance frequency out of 0-20 GHz. However, the small 3D rectangular cavity directly above the microchip together with its extending channels still causes some unwanted resonances below 20 GHz as will be shown in the sections below.

4.2.1 Resonance frequencies of the cavity modes

From Maxwell equations and the boundary conditions (the tangential component of the electric field vanishes on the interface between cavity and metal), the resonance frequencies of different modes for cylindrical and rectangular waveguides can be deduced from ref [34].
Three modes are considered here: Transverse electromagnetic (TEM) wave modes with $E_z = H_z = 0$ (z is the EM field propagation direction), Transverse electric (TE) wave modes with $E_z = 0, H_z \neq 0$, Transverse magnetic (TM) wave modes with $E_z \neq 0, H_z = 0$. TEM wave modes can exist only when two or more conductors are present which indicates that the closed cylindrical and rectangular cavity cannot support TEM waves.
The rectangular cavity is the terminated-at-two-ends rectangular waveguide with cross section size a x b and length c. It has the same resonance frequen-

cies for the TE and TM modes:

$$f_{mnl} = \frac{1}{2\pi\sqrt{\mu_r\epsilon_r}}\sqrt{(\frac{m\pi}{a})^2 + (\frac{n\pi}{b})^2 + (\frac{l\pi}{c})^2} = \frac{1}{2\sqrt{\mu_r\epsilon_r}}\sqrt{(\frac{m}{a})^2 + (\frac{n}{b})^2 + (\frac{l}{c})^2} \tag{4.1}$$

where l m and n are integers and ϵ_r and μ_r are the relative dielectric and magnetic constants, respectively.
The cylindrical cavity can also be considered as the terminated-at-two-ends cylindrical waveguide with radius a and length d. The resonance frequencies for the TE and TM modes are respectively:

$$f^{TE}_{mnl} = \frac{c}{2\pi\sqrt{\mu_r\epsilon_r}}\sqrt{(\frac{P'_{nm}}{a})^2 + (\frac{l\pi}{d})^2} \tag{4.2}$$

$$f^{TM}_{mnl} = \frac{c}{2\pi\sqrt{\mu_r\epsilon_r}}\sqrt{(\frac{P_{nm}}{a})^2 + (\frac{l\pi}{d})^2} \tag{4.3}$$

where P'_{nm} and P_{nm} are the roots of the Bessel function of first kind and the roots of the derivative of the Bessel function of first kind. l and n are integers, and m are non-zero integers.
The values of P'_{nm} and P_{nm} are partially given in the table below

Table of P'_{nm} and P_{nm}

n	P'_{n1} / P_{n1}	P'_{n2} / P_{n2}	P'_{n3} / P_{n3}
0	3.832/2.405	7.016/5.520	10.174/8.654
1	1.841/3.832	5.331/7.016	8.536/10.174
2	3.054/5.135	6.706/8.417	9.970/11.620

The deductions of the cavity resonator frequency will be used for the understanding of the transmission spectra presented in the following sections.

4.2.2 Characterization of the microchip with Cu resonators

In the Fig 4.2, the PCB cover on the left side is made of copper (copper has good electrical and heat conductivity at low temperatures). The PCB on the right side consists of 6 Copper resonators (the most left one and the most right one do not have capacitors, thus not resonators) and 16 ports (each resonator is connected to its two ports by an input and an output capacitors). Only 4 ports are used where 4 SMP connectors labeled port 1,2,3 and 4 are soldered on. The resonators R1 between ports 1,2 and R2 between ports 3,4 are of the same size (12.71 mm).
The sample is mounted on the dip stick with which the sample can be dipped in liquid nitrogen and liquid helium dewars for measurements. The frequency dependent transmissions are measured with a Network Analyzer. The input power used is -5 dBm.

The diagram 4.3 shows the spectrum of the Cu resonators inserted in the

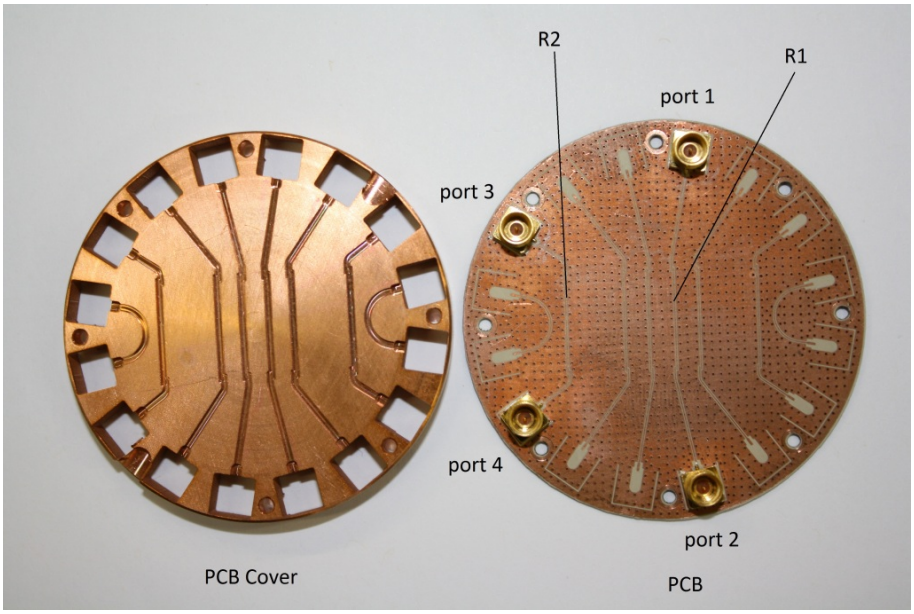

Figure 4.2: PCB with copper resonators and its PCB cover

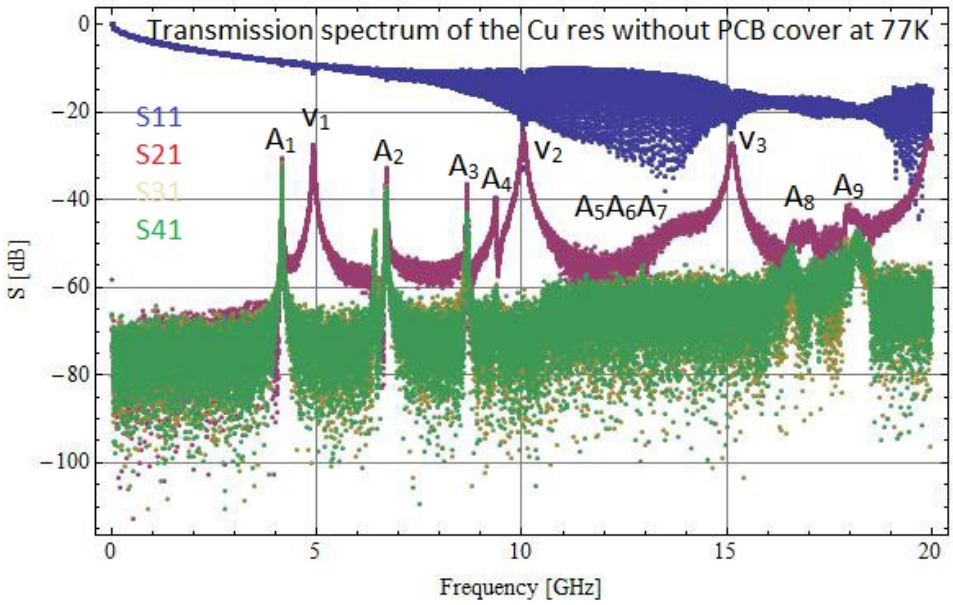

Figure 4.3: The spectrum of the Cu resonators inserted in the liquid nitrogen without PCB cover

liquid nitrogen without PCB cover.
As can be seen from Fig 4.3, the reflection S11 is frequency dependent. There are several tiny drops corresponding to the transmission signal power peaks ν_1, ν_2 and ν_3 in curve S21 (the resonance frequencies of the copper resonator R1). The resonance peaks in S21 could only induce small drops in S11 for the reason that the reflection signal power is way larger than the transmission

signal power.

Table of resonance frequencies of Cu resonator R1 at 77 K

resonance	frequency[GHz]	Power transmission max[dB]	Q
ν_1	4.91	-28	117
ν_2	10.04	-24	108
ν_3	15.14	-27	117

The experimental frequency and quality factor are obtained by fitting a Lorentzian line shape according to

$$P(\nu) = P_0 \frac{\delta\nu^2}{(\nu - \nu_0)^2 + \delta\nu^2} \tag{4.4}$$

$$Q = \frac{\nu_0}{\delta\nu} \tag{4.5}$$

where $\delta\nu$ is the full width half maximum of the resonance, P_0 is the maximal transmission amplitude and ν_0 is the resonance frequency.
The peaks A1, A2,...,A9 occur in S21, S31 and S41 can be interpreted by the resonances of the cylindrical cavity between the PCB and the lid (cylindrical cavity modes) and can be theoretically calculated and explained by the Eq. (4.2) and Eq. (4.3). The cavity resonance peaks displayed in S21, S31 and S41 could also be found in S11 (nearly invisible due to the strong reflection and relatively weak resonances).
The relative permittivity of liquid nitrogen is 1.5 [35]. The relative permeability is taken to be 1. The height of the cylindrical cavity is 4.8 mm. The effective radius of the cylinder is 15 mm (real radius 24.5 mm) since it is not an ideal one (the SMP connectors, cables, holes on the lid, etc. are presented inside of the cylindrical cavity).
The TE mode with n = 0, m = 1 have the same theoretically predicted value as the TM mode with n = 1, m = 1 does. It is the same case for A9. The value of A10 is out of the range in the Fig 4.3. If we take l = 1 and n = m = 1 in TE mode such that the contribution from the $(P'_{nm}/a)^2$ in the Eq. (4.2) is the smallest, the resonance frequency A11 is still as large as 25.96 GHz which is out of our range. Thus only the nine lowest order resonance frequencies are shown in the Fig 4.3 and in the table below.
The theoretically predicted resonance peaks A5, A6 and A7 corresponding to 13.35 GHz, 13.86 GHz and 14.35 GHz respectively are not visible in the plot for the reason that their resonances are too close (see the table below) and weak.

Table of peaks of Cu resonator due to cylindrical cavity at 77 K

Peaks	n	m	l	P'_{nm} or P_{nm}	mode	theoretical frequency [GHz]	experimental frequency [GHz]	Max dB	Q
A1	1	1	0	1.841	TE	4.78	4.14	-30	634
A2	0	1	0	2.405	TM	6.25	6.69	-33	590
A3	2	1	0	3.054	TE	7.94	8.67	-36	724
A4	0	1	0	3.832	TE	9.96	9.36	-40	274
A4	1	1	0	3.832	TM	9.96	9.36	-40	274
A5	2	1	0	5.135	TM	13.35	—	—	—
A6	1	2	0	5.331	TE	13.86	—	—	—
A7	0	2	0	5.520	TM	14.35	—	—	—
A8	2	2	0	6.706	TE	17.43	16.92	-47	26
A9	1	2	0	7.016	TM	18.23	18.08	-43	58
A9	0	2	0	7.016	TE	18.23	18.08	-43	58
A10	2	2	0	8.417	TM	21.88	—	—	—
A11	1	1	1	8.536	TE	25.96	—	—	—

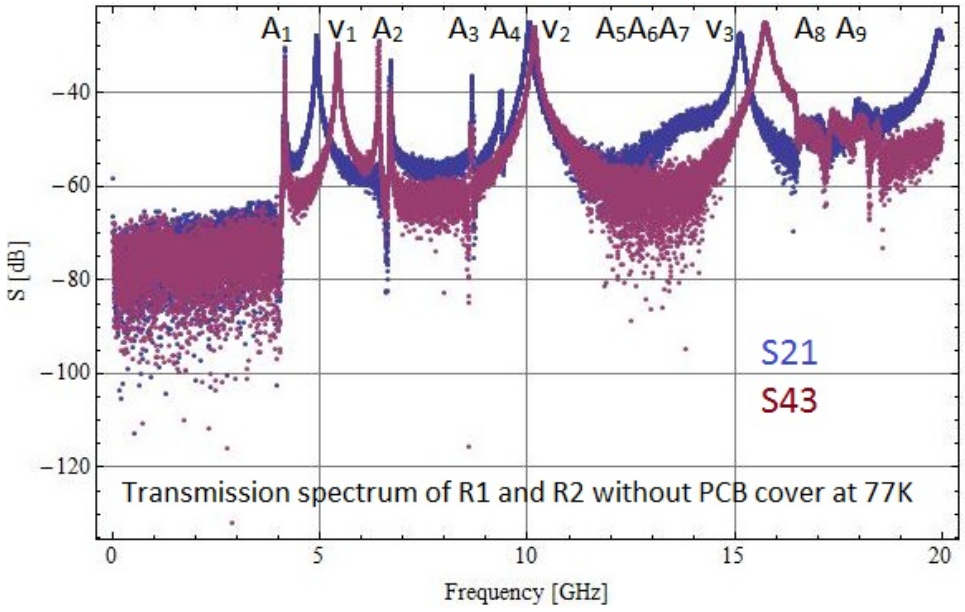

Figure 4.4: The spectra of the Cu resonators inserted in liquid nitrogen without PCB cover

The Fig 4.4 shows the spectra of resonators R1 and R2 without cover dipped in liquid nitrogen. The two resonators are of the same size (same length 12.71 mm) but of different resonance frequency for the first and third resonance peaks. This is because the resonance frequency depends not only on the length of the resonator but also on its dielectric environment (the two resonators are located at different places on the PCB).
This figure also shows that the peaks A1, A2,...A9 corresponding to the cylindrical cavity resonances exist not only in S21 but also in S43 (except for A2 and A4). It confirms that the peaks A1, A2,...A9 are not the resonances of

a specific resonator but the ones of the whole cylindrical cavity. However, since the cylindrical cavity is not homogeneous inside (inhomogeneous dielectric environment), the resonances are slightly dependent on the position of the resonator. This explains the anomalies of A2 and A4.

It can be easily seen from the Fig 4.5 that the resonance peaks A1, A2,...,A9

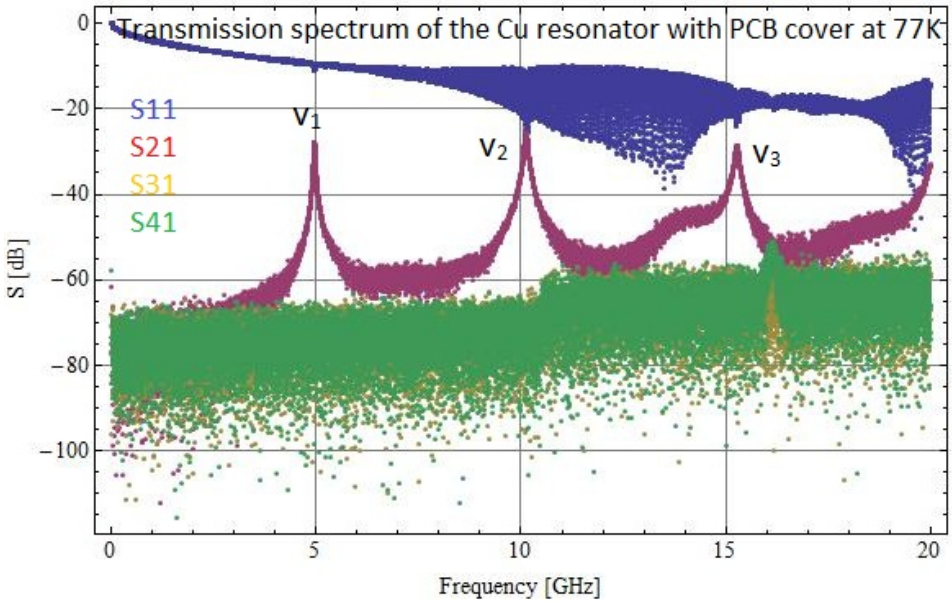

Figure 4.5: The transmission spectrum of the Cu resonator in liquid nitrogen with PCB cover

due to the cylindrical cavity are eliminated by the presence of the PCB cover except for an anomaly in S41 at around 16 GHz.

The Fig 4.6 shows the spectrum of Cu resonator R2 dipped in liquid helium with and without PCB cover, respectively. The one with PCB cover is shifted down by 40 dB for better visibility.

Here the effective radius of the cylinder is 17 mm. The relative permittivity of liquid helium (slightly depends on the frequency and the temperature) is taken to be 1.05 [35]. The relative permeability is taken to be 1. The first three peaks due to the presence of the cylindrical cavity are of good visibility while the peaks B4 B5 B6 and B7 are nearly invisible.

Table of peaks of Cu resonator R2 due to cylindrical cavity at 4.2K

Peaks	n	m	l	P'_{nm} or P_{nm}	mode	theoretical frequency [GHz]	experimental frequency [GHz]
B1	1	1	0	1.841	TE	5.05	4.78
B2	0	1	0	2.405	TM	6.59	7.22
B3	2	1	0	3.054	TE	8.37	7.62
B4	0	1	0	3.832	TE	10.50	9.83
B4	1	1	0	3.832	TM	10.50	9.83
B5	2	1	0	5.135	TM	14.07	13.50
B6	1	2	0	5.331	TE	14.61	14.9
B7	0	2	0	5.520	TM	15.13	16.3

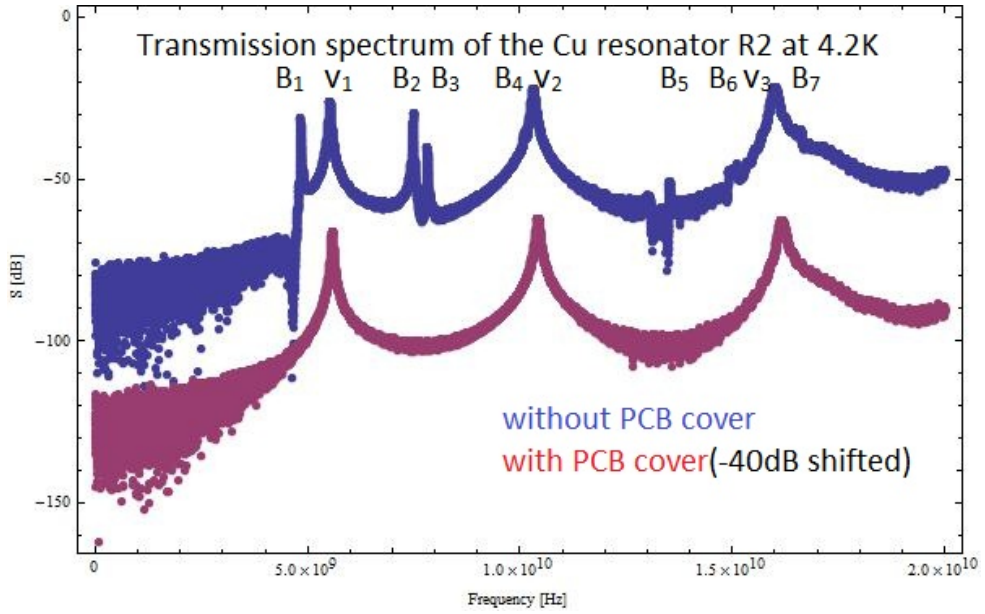

Figure 4.6: The transmission spectrum of the Cu resonator inserted in liquid helium with/without PCB cover

The Fig 4.7 shows the spectra of the Cu resonator R1 with PCB cover dipped in the air, liquid nitrogen and liquid helium respectively. The resonance frequency shifts at different temperature because it depends on the temperature dependent kinetic inductance and the dielectric environment changes (from air, liquid nitrogen to liquid helium)[31].

4.2.3 Characterization of the microchip with Nb resonators

The PCB cover shown in Fig 4.8 is made of copper. In the middle of the PCB cover a rectangular cavity of the size 7.8 mm x 8.2 mm x 0.5 mm is presented. In the middle of the 16-port PCB, a 7 mm x 6.6 mm microchip M20W1 (see Fig 4.9) is glued on. The microchip M20W1 consists of 4 parallel

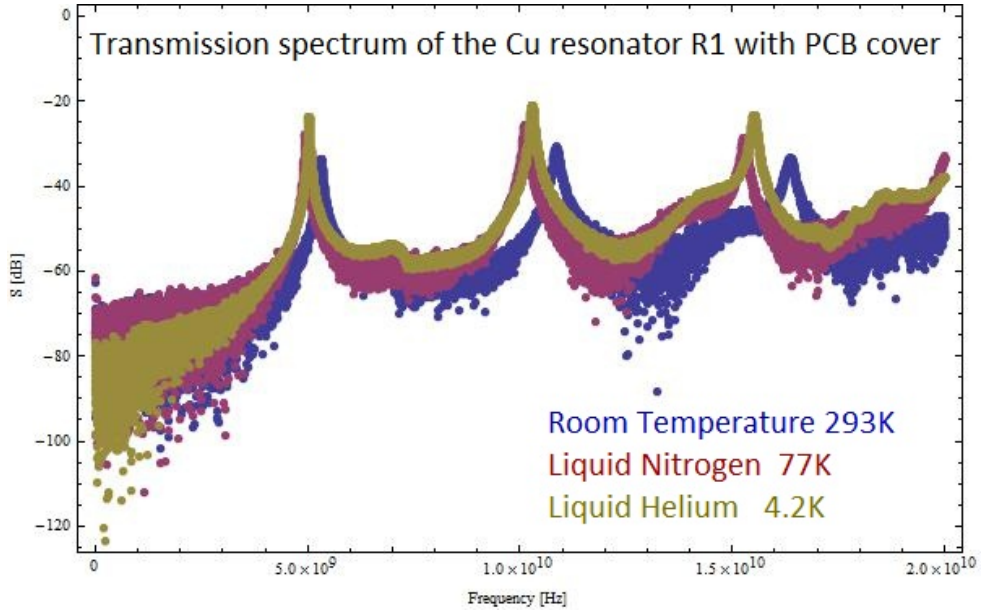

Figure 4.7: The transmission spectra of the Cu resonator R1 inserted in air, liquid nitrogen and liquid helium with PCB cover

niobium resonators with different frequencies on the sapphire substrate. Each Nb resonator is connected to its two ports by an input and an output capacitors. Only 8 ports are used and they are connected by 8 SMP connectors labeled as port 1, 2,...8. The other ports are bonded to the ground planes on the PCB. The resonators R1 and R3 are of the same resonance frequency (7.5 GHz). The resonators R2 and R4 are of the same resonance (6.5 GHz). The resonators R1 and R2 are of the same gap width s (5.5 μm) (see Fig 3.12). The resonators R3 and R4 are of the same gap width s (4.5 μm). All of them have the same resonator width a = 10 μm (see Fig 3.12). The upper left corner of the microchip is over etched and the center conductor of resonator R4 is partly connected to the ground plane of the microchip during the optical lithography fabrication.

The Fig 4.10 shows the transmission spectrum of Nb resonator R1 dipped in liquid helium with PCB cover and with bonds over resonators (ports 1, 2, 3 and 4 are connected to the Network Analyzer). The resonance peaks C1, C2,...,C5 (higher modes are not considered here) are due to the rectangular cavities indicated in the Fig 4.8. The rectangular cavity 1 is of the size 7.8 mm x 8.2 mm x 0.5 mm. The rectangular cavity 2 is of the size 14.11 mm x 0.9 mm x 0.5 mm and the effective size is taken to be 18mm x 0.9mm x 0.5mm. The rectangular cavity 3 is of the size 13.47 mm x 0.9 mm x 0.5 mm and the effective size is taken to be 10.6 mm x 0.9 mm x 0.5 mm. The cavities 2 and 3 are closed by the SMP connectors at one end and by the bonds connecting the microchip to the PCB at another end. All of the three cavities are not ideal, and the effective sizes for the cavities 2 and 3 are especially necessary. The extra resonance peaks in S31 are probably due to the fabrication failure (over

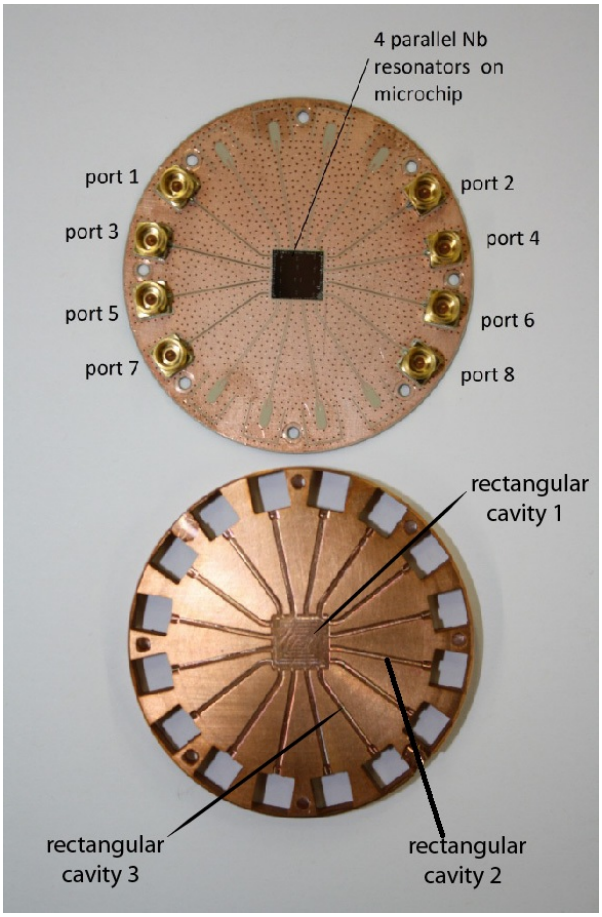

Figure 4.8: A microchip M20W1 with 4 parallel NB resonators on (see figure 4.9) is glued on a PCB with 8 SMP connectors labeled port 1, $2 \cdots 8$. The PCB cover is shown in below. Rectangular cavities 1, 2 and 3 are indicated.

etching and R4 connecting to the ground plane).

Table of rectangular cavity modes of the PCB cover in Fig 4.8

Peaks	n	m	l	a [mm]	b [mm]	c [mm]	theoretical frequency [GHz]	experimental frequency [GHz]	max dB	Q
C1	0	0	1	0.5	0.9	18	8.13	8.73	-55	294
C2	0	0	1	0.5	0.9	10.6	13.81	13.48	-48	218
C3	0	0	2	0.5	0.9	18	16.27	15.63	-48	73
C4	0	1	0	0.5	8.2	7.8	17.85	17.76	-52	123
C5	0	0	1	0.5	8.2	7.8	18.77	18.46	-48	155

The Fig 4.11 shows the transmission spectra of Nb resonator R3 with and without bonds over the resonators with PCB cover dipped in liquid helium (ports 5, 6, 7 and 8 are connected to the Network Analyzer). It can be easily seen that with bonds the unwanted resonance peaks D1, D2, D3 and D4 are

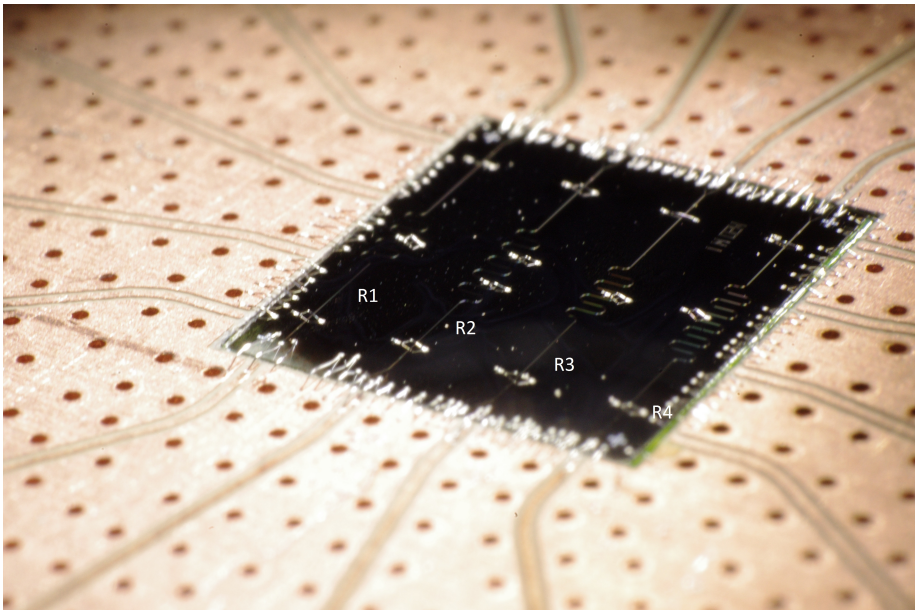

Figure 4.9: The microchip M20W1 with 4 parallel Nb resonators.

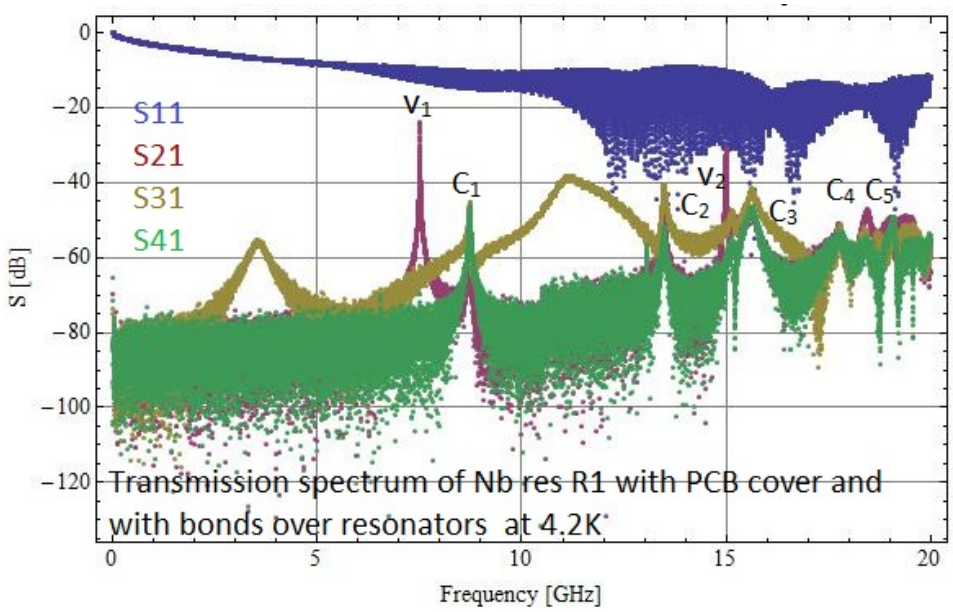

Figure 4.10: The transmission spectrum of the Nb resonator R1 with PCB cover and with bonds over resonators in liquid helium.

eliminated. The resonance peaks C1, C2,...C5 due to the rectangular cavities are still present but slightly changed because the dielectric environment of the cavities has been changed due to the presence of the bonds over resonators.

Since the resistance of Nb at room temperatures is so high that the transmission of the signal is fairly low, the resonance peaks due to the Nb resonators

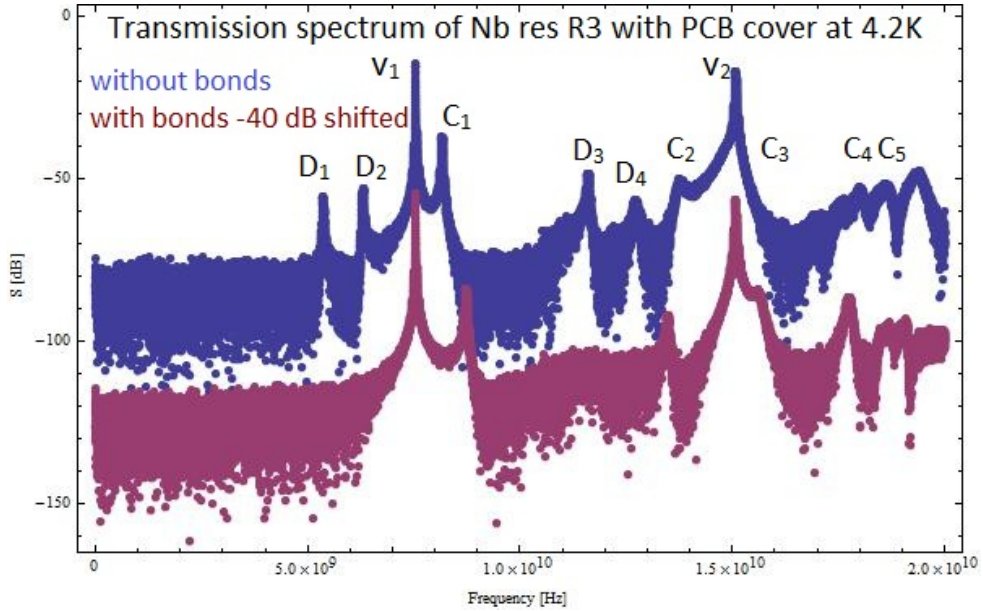

Figure 4.11: The transmission spectrum of the resonator R3 with PCB cover with and without bonds over resonators at 4.2 K.

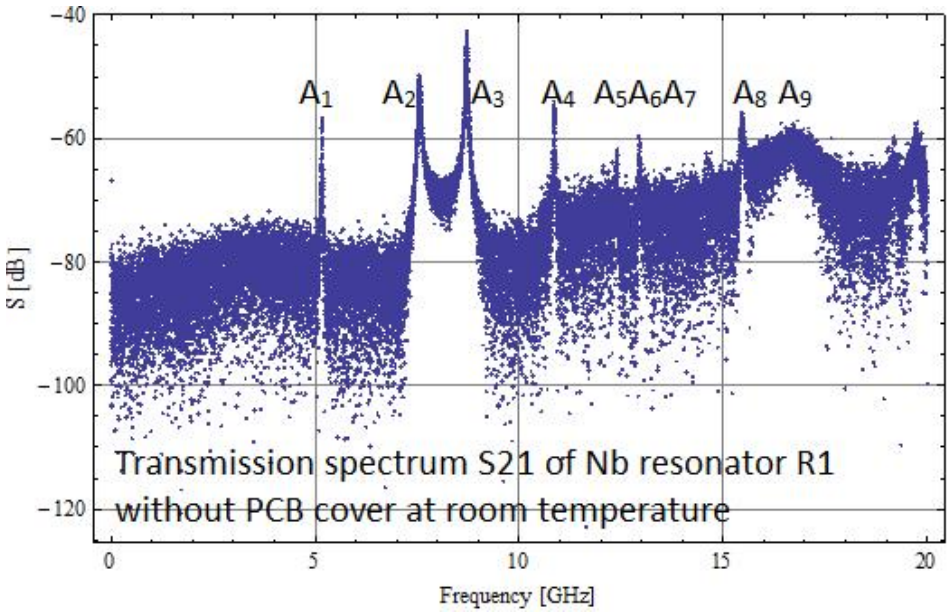

Figure 4.12: The transmission spectrum of the microchip M20W1 without PCB cover at room temperatures.

are suppressed while the resonance peaks of the cylindrical cavity are clearly visible. These values have been theoretically predicted in the table of peaks of Cu resonator due to cylindrical cavity at 77 K except for a slight change due to the change of dielectric environment from liquid nitrogen to air and the change of microchip. They can be used to check the resonance frequencies of

the cylindrical cavity. This can not be done with Cu resonator due to its high signal transmission ability even at room temperatures (see Fig 4.7).
As can be seen from the Fig 4.12, the invisible peaks A5, A6 and A7 in the Fig 4.3 are presented here due to the suppression of the resonator resonances.
With the PCB cover over the microchip M20W1, the transmission spectrum

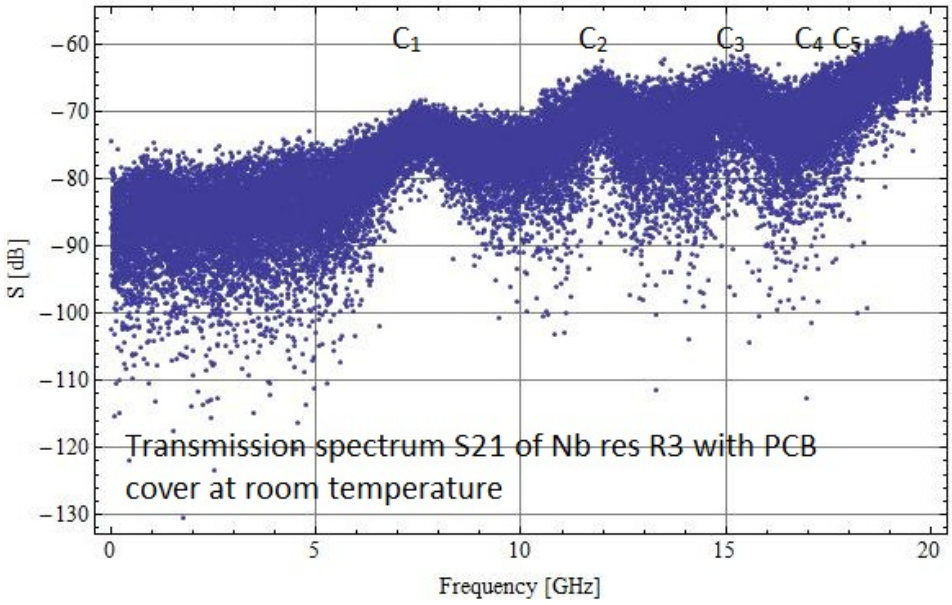

Figure 4.13: The transmission spectrum of the microchip M20W1 with PCB cover at room temperatures.

from Fig 4.13 shows the rectangular cavity modes C1, C2,...C5.

4.3 Characterization of the microchip M20E2 with 7 ports connected at 20 mK

The characterization of the resonators on the microchip M20E2 (see Fig 4.14) is done with the Network Analyzer. The sample is mounted inside of the cryostat (see section 3.2) and cooled down to around 20 mK.
Since currently only two cold amplifiers are implemented inside of the cryostat, the transmitted signals from two of the three resonators can be amplified and read out. Port 2 is connected to 109D Caltech amplifier (bandwidth 1-12 GHz) and Port 3 is connected to LNF amplifier (bandwidth 4-8 GHz). A room temperature amplifier AFS3 is also implemented outside of the cryostat to get better Signal-to-Noise Ratio (SNR). Thus signals transmitted from res1 and res2 can be detected. In this section all the ports labeled 1, 2,...8 are connected except for port 5 connecting the flux line of qb2.
The characterization of the cables inside of the cryostat and of the amplifiers are first investigated at room temperature before the characterization of the resonators on the microchip.

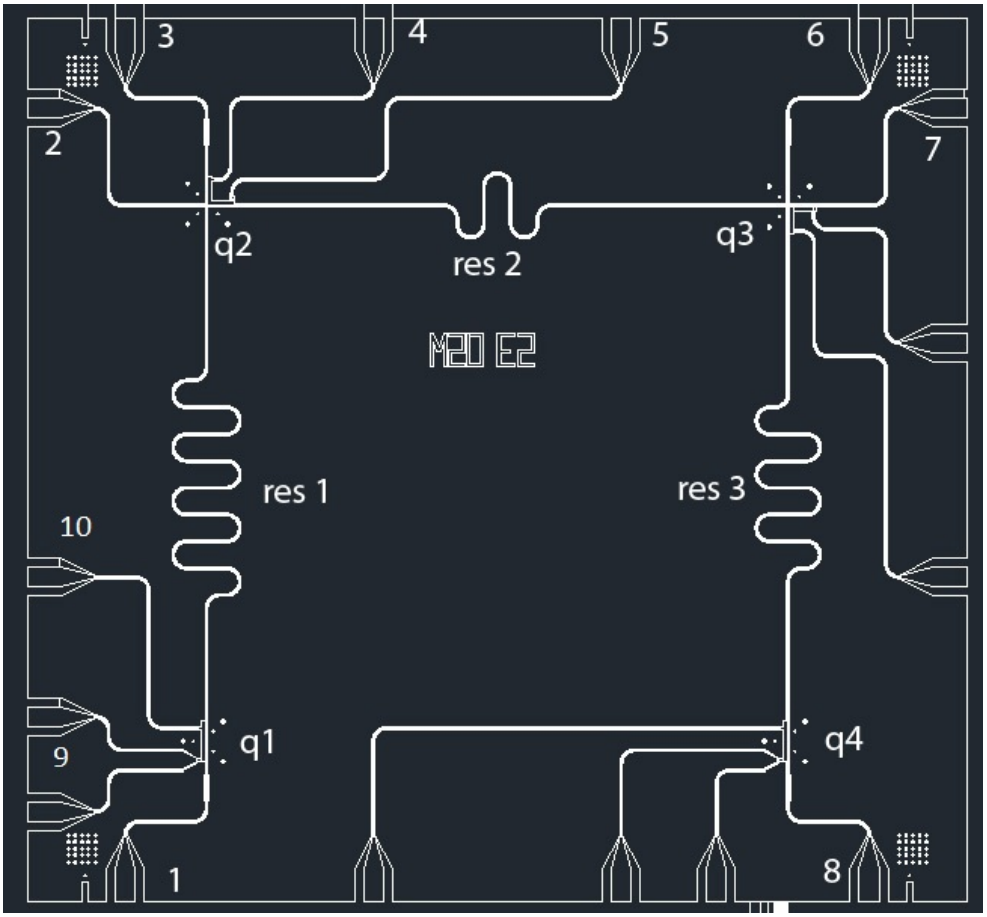

Figure 4.14: The illustration of the microchip M20E2. Three crossed resonators are indicated as res1, res2 and res3. The four qubits are also labeled as qb1, qb2, qb3 and qb4 (the transmons are not fabricated on this microchip). Two ports for each resonator and each transmon, 14 ports in total are presented here. Only ten ports are labeled from 1 to 10.

The cables connecting to ports 1, 4, 6, 7 and 8 are connected to the Network Analyzer first. There are no amplifiers on these cables. The cabling configuration inside of the cryostat connecting to port 4 is shown on the right of the Fig 4.15. The cables are thermalized at different stages. Its transmission spectrum at room temperature is shown on the left. A -50 dB attenuation can be easily seen at 300 KHz and as the frequency increases the transmission signal drops due to the signal losses in the cables. A sharp drop at around 5 GHz is observed. This is probably due to a bad connector.

For the room temperature amplifier AFS3, the bandwidth is 4-8 GHz and its gain is 30 dB within this range. The maximum output power is 15 dBm. To protect the amplifier from being destroyed by incorrect manipulation of the Network Analyzer, a -40 dB attenuator is employed on the output channel of the Network Analyzer since its maximum output power is 27 dBm. As can be seen from the Fig 4.16, the bandwidth of the room temperature amplifier is 3-11 GHz.

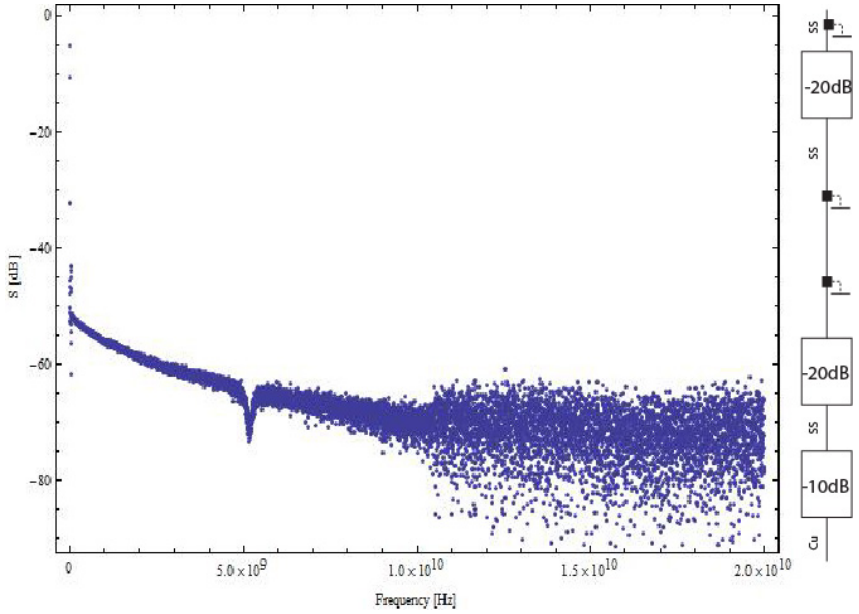

Figure 4.15: The transmission spectrum at room temperature of the cable connecting to port 4 without any amplifiers. The cabling configuration is shown on the right.

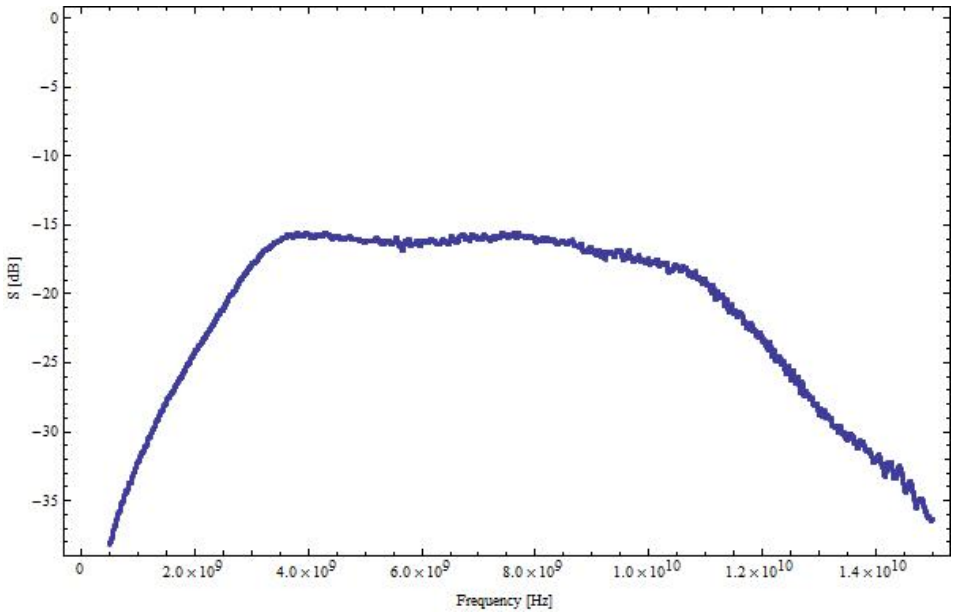

Figure 4.16: Room temperature amplifier AFS3-04000800-10-ULN-1048833 transmission spectrum.

The cables connecting to the output port 2 are loaded with a -10 dB attenuator, a Caltech amplifier and two circulators as shown on the right of the Fig 4.17. The transmission spectrum shows a good bandwidth of 5-11 GHz (due to the other components in the line on the right of the Fig 4.17) instead of 1-12 GHz.

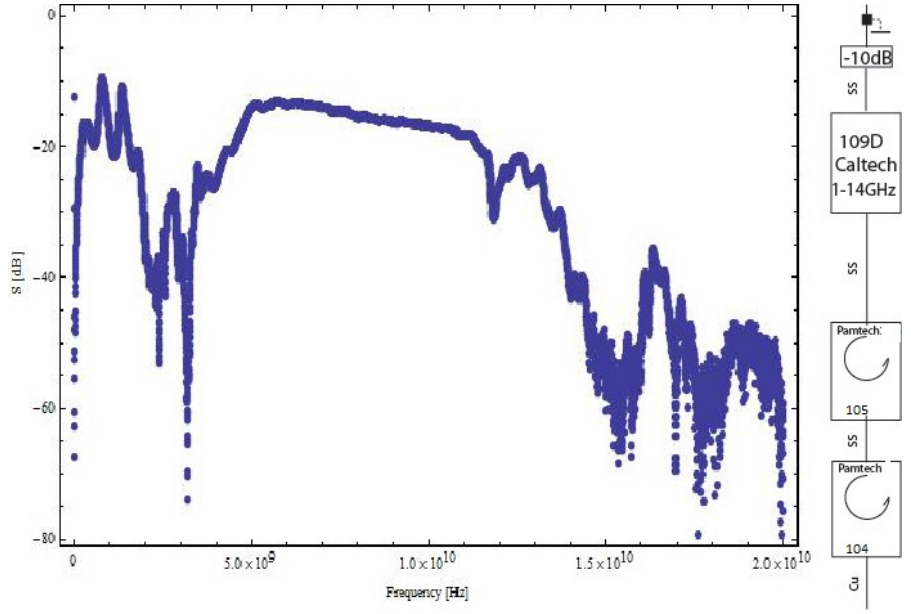

Figure 4.17: The transmission spectrum of 109D Caltech amplifier at room temperature. The cabling configuration is shown on the right.

As can be seen from Fig 4.18, the cables connecting to the output port 3 are

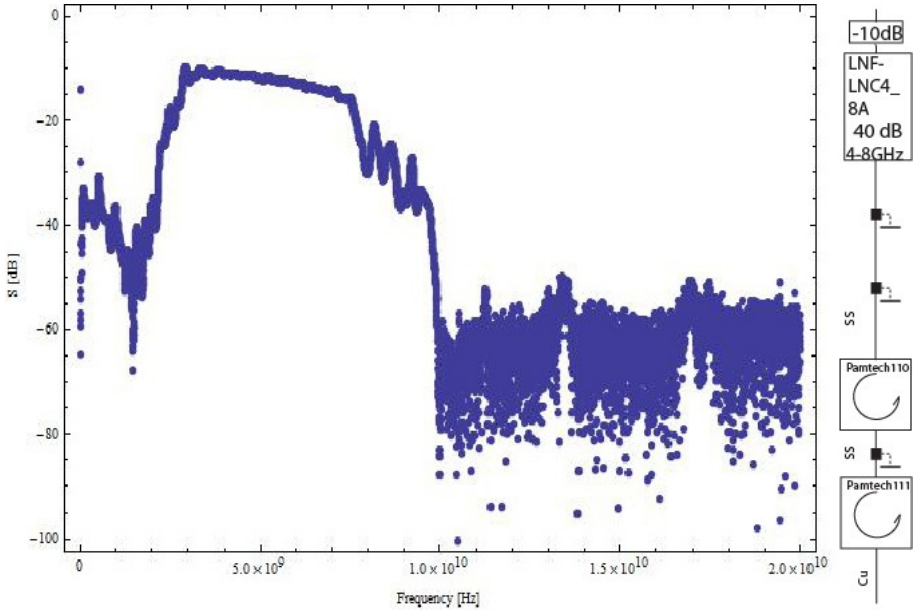

Figure 4.18: The transmission spectrum of LNF amplifier (bandwidth 4-8 GHz) at room temperature. The circuit is shown on the right.

loaded with a -10 dB attenuator, a LNF amplifier and two circulators. The transission spectrum shows a good bandwidth of 3-8 GHz.

With the characterization of the cables inside of the cryostat and of the am-

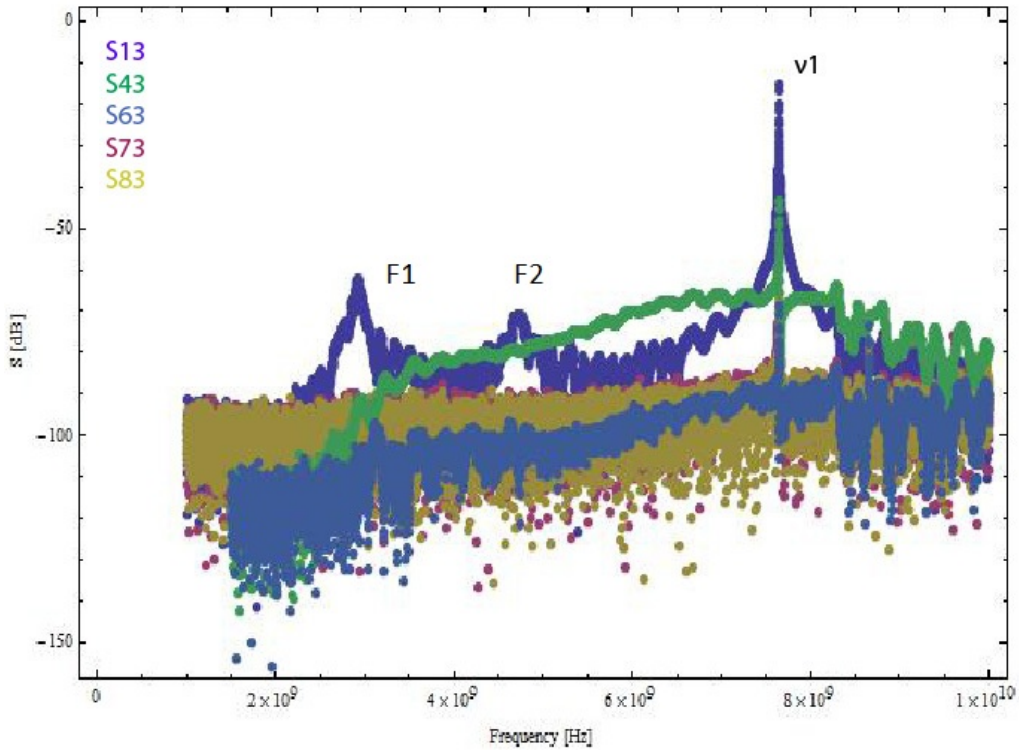

Figure 4.19: The transmission spectra with readout connected to port 3 and input ports 1, 4, 6, 7 and 8.

plifiers, the characterization of the resonators on the microchip M20E2 can now be conducted. The sample is mounted inside of the cryostat and cooled down to 20 mK. Signals are sent through ports 1, 4, 6, 7 and 8. The readout with amplifiers is connected to the ports 2 and 3 each time.
The Fig 4.19 shows with port 3 as readout the transmission spectra of signals from input ports 1, 4, 6, 7 and 8 respectively. The resonance peaks F1 (2.917 GHz, Q=51) and F2 (4.719 GHz, Q=40) in S13 are spurious modes not from the cavity modes since they appear only on S13 and their resonance frequencies are not close to any theoretically calculated values we have in previous sections (see Table of rectangular cavity modes of the PCB cover in Fig 4.8). The resonance peak ν1=7.65 GHz and Q=5037 in S13 is the largest since port 1 and port 3 are the two ends of the resonator res1. The signals from the ports 4, 6, 7 and 8 can also induce the resonance to port 3 with lower peaks at 7.65 GHz.

Similarly, the transmission spectra from input ports 4, 6, 7 and 8 and port 2 as readout are shown in Fig 4.20. The resonance peak ν2=9.61 GHz and Q=11094 in S72 is the largest since port 2 and port 7 are the two ends of the resonator res2. The signals from the ports 1, 4, 6 and 8 can also induce the resonance to port 2 with lower peaks at 9.61 GHz. Different from the Fig 4.19, the resonances of the resonators res1 and res3 can also be seen even though the output port is on resonator res2.

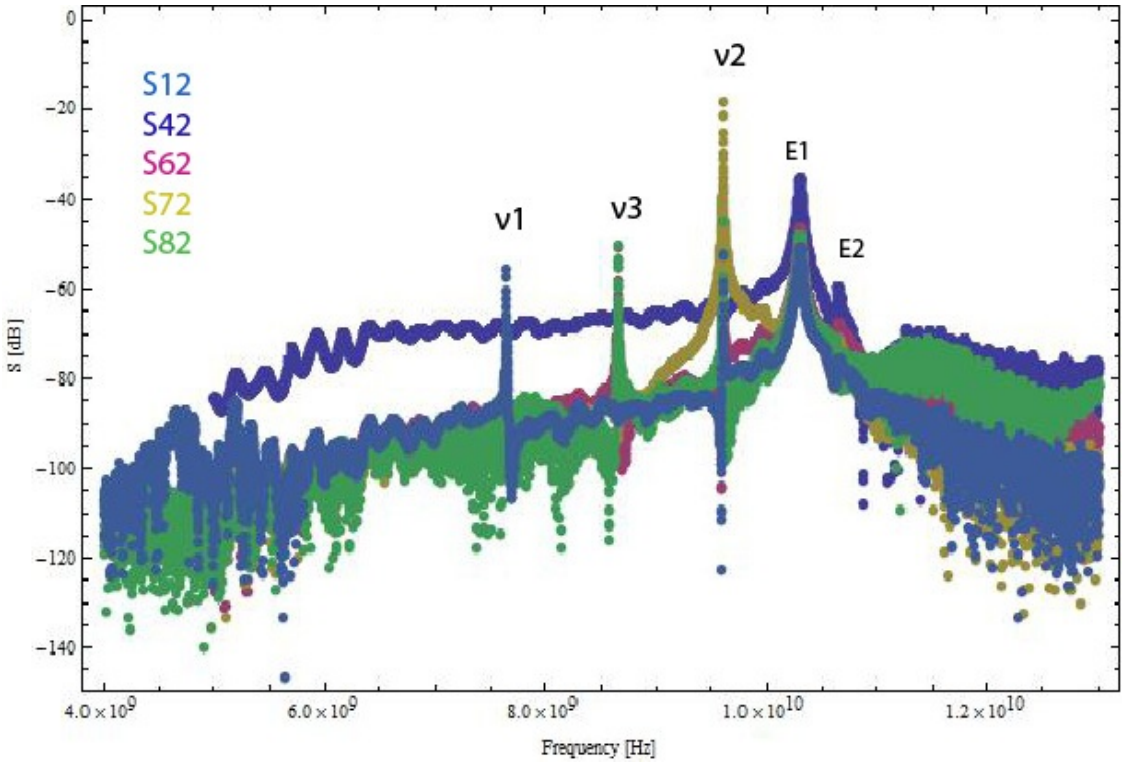

Figure 4.20: The transmission spectra with readout port 2 and input ports 1 4 6 7 and 8.

The resonance peaks E1 (10.30 GHz, Q=368) and E2 (10.65 GHz, Q=642) in S42 are cavity modes because they appear in almost every transmission spectrum with almost the same strength and Q. However, the peaks in S42 are a little bit higher than in the other spectrum. Since the flux line port 5 is not connected and bonded, the λ /4 resonance (because the flux line is grounded) of the flux line is suggested to be one of the possible reasons for the unwanted resonance peaks at 10.3 GHz and at 10.65 GHz which we will check again later with the 16-port dip stick (see next section). In addition, the resonances at 10.3 GHz of E1 and 10.65 GHz of E2 are not close to the values we get in the Table of rectangular cavity modes of the PCB cover. This is because the dielectric environment has changed from liquid helium to vacuum and from microchip M20W1 to M20E2 (correspondingly the effective size of the cavities should be modified).

Table of characteristic values of the 3 resonators

resonator	designed frequency [GHz]	real frequency [GHz]	designed Q	real Q	real photon lifetime [ns]
res1	7.5	7.65	4000	5047	660
res2	9.5	9.61	4000	11095	1155
res3	8.5	8.65	4000	6537	756

As can be seen from the table above, the experimental resonance frequencies of the resonators 1, 2 and 3 are a little bit higher than the designed values Q = 4000, especially the Q of res2. Consequently, the lifetime of photon in res2 is in the order of micron second which is worse for the fast measurements.

4.4 Characterization of the microchip M20E2 with 14 ports connected at 4.2 K

Since currently only two amplifiers are mounted inside of the cryostat, the characterization of all the three resonators and eight gate lines at 20 mK is time-consuming (the cooling-down, warm-up and rearrangement of cables take several days for each characterization). However with the 16-port dipstick (for detail see the section 3.4) dipping inside of the liquid helium, fast measurements can be easily achieved. Arbitrary combinations of connection of the four channels on the Network Analyzer with the 14 ports on the microchip M20E2 can be quickly switched. The unconnected 12 ports on the dip stick are terminated with 50 Ω terminations (see Fig 3.19) to suppress reflection signals.
However since the two parts of the resonators res1 and res3 in the two sides of the res2 are connected by Al (T_c=1.2 K) airbridges (see Fig 3.14) which are not superconducting at 4.2 K, the quality factors of res1 and res3 are expected to be lower than the case when they were cooled down to 20 mK in previous section.
As can be seen from Fig 4.21, the spectra S13, S27 and S86 show the resonance

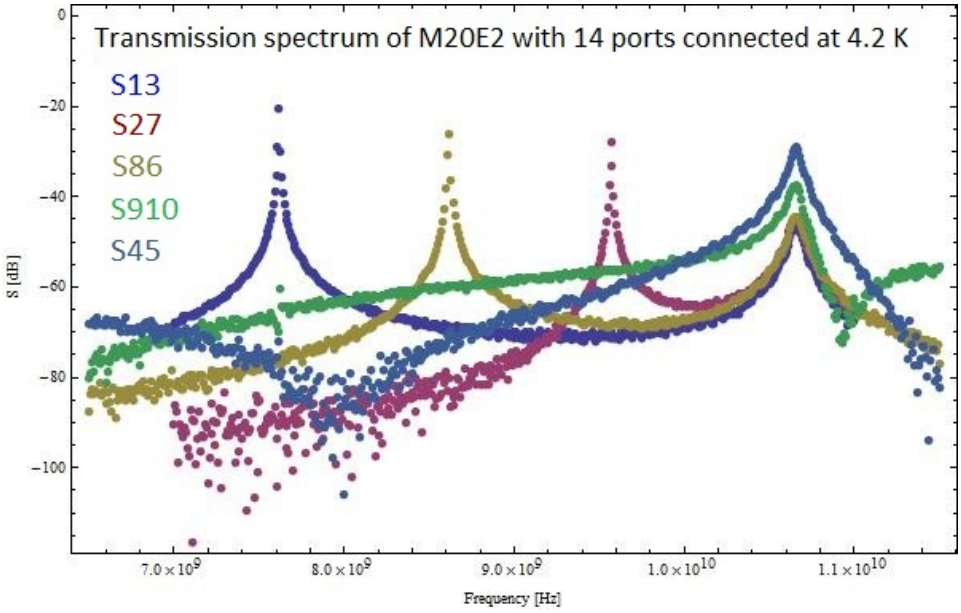

Figure 4.21: The transmission spectra of the microchip M20E2 with 14 ports connected to the dip stick and dipped inside of the liquid helium.

peaks of resonator res1 (7.62 GHz, Q=1287), res3 (9.77 GHz, Q=1663) and res2 (8.62 GHz, Q=1695) respectively. The resonance frequencies of res1, res2 and res3 are shifted a little bit compared the ones in previous section due to the change of dielectric environment from vacuum to liquid helium. However, the quality factor of res2 changed from 11095 in previous section to current 1695. This because the quality factor is temperature dependent. The quality factors of res1 and res3 are reduced as expected.
The spectra S13, S27, S86, S910 and S45 all show the resonance at 10.6 GHz with quality factor around 140.
When the dip stick is taken out of the liquid helium, the temperature on the sample increases and the resonances due to the Nb resonators are suppressed while the cavity modes still survive. The Fig 4.22 shows the transmission spectra S13 S14 and S15 when the dip stick is taken out of the helium dewar. It is confirmed that the unwanted resonance at 10.66 GHz is a cavity mode.

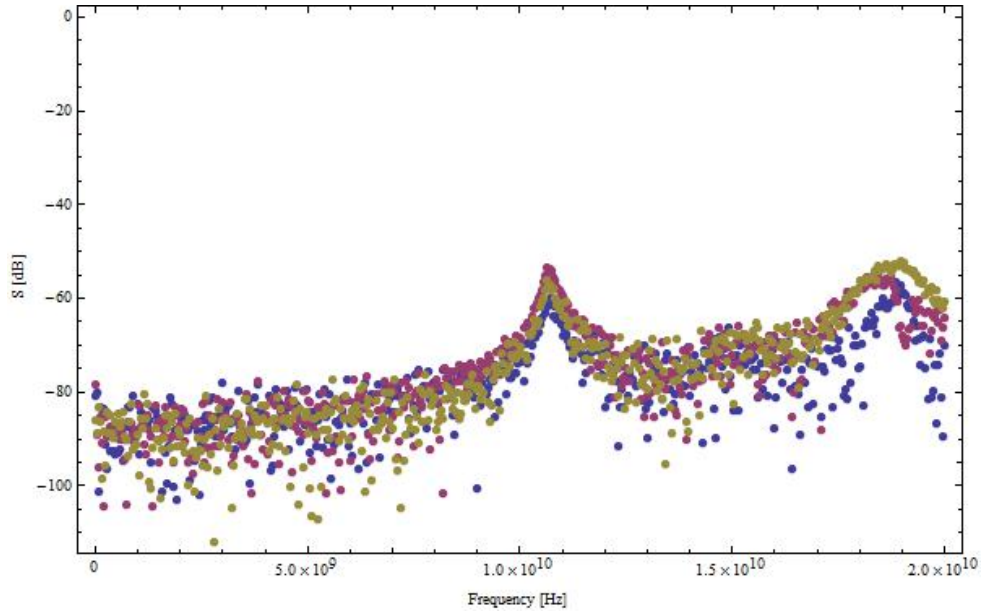

Figure 4.22: The transmission spectra S13 (blue), S14 (red) and S15 (yellow) when the sample temperature is over 9.2 K (the critical temperature of niobium). Only the cavity modes survive.

Chapter 5

Measurement

The characterizations of the PCB cover and the microchip M20E2 confirm that with PCB cover the cavity modes due to the cylindrical cavity are eliminated. However, the rectangular cavity modes especially the one at 10.6 GHz still survive. In the consecutive measurements, special attention should be paid at frequency around 10.6 GHz.
The type of microchip we used in our first measurements in this chapter is M20K2 (see Fig 3.11) with big transmons (see Fig 3.13-3.17). The measurements of the sample can be categorized into several steps:

1. Measurement of the resonance frequencies of the resonators res1 res2 and res 3;
2. Spectroscopic measurements:
   - the dependence of the qubit transition frequency on the magnetic flux (i.e. the biasing voltage of the coils),
   - determination of the charging energy E_{Ci} and Josephson energy E_{Ji}^{max} of each qubit qbi (i=1,2,3,4),
   - the coupling strength g_i of each qubit to the resonators;
3. Time-resolved single qubit operation:
   - Rabi oscillations to determine the relaxation time T_1,
   - Ramsey experiments to determine the dephasing time T_2;
4. Spin echo experiments to enhance the dephasing time T_2 by canceling the low frequency noise components;
5. AC-Stark effect to determine the photon number inside the cavity;
6. Two-photon induced sideband transitions which are for the conversion of qubit states into photon states and for the coupling of several qubits;
7. Quantum state tomography;
8. Quantum teleportation etc...

Due to the time restriction, in this thesis only the first 3 types of experiments are conducted and will be briefly shown in this chapter.
Basically there are two kinds of measurement techniques: the (weak) continuous measurement and the (strong) pulsed measurement (the measurement is weak or strong depends on the photon number inside of the cavity).
In the (weak) continuous measurement, the measurement signal is applied before, during and after the qubit state operation. Therefore the in-situ observation of the state evolution before, during and after the qubit state operation is achieved. However the measurement photons induce the ac-Stark shift of the transmon frequency $\hbar\chi a^\dagger a\sigma_z$. As the photon number fluctuates the shift varies which causes the measurement-induced dephasing. Thus low measurement power (small photon number) is required. However low measurement power results in low SNR. Therefore large number of measurement is necessary.
In the (strong) pulsed measurement, the measurement signal is applied only after the qubit state operation. It's beneficial because the qubit resonance frequency shift due to the ac-Stark effect can be eliminated and thus the measurement-induced dephasing can be avoided.

5.1 Resonance frequencies of the resonators

The resonance frequencies of the resonators are obtained by performing a frequency swept RF signal with constant power -25 dBm from the RF generator to the resonators on the microchip. The resonance frequency of the resonator is dispersively shifted by a term g^2/Δ due to the presence of the qubit. And the sign of this dispersive shift depends on the state of the qubit (ground or excited state). Considering this effect, the qubit transition frequency is maximally detuned using voltage bias to minimize the influence of the qubit on the resonance frequency of the resonator. The amplitude $\sqrt{I^2+Q^2}$ and the phase arctan(Q/I) are obtained from the quadratures. The transmission amplitude shows a Lorentzian line shape

$$P(\nu) = P_0 \frac{\delta\nu^2}{(\nu-\nu_0)^2+\delta\nu^2}, \tag{5.1}$$

where P_0 is the maximal transmission power, ν_0 is its peak and $\delta\nu$ is the half width at half maximum (HWHM) of the Lorentzian shape function.
The phase shift of the transmission signal is given by

$$\delta(\nu) = \arctan[\frac{\nu-\nu_0}{\delta\nu}]. \tag{5.2}$$

By fitting the Lorentzian line of Eq. (5.1), the resonance frequency ν_0 and the HWHM $\delta\nu$ are obtained. The quality factor Q is obtained by

$$Q = \frac{\nu_0}{2\delta\nu} \tag{5.3}$$

The photon decay rate is obtained by

$$\frac{\kappa}{2\pi} = 2\delta\nu \tag{5.4}$$

The life time of the photon inside the cavity is given by $T_\kappa = 2\pi/\kappa$.

The resonance frequencies of the resonator res1 res2 and res3 are 7.59 GHz,

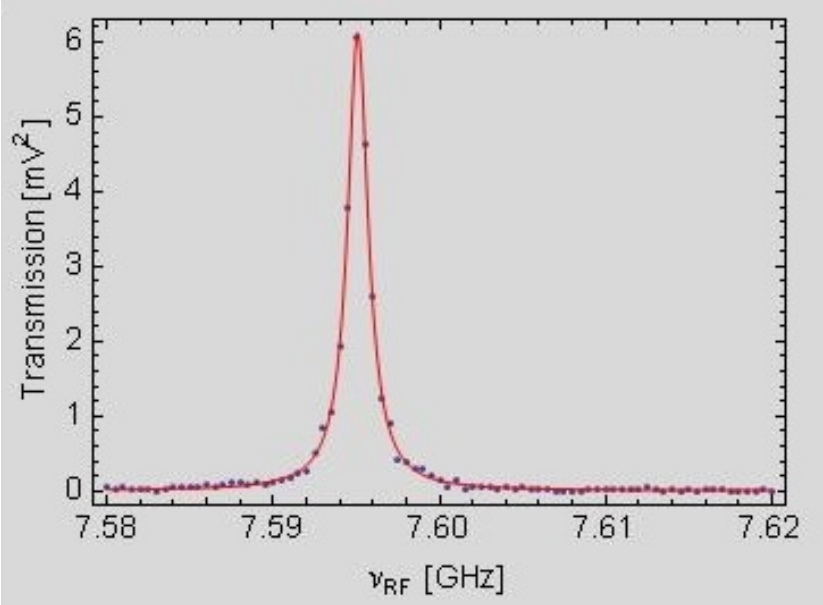

Figure 5.1: The transmission spectrum of the resonator res1 on the microchip M20K2 when the qubits are far detuned from the resonator. The blue dots are fitted by the red Lorentzian line shape (see Eq. (5.1)).

10.07 GHz and 8.55 GHz, respectively. The quality factors of the res1 and res3 are 5070 ($\kappa = 1.5$ MHz) and 202 ($\kappa = 42.4$ MHz), respectively. The low quality factor of resonator res3 is due to some particles on it which are removed after our first experiments (consequently, the measurement results concerning the resonator res3 are only partially conducted due to its poor quality).

5.2 Spectroscopic measurements

The transition frequency of the transmon is measured by the spectroscopic measurements. The resonance frequency of the resonator with the presence of the transmon is first probed. Then an RF signal is tuned to match the resonator frequency and is sent through the resonator continuously. In addition, a frequency swept spectroscopy signal is sent to the qubit either via the charge line or through the resonator. When the spectroscopy signal is on resonance with the transmon transition frequency (the transmon is continuously drived and finally equilibrates at the superposition of the ground and excited states), the transmitted RF signal drops due to the shift of the resonator frequency. This drop fits a Lorentzian line shape and its width inversely scales with the

spectroscopy power and the lifetime of the transmon.

As can be seen from the Eq. (2.9), the qubit transition frequency depends on

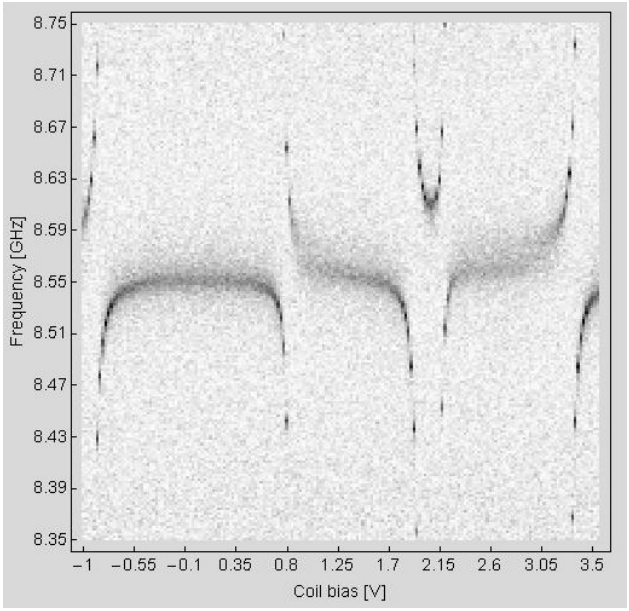

Figure 5.2: The resonance frequency of the resonator res3 depends on the states and the detunings of the qubits qb3 and qb4. Anticrossings occur when the qubits are on resonance with the resonator.

the magnetic flux through its SQUID loop. The magnetic field is created by sending dc currents through the coils attached on the back side of the mount (for detail see the chapter 3). Thus, the qubit transition frequency is tunable by controlling the voltage source of the coils. Since the transition frequency of the transmon is magnetic field dependent, the spectroscopic experiment can be repeated with different magnetic fields. By increasing the voltage on the coil, the magnetic field dependent qubit transition frequency is obtained and the maximum transition frequency of the qubit is achieved.

The maximum transition frequencies of the qb1 and qb 2 are $f_{qb1}^{max} = 12.092$ GHz and $f_{qb2}^{max} = 11.432$ GHz, respectively.

By increasing the input RF power, the ground state to the second excited state transition appear. The charging energy can be deduced from the Eq. (2.10). The charging energies of qubits qb1 and qb2 are 282 MHz and 251 MHz respectively. With the maximum transition frequencies and the charging energies, the Josephson energies are deduced from Eq. (2.9). We get $E_{J,max}^{qb1} = 67.6$ GHz and $E_{J,max}^{qb2} = 68.1$ GHz, respectively.

When the qubit transition frequency is tuned closer and closer to the resonance frequency of the resonator ($\Delta \to 0$), the dipersive shift of term g^2/Δ gets larger and larger and changes sign when they cross each other. The phase shift also changes sign at this point (see Fig 2.7 and 2.8). At the anticrossing, the coupling strength between the qubit and the resonator is obtained by measuring the minimum spacing between the anticrossing lines (see Fig 5.3). The

coupling strength between resonator res1 and qubits qb1, qb2 are 147 MHz and 60 MHz, respectively. The coupling strength between resonator res3 and qubits qb3, qb4 are 105 MHz and 145 MHz, respectively.

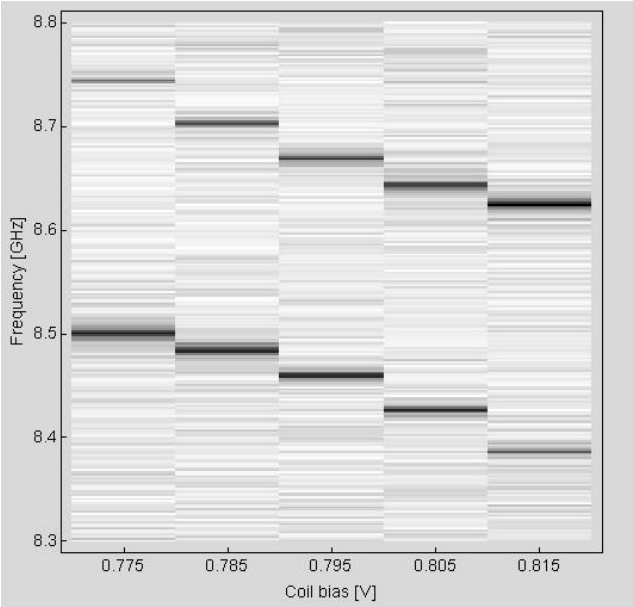

Figure 5.3: The coupling strength of the qubit qb3 can be inferred from the smallest spacing between the anticrossings.

5.3 Decoherence

Since the macroscopic transmon qubit is easily coupled to its environment, the relaxation and dephasing of its state are therefore induced.
In the following sections, the time resolved measurements of the qubit state in the dispersive limit are conducted to determine the relaxation time T_1 and the dephasing time T_2.
In order to be insensitive to the magnetic field variations, the magnetic flux through the SQUID loop is tuned to an integer number of the quantum flux Φ_0. The experiments that are not conducted on these "sweet" spots are also shown.

5.3.1 Rabi oscillations and relaxation time T_1

Since the ratio E_J^{max}/E_C in our experiment is large (around 500), the charge dispersion is flat but the anharmonicity is small. To suppress the two-photon $|g\rangle \rightarrow |f\rangle$ transition, the pulses with Gaussian or tangential DRAG (derivative remove by adiabatic gate) envelope is used instead of the rectangular shape pulses.

The qubit is initially prepared in its ground state by relaxation. A length-fixed single pulse with amplitude varying from low to high on resonance with the qubit frequency is sent to the qubit through the charge line. The qubit is then rotated on the Bloch sphere about an axis which is defined as x-axis. The periodic transitions between ground state and excited state of the qubit states are called Rabi oscillations. The weak continuous measurement pulse on resonance with the resonator frequency is applied before, during and after the driving pulses (However we used strong pulsed measurement technique in our first several experiments). The excited-state population of the qubit is measured.
The above procedure is repeated every 110 μs to ensure the qubit is relaxed to its ground state. The pulse sequence is sent 10^4 times to average out the fluctuations.
The amplitudes of a length-fixed π pulse and $\pi/2$ pulse can thus be obtained.

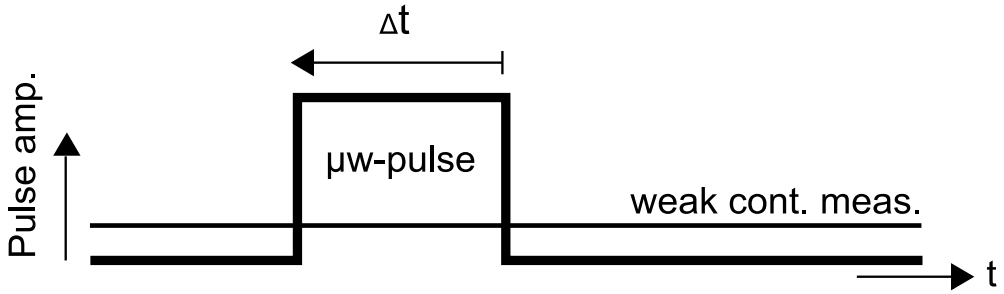

Figure 5.4: The pulse sequence of the Rabi oscillations is applied to the qubit through charge line while a weak continuous measurement signal on resonance with the resonator is sent through the resonator.

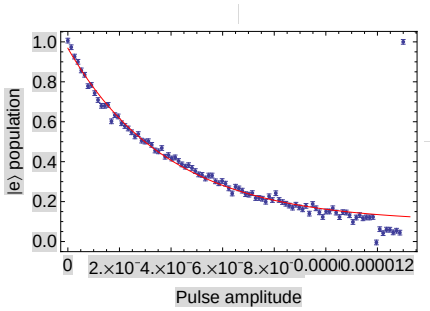

Figure 5.5: The fully populated qubit state decays from excited state to ground state. The blue dots are fitted by the red line and the relaxation time is obtained.

For a qubit in its ground state, a π pulse can drive it to its excited state. The population of the excited state decays exponentially to zero. A weak measurements signal can continuously monitor this decay. By fitting this population decay exponentially, the relaxation time is obtained (with strong pulsed measurement technique).

At 12.092 GHz, the relaxation time of qubit qb1 is 660 ns; at 4.913 GHz, the relaxation time is 4.15 μs.
At 11.422 GHz, the relaxation time of qubit qb2 is 550 ns; at 4.816 GHz, the relaxation time is 4 μs.

5.3.2 Ramsey experiments and dephasing time T_2

With known $\pi/2$ pulse amplitude and length from the Rabi experiments, the Ramsey fringe experiments now can be conducted.
With a qubit in its ground state, a $\pi/2$ pulse about the x-axis is applied to the

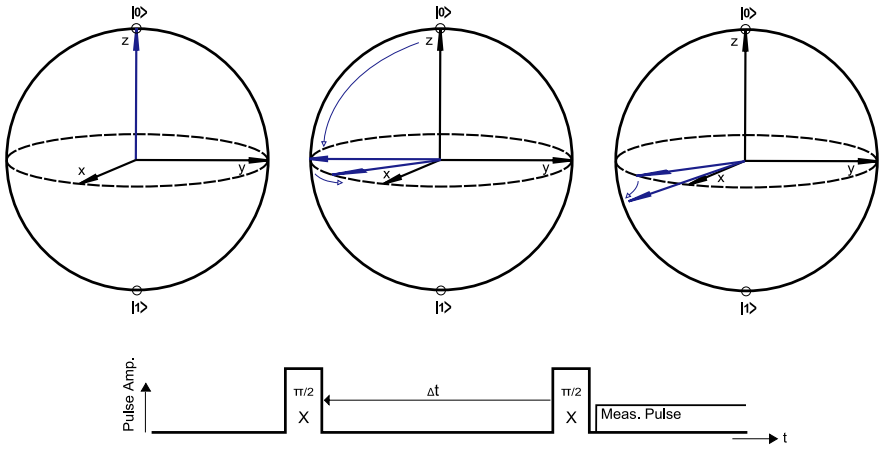

Figure 5.6: The qubit in its ground state is first drived by a $\pi/2$ pulse Δ detuned from the qubit about the x-axis. During Δt the state evolves on the equator and a phase of $\Delta\Delta t$ is accumulated. A same $\pi/2$ pulse is applied followed by a pulsed measurement.

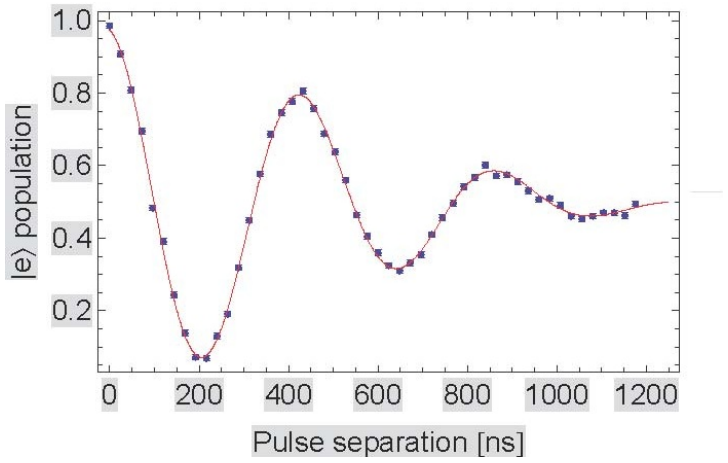

Figure 5.7: In the Ramsey fringe experiments, the blue dots are fitted by the red line and the dephasing time is obtained.

qubit. The qubit is thus brought to the equator (from $|0\rangle$ to $(|0\rangle + i|1\rangle)/\sqrt{2}$).

During the time interval Δt, the qubit is exposed to a phase shifting term and evolves about the z-axis. Then another $\pi/2$ pulse about the x-axis is applied to the qubit again. A measurement pulse is applied shortly after. The excited state population depending on the accumulated phase during Δt is obtained. Here the weak continuous measurement technique is not used because the measurement photons inside of the cavity will induce dephasing.
Both $\pi/2$ pulses are $\Delta = 4$ MHz detuned from the resonance frequency of the qubit. If the pulses are on resonance with the resonance frequency of the qubit, the qubit will not accumulate any phase during time Δt. And the two $\pi/2$ pulses can be linearly added to a π pulse which corresponds to a $|0\rangle \rightarrow |1\rangle$ transition. If the pulses are Δ detuned from the resonance frequency of the qubit, the qubit will accumulate a phase of $\Delta\Delta t$ during Δt. And the two $\pi/2$ pulses do not necessarily bring the qubit to the excited state as the previous case.
The above procedure is repeated and averaged for different interval time Δt. The dephasing time can be obtained by exponentially fitting the Ramsey fringe curve (see Fig 5.7).
At 12.092 GHz, the dephasing time of qubit qb1 is 1.1 μs; at 4.913 GHz, the dephasing time is 430 ns.
At 11.422 GHz, the dephasing time of qubit qb2 is 900 ns; at 4.816 GHz, the dephasing time is 500 ns.

Chapter 6

Conclusion

This master thesis is aimed at the implementation and characterization of 16-port devices in Circuit QED. We have first designed in Mathematica 8 and fabricated different versions of microchips (7 mm x 6.6 mm) with normal size transmons (200 μm x 30 μm) and with big size transmons (200 μm x 60 μm). As many as 3 crossed niobium resonators and four superconducting transmons can be arranged on the sapphire substrate. Each resonator can be capacitively coupled to its input and output ports by either finger capacitors or gap capacitors. Each transmon is controlled by a flux line and a charge line. The microchip is glued on a PCB interface and bonded to the ground planes and CPW of the PCB. The PCB is fixed on the mount on which three coils are fixed. The PCB is covered by a PCB cover and lid. The cables, PCBs, PCB covers, mounts, lids and 16-port dip stick are designed using CAD and manufactured. These 16-port devices are then assembled for characterizations at different temperatures.

The characterization of the PCB cover shows that the cylindrical cavity modes are eliminated due to the presence of the PCB cover. However the PCB cover brings the rectangular cavity modes. The characterization of the microchip M20E2 shows one cavity mode at 10.6 GHz which deserves much attention in our successive measurements.

In the following measurements, the resonance frequencies and quality factors of the resonators res1 and res3 on the microchip M20K2 are obtained. Longer relaxation times and dephasing times of the big transmons qb1 and qb2 are expected and achieved. Due to the particles on the resonator res3, the coherence times of transmons qb3 and qb4 are unable to be measured. However the coupling strengths of all the four transmons to the corresponding resonators are measured. The experiments show that the spectrum is clean and the coherence times are not influenced by the enlarged size of the microchip. No spurious modes are shown which indicates the success of our first step towards the future quantum teleportation on these microchips.

Remerciements

J'ai eu l'opportunité de pouvoir travailler pendant presque six mois entiers en tant que l'étudiant en master au sein du laboratoire de dispositifs quantiques. Chaque fois encadré par des gens différents qui m'ont tous appris énormément, je tiens à remercier vivement tout ces membres pour la convivialité et la sympathie que chacun d'entre eux m'a témoingné.
Ma gratitude va particulièrement à M. Andreas Wallraff qui m'a permis de faire ce travail de thèse au sein de cette équipe et qui m'a conseillé de faire ce stage avec M. Lars Steffen.
Je tiens tout d'abord à exprimer toute ma reconnaissance à Monsieur Lars Steffen, mon directeur de thèse qui m'a accueilli et qui a accepté de diriger ce travail de recherche, de m'avoir permis de faire un tout petit pas dans le monde de l'ordinateur quantique et de m'avoir fait confiance pour la démarche scientifique utilisée lors de mes manips et de mettre sa confiance en mes compétences. Merci de m'avoir appris les logiciels très utile Mathématica 8 et CAD. Merci d'avoir fabriqué les masques de micropuces.
Je suis très reconnaissant à M. Arkady Fedorov. Merci Arkady pour ton aide durant toutes les semaines de mon stage. Tu as su répondre à mes questions avec patience et pédagogie. Et je te remercie de fabriquer les transmons sur le micropuce.
Je vous remercie également pour la correction de manuscrit. Vos grandes compétences en physique m'ont beaucoup aidé à résoudre mes questions.
Mes remerciements s'adressent également à M. Matthias Baur pour sa gentillesse et son aide pendant la semaine où tout le monde était aux Etats-Unis. Tu m'a donné beaucoup de suggestions. Merci pour ton soutien et ta disponibilité.
Aussi je suis tellement reconnaissant du temps avec vous les gars Arjan van Loo, Simon Berger, Marek Pechal, Michael Peterer, Anna Stockklauser et Yves Salathé et je bénis aussi des supports de Markus Oppliger à la fin de ma thèse. Je remercie aussi les autres membres de l'équipe. Merci pour les moments agréables que nous avons passés ensemble.

Bibliography

[1] Isaac L. Chuang Michael A. Nielsen. *Quantum Computation and Quantum Information*. Cambridge University Press, 2010.

[2] G.E. Moore. Progress in digital integrated electronics. In *Electron Devices Meeting, 1975 International*, volume 21, pages 11 – 13, 1975.

[3] R. P. Feynman. Simulating physics with computers. *International Journal Of Theoretical Physics*, 10:467–488, 1982.

[4] D. Deutsch. Quantum theory, the church-turing principle and the universal quantum computer. *Proceedings of the Royal Society of London. Series A, Mathematical and Physical Sciences*, 400(1818):pp. 97–117, 1985.

[5] Peter W.Shor. Polynomial-time algorithms for prime factorization and discrete logarithms on a quantum computer. *SIAM J.SCI.STATIST.COMPUT.*, 26:1484, 1997.

[6] Lov K. Grover. Quantum mechanics helps in searching for a needle in a haystack. *Phys. Rev. Lett.*, 79:325–328, Jul 1997.

[7] M. Baur M. P. da Silva A. Fedorov, L. Steffen and A. Wallraff. Implementation of a toffoli gate with superconducting circuits. *nature*, 481:pp. 170–172, 2012.

[8] L. Steffen S. Filipp M. P. da Silva M. Baur, A. Fedorov and A. Wallraff. Benchmarking a quantum teleportation protocol in superconducting circuits using tomography and an entanglement witness. *Phys. Rev. Lett.*, 108:040502, 2012.

[9] M. Brune J. M. Raimond and S. Haroche. Manipulating quantum entanglement with atoms and photons in a cavity. *Rev. Mod. Phys.*, 73:565–582, 2001.

[10] B.D. Josephson. Possible new effects in superconductive tunnelling. *Physics Letters*, 1(7):251 – 253, 1962.

[11] R. J. Schoelkopf and S. M. Girvin. Wiring up quantum systems. *nature*, 451:664, 2008.

[12] P. Joyez D. Esteve V. Bouchiat, D. Vion and M. H. Devoret. Quantum coherence with a single cooper pair. *Phys. Scr.*, T76:165–170, 1988.

[13] Richard Phillips Feynman. *Feyman Lectures on physics Volume 3*. Addison-Wesley Pub. Co., 1963.

[14] Vinay Ambegaokar and Alexis Baratoff. Tunneling between superconductors. *Phys. Rev. Lett.*, 10:486–489, Jun 1963.

[15] Vinay Ambegaokar and Alexis Baratoff. Tunneling between superconductors. *Phys. Rev. Lett.*, 11:104–104, Jul 1963.

[16] V. Ambegaokar and A. Baratoff. Tunneling between superconductors. *Phys. Rev. Lett.*, 10:486, 1963.

[17] Andreas Wallraff. *Fluxon Dynamics in Annular Josephson Junctions: From Relativistic Strings to Quantum Particles*. PhD thesis, Friedrich-Alexander-Universitat Erlangen-Nurnberg, (2000).

[18] Y. A. Pashkin Y. Nakamura and J. S. Tsai. Coherent control of macroscopic quantum states in a single-cooper-pair box. *nature*, 398:pp.786–788, 1999.

[19] P. Joyez P. J. Meeson D. Vion D. Esteve F. Chiarello A. Shnirman Y. Makhlin J. Schriefl G. Ithier, E. Collin and G. Schn. Decoherence in a superconducting quantum bit circuit. *Phys. Rev. B.*, 72:134519, 2005.

[20] Jens Koch, Terri M. Yu, Jay Gambetta, A. A. Houck, D. I. Schuster, J. Majer, Alexandre Blais, M. H. Devoret, S. M. Girvin, and R. J. Schoelkopf. Charge-insensitive qubit design derived from the cooper pair box. *Phys. Rev. A*, 76:042319, Oct 2007.

[21] M. Baur R. Bianchetti P. J. Leek A. Blais J. M. Fink, M. Gppl and A. Wallraff. Climbing the jaynescummings ladder and observing its sqrtn nonlinearity in a cavity qed system. *nature*, 454:315–318, 2008.

[22] R. J. Thompson, G. Rempe, and H. J. Kimble. Observation of normal-mode splitting for an atom in an optical cavity. *Phys. Rev. Lett.*, 68:1132–1135, Feb 1992.

[23] J. M. Fink M. Baur R. Bianchetti P. J. Leek A. Blais A. Fragner, M. Gppl and A. Wallraff. Resolving vacuum fluctuations in an electrical circuit by measuring the lamb shift. *Science*, 322:1357–1360, 2008.

[24] Proceedings of the american physical society. *Phys. Rev.*, 69:674–674, Jun 1946.

[25] Alexandre Blais, Ren-Shou Huang, Andreas Wallraff, S. M. Girvin, and R. J. Schoelkopf. Cavity quantum electrodynamics for superconducting electrical circuits: An architecture for quantum computation. *Phys. Rev. A*, 69:062320, Jun 2004.

[26] E. Jaynes and F. Cummings. Comparison of quantum and semiclassical radiation theories with application to the beam maser. *Proceedings of the IEEE*, 51:89–109, 1963.

[27] A. Blais L. Frunzio R.-S. Huang J. Majer S. M. Girvin D. I. Schuster, A. Wallraff and R. J. Schoelkopf. Ac stark shift and dephasing of a superconducting qubit strongly coupled to a cavity field. *Phys. Rev. Lett.*, 94:123602, 2005.

[28] Matthias Baur. *realizing quantum gates and algorithms with three superconducting qubits*. PhD thesis, ETH Zurich, (2012).

[29] Lara Risegari Guglielmo Ventura. *The art of cryogenics: low-temperature experimental techniques*. Elsevier Ltd., 2008.

[30] L. Frunzio, A. Wallraff, D. Schuster, J. Majer, and R. Schoelkopf. Fabrication and characterization of superconducting circuit qed devices for quantum computation. *Applied Superconductivity, IEEE Transactions on*, 15(2):860 – 863, june 2005.

[31] M. Goppl, A. Fragner, M. Baur, R. Bianchetti, S. Filipp, J. M. Fink, P. J. Leek, G. Puebla, L. Steffen, and A. Wallraff. Coplanar waveguide resonators for circuit quantum electrodynamics. *Journal of Applied Physics*, 104(11):113904 –113904–8, dec 2008.

[32] HOU ZhaoWU. The magnetic field at the spot of galvanized solenoid. *Journal of guangxi university for nationalities*, 11(1), feb. 2005.

[33] R. Bianchetti. *Control and readout of a superconducting artificial atom*. PhD thesis, ETH, (2010).

[34] David M. Pozar. *Microwave engineering*. John Wiley Sons. Inc, 2005.

[35] Measurement of the reflector antenna absorption at terahertz frequencies by the method of a balanced radiometer. *Technical Physics*, 56(11):1652, 2011.